Magnetic Properties of Nanoparticle Arrays

by

Bassel Alkadour

A Thesis submitted to the Faculty of Graduate Studies of
The University of Manitoba
in partial fulfillment of the requirements for the Degree of

Doctor of Philosophy

Department of Physics and Astronomy
University of Manitoba
Winnipeg

Table of Contents

List of Figures

List of Tables

List of Abbreviations

Abbreviation	**Full Form**
BCC	Body-Centered Cubic
FCC	Face-Centered Cubic
FMR	Ferromagnetic Resonance
LLG	Landau-Lifshitz-Gilbert
MC	Monte Carlo
MPI	Message Passing Interface
NP	Nanoparticle
sLLG	Stochastic Landau-Lifshitz-Gilbert

Acknowledgments

First, I owe a profound debt of gratitude to my supervisor, Prof. Byron Southern for his mentorship and unwavering support throughout my PhD journey. His expertise, advice, and insights have been invaluable. I am also deeply thankful to my Co-Advisor Prof. Gerald Gwinner for all the guidance and support. I am grateful to Prof. John P. Whitehead, who also collaborated on this work.

This research was supported by a grant from the Natural Sciences and Engineering Research Council of Canada, whose financial support made this project possible. I am grateful for the support and resources provided by the University of Manitoba, which were invaluable to my research. Special thanks to the Department of Physics and Astronomy for their assistance and the use of their facilities.

I want to honor the memory of my father, Ahmad Rafee Alkadour who sadly passed away during my PhD studies. His unparalleled care, generosity, and wisdom will always inspire and guide me. This thesis is dedicated to him.

I am deeply grateful to my mother, Faten, for her love, patience, and encouragement.

Finally, I would like to thank my siblings for their continuous encouragement.

Abstract

This thesis presents an investigation of the magnetic properties and dynamics of maghemite ($\gamma - Fe_2O_3$) nanoparticle assemblies using atomistic spin dynamics simulations. The study focuses on the complex interplay between intra-particle interactions, such as surface anisotropy and vacancies, and inter-particle dipolar interactions in determining the collective magnetic behavior.

Atomistic simulations of individual maghemite nanoparticles reveal a significant reduction in magnetization at low temperatures, attributed to the competing effects of surface anisotropy and exchange interactions. The presence of vacancies introduces an inhomogeneous effective anisotropy unique to each nanoparticle. In triangular arrays, the interplay between surface effective anisotropy and dipolar interactions leads to the formation of magnetic domains, with domain size decreasing as surface anisotropy increases.

To understand the nature of dipolar interactions in nanoparticle assemblies, the study first examines the magnetic ordering in triangular arrays of point dipoles. The simulations reveal ferromagnetic in-plane ordering with a six-fold anisotropy arising from the order-from-disorder effect, consistent with previous theoretical studies. The dipole interactions in the triangular array are then compared with those in maghemite nanoparticle arrays. While nanoparticle arrays with zero surface anisotropy exhibit similar behavior to point dipole arrays, the presence of surface anisotropy leads to

the formation of magnetic domains, with domain size decreasing as surface anisotropy increases.

The spin-wave spectra of point dipole arrays reveal weak longitudinal modes and more dominant transverse modes, with the dispersion relations agreeing well with theoretical calculations. Spin wave excitations in the nanoparticle arrays are explored using Fourier analysis. In addition to propagating spin waves, localized modes are observed, originating from the hopping of magnetization between energy minima at the individual nanoparticle level. The surface anisotropy introduces spectral gaps and increases spin wave frequencies of the transverse and the longitudinal modes, with the frequency at zero wave-vector following a quadratic dependence on surface anisotropy strength for the transverse spin waves and following a linear dependence on the surface anisotropy for the longitudinal spin waves (for small values of the surface anisotropy).

The multiscale hierarchical model developed in this work captures the intricate interplay between intra-particle and inter-particle interactions. The atomistic simulations provide insights into the role of surface effects and defects in determining the magnetic properties of nanoparticle assemblies, highlighting the necessity of considering atomic-scale structure in the design and optimization of magnetic nanomaterials.

Chapter 1

Introduction

1.1 Magnetic Nanoparticles: An Overview

Magnetic nanoparticles have gained significant attention in recent years due to their unique properties and potential applications in various fields, such as biomedicine, data storage, and environmental remediation [3, 4, 5]. These nanoparticles are typically defined as materials with sizes ranging from 1 to 100 nm, exhibiting magnetic behavior that differs from their bulk counterparts [6]. Among the most common types of magnetic nanoparticles are iron oxides (e.g., magnetite, maghemite), ferrites (e.g., cobalt ferrite, manganese ferrite), and metallic nanoparticles (e.g., iron, cobalt, nickel) [7]. Various synthesis methods have been developed to produce magnetic nanoparticles with controlled size, shape, and composition, such as co-precipitation, thermal decomposition, and hydrothermal synthesis [8, 4].

1.2 Maghemite Nanoparticles

Among the various types of magnetic nanoparticles, maghemite ($\gamma - Fe_2O_3$) nanoparticles have attracted particular interest due to their favorable properties, such as high

saturation magnetization, high Currie temperature, small damping factor, biocompatibility, and chemical stability [9]. Maghemite has an inverse spinel structure, where the Fe^{3+} ions are distributed between the octahedral and tetrahedral sites, with vacancies present in the octahedral sites to maintain charge neutrality [10, 11]. The presence of these vacancies and the reduced coordination of surface atoms lead to complex magnetic behavior in maghemite nanoparticles [12, 13]. Understanding the magnetic properties and dynamics of these nanoparticles is crucial for their successful application in various fields.

1.3 Magnetic Interactions in Nanoparticle Assemblies

The magnetic behavior of nanoparticle assemblies is governed by a complex interplay between intra-particle and inter-particle interactions. Intra-particle interactions include exchange interaction, magnetocrystalline anisotropy, and surface anisotropy [14]. The exchange interaction is a quantum mechanical effect that favors the parallel alignment of neighboring spins, while magnetocrystalline anisotropy arises from the crystal structure and leads to preferred magnetization directions [15]. Surface anisotropy, which becomes significant in nanoparticles due to their high surface-to-volume ratio, originates from the reduced coordination and broken symmetry of surface atoms [14, 16].

Inter-particle interactions, primarily dipolar interactions, play a crucial role in determining the collective magnetic behavior of nanoparticle assemblies [17]. Dipolar interactions are long-range and anisotropic, leading to the formation of various magnetic structures. The strength and nature of these interactions depend on the nanoparticle arrangement, with triangular lattices being of particular interest due to their potential for stabilizing novel magnetic states.

1.4 Spin Dynamics in Magnetic Nanoparticle Assemblies

Understanding the spin dynamics in magnetic nanoparticle assemblies is essential for their application in high-frequency devices and spintronic technologies [18]. Ferromagnetic resonance (FMR) and spin waves are two fundamental aspects of spin dynamics in these systems. FMR refers to the precession of the magnetization around an effective magnetic field, while spin waves are collective excitations of the magnetization that propagate through the material [19]. Experimental techniques, such as Brillouin light scattering and FMR spectroscopy, have been employed to study spin dynamics in nanoparticle assemblies [20, 21].

Theoretical models, such as the Landau-Lifshitz-Gilbert equation and the Heisenberg model, have been used to describe spin dynamics in nanoparticle assemblies [22]. However, these models often rely on simplifying assumptions and fail to capture the complex interplay between intra-particle and inter-particle interactions. Atomistic simulations, which take into account the detailed structure and interactions of individual nanoparticles, provide a more accurate description of spin dynamics in these systems.

1.5 Computational Methods for Studying Magnetic Nanoparticles

Computational methods have become increasingly important in the study of magnetic nanoparticles, as they provide insights into the underlying physical mechanisms that are difficult to access experimentally. Micromagnetic simulations, which treat the magnetization as a continuous vector field, have been widely used to study the magnetic properties and dynamics of nanoparticles. However, these simulations often neglect the atomic-scale structure and interactions, which can have a significant impact on the magnetic behavior of small nanoparticles.

Atomistic spin dynamics simulations, on the other hand, model the magnetic moments of individual atoms and their interactions explicitly. This approach allows for a more accurate description of surface effects, defects, and thermal fluctuations, which are crucial in understanding the magnetic properties and dynamics of nanoparticles. However, atomistic simulations are computationally demanding, requiring the use of efficient algorithms and high-performance computing resources.

1.6 Motivation and Objectives of the Thesis

The magnetic behavior of nanoparticle assemblies is governed by a complex interplay between intra-particle and inter-particle interactions. Inter-particle interactions depend heavily on the chemical structure of the material. The long-range dipolar interactions, characterized by their long-range and anisotropic nature, depend strongly on the spatial distribution of the nanoparticles. This dependence offers a rich playground for tailoring the collective magnetic behavior of nanoparticle assemblies. Leveraging this level of control allows for engineering novel materials with specific properties. This holds tremendous promise in the realm of potential applications of assemblies of magnetic nanoparticles

Despite the extensive research on magnetic nanoparticles, there are still significant knowledge gaps in understanding the magnetic properties and dynamics of maghemite nanoparticle assemblies. In particular, the effect of surface anisotropy and the presence of vacancies on the collective magnetic behavior of these systems remains poorly understood. Experimental studies have provided valuable insights, but they often lack the resolution and control necessary to elucidate the underlying physical mechanisms.

Atomistic simulations offer a powerful tool to bridge this gap, as they can capture the complex interplay between intra-particle and inter-particle interactions at the atomic scale. However, most previous studies have focused on individual nanoparticles or simplified models of nanoparticle assemblies, neglecting the role of surface

anisotropy and vacancies [23].

The main objectives of this thesis are: 1. To develop an atomistic spin dynamics model for maghemite nanoparticle assemblies that accurately captures the surface anisotropy and the presence of vacancies. 2. To investigate the effect of surface anisotropy and vacancies on the magnetic properties and spin dynamics of maghemite nanoparticle assemblies using the developed model. 3. To provide insights into the interplay between intra-particle and inter-particle interactions in these systems and their impact on the collective magnetic behavior.

The novelty of this work lies in the application of atomistic spin dynamics simulations to study the magnetic properties and dynamics of maghemite nanoparticle assemblies with a realistic representation of surface anisotropy and vacancies. The results of this thesis are expected to advance our fundamental understanding of these systems and guide the design of novel magnetic nanoparticle-based materials and devices.

1.7 Thesis Outline

The remainder of this thesis is organized as follows:

- Chapter 2 provides an overview of the theoretical background and computational methods used in this work, including the atomistic spin dynamics model, the treatment of surface anisotropy and vacancies, and the numerical techniques employed.

- Chapter 3 presents the results of atomistic simulations on the magnetic properties of individual maghemite nanoparticles, focusing on the effect of surface anisotropy and vacancies on the magnetization and anisotropy energy.

- Chapter 4 discusses the magnetic properties and spin dynamics of maghemite

nanoparticle assemblies, with an emphasis on the role of inter-particle dipolar interactions and the interplay with intra-particle interactions.

- Chapter 5 explores the spin wave dynamics in maghemite nanoparticle assemblies, including the calculation of spin wave spectra and dispersion relations, and the effect of surface anisotropy and vacancies on the spin wave properties.

- Chapter 6 summarizes the main findings of the thesis, highlights the significance and implications of the results, and provides an outlook for future research directions.

By presenting a comprehensive study of the magnetic properties and dynamics of maghemite nanoparticle assemblies using atomistic simulations, this thesis aims to contribute to the fundamental understanding of these systems and pave the way for their rational design and application in various fields.

Chapter 2

Basic Background

2.1 Magnetic Interactions

2.1.1 Exchange Interactions

The exchange interaction is a quantum effect guided by the overlapping of electron orbitals from different atoms and the Pauli principle. The simplest case of the exchange interaction can be illustrated by considering two atoms where the two electrons (one from each atom) occupy overlapping orbitals. The Hamiltonian of the exchange interaction due to two overlapping orbitals is given by $\mathcal{H} = -JS_1S_2$, where J is the exchange parameter, S_1 is the spin operator acting on the first spin and S_2 is the spin operator acting on the second spin. The values of the exchange parameter depends on the nature of the overlapping of the two orbitals. In the case of a lattice of atoms, the orbital overlapping is usually limited to the nearest neighbour atoms and the exchange energy is given by the Heisenberg model,

$$\mathcal{H} = -\frac{1}{2}\sum_{ij}(J_{ij}\hat{S}_i \cdot \hat{S}_j), \tag{2.1}$$

where J_{ij} is the exchange constant between the spin i and the spin j. Since the overlapping of the orbitals is usually limited to neighbouring atoms, J_{ij} is zero except when atom i and atom j are nearest neighbours of each other.

The exchange effect is the strongest and most influential interaction in determining the magnetic order of a material. In the case of non-interacting atoms ($J = 0$), the spins are randomly oriented in the absence of an external magnetic field. This group of materials is referred to as paramagnetic. Fig. 2.1(A) shows an illustration of a paramagnet.

If the exchange parameter is positive, the energy is minimized by aligning the spins parallel to each other (ferromagnetic order) as shown in Fig. 2.1(B). The net magnetization for the ground state reaches the saturation magnetization (the maximum possible magnetization). In this case, the saturation magnetization is $m_s = Ng_J\mu_B|S|$, where N is the number of atoms in the system, g_J is the Landé factor, and $\mu_B = 9.27 \times 10^{-24}\mathrm{JT}^{-1}$ is the Bohr magneton .

If the exchange constant is negative, the energy of each interaction bond is minimized by aligning each spin antiparallel to its nearest neighbours. For a lattice of identical atoms, the ground state can be illustrated by dividing the lattice into two sublattices where the spins on one sublattice are parallel to each other and antiparallel to the spins on the other sublattice. This is called an antiferromagnetic configuration and it is illustrated in Fig. 2.1(C). The net magnetization of the ground state in this case is $m = \frac{N}{2}g_J\mu_B|S| - \frac{N}{2}g_J\mu_B|S| = 0$.

If the exchange constant is negative, but the spins on one sublattice are larger than the spins on the other, the net magnetization can have a large magnetization that is comparable to ferromagnets while the spin alignment is similar to antiferromagnets as illustrated in Fig. 2.1(D). Such systems (ferrimagnets) along with the antiferromagnets were discussed by L. Neél in 1948 [24, 25].

In some materials such as ionic solids, the orbitals of the neighbouring magnetic ions do not overlap, and the exchange interaction is expected to be negligible, leading to a paramagnetic behaviour. For example, in transition metal oxides, the magnetic moment is mainly due to the orbitals $3d$, but the metal cations are separated by oxygen anions, and the $3d$ orbitals do not overlap. Nevertheless, some of these materials, such

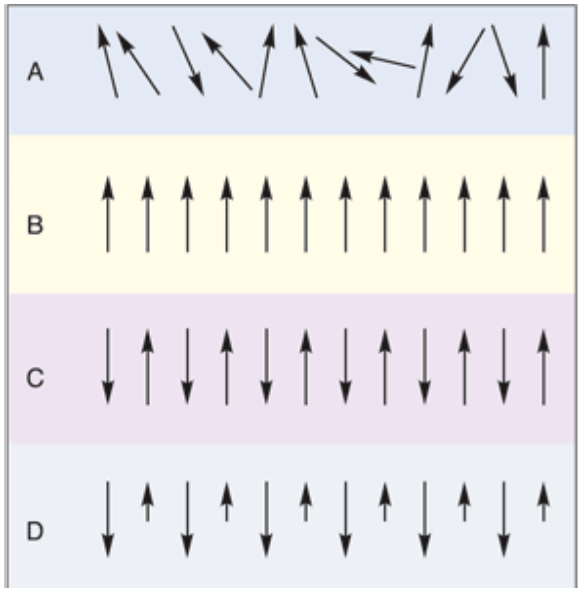

Figure 2.1: The magnetic configuration of a paramagnet (A), a ferromagnet (B), an antiferromagnet (C), and a ferrimagnet (D).

as $\gamma - Fe_2O_3$, show strong interactions. Thus, the interaction must be mediated by the non-magnetic atoms that are between the two magnetic ions. This mechanism of interaction is called superexchange, and it was proposed by Kramers in 1934 [26].

To illustrate this mechanism, Fig. 2.2 shows the orbital overlapping of collinearly arranged Mn-O-Mn and the associated possible magnetic configurations. There are five electrons occupying the $3d$ orbitals in Mn^{2+} with parallel spins (according to Hund's rule), whereas the $2p$ orbitals of the oxygen are fully occupied by electrons with antiparallel spins. Fig. 2.2(a) shows the ferromagnetic configuration whereas Fig. 2.2(b) shows the antiferromagnet configuration. In Fig. 2.2(b), electrons from the $2p$ orbitals of the oxygen can hop to both of the half-occupied $3d$ orbitals or even from one $3d$ orbital to the other without violating Pauli's principle. This freedom of motion (or delocalization of the involved electrons) reduces the restrictions on the electrons and hence lowers the energy. In Fig. 2.2(a), such motion is forbidden due to

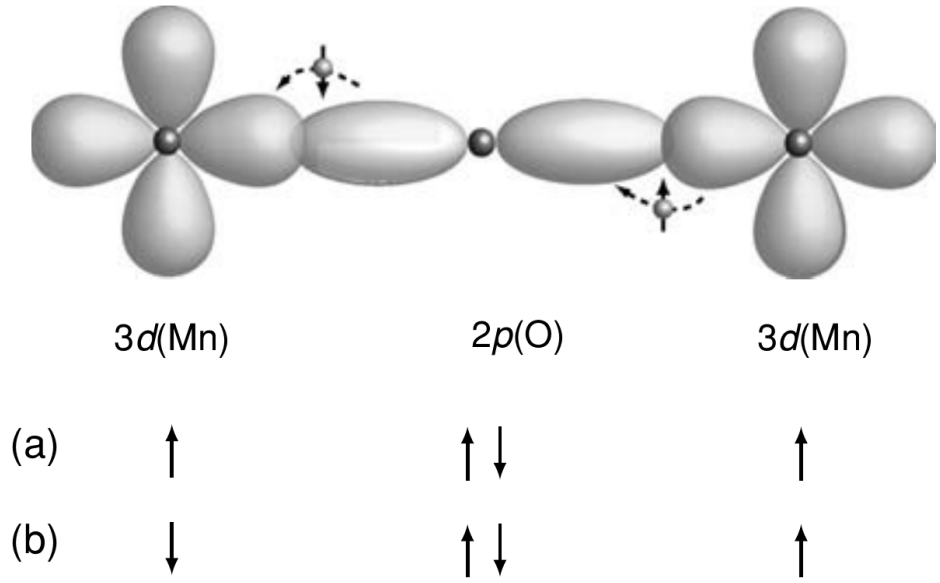

Figure 2.2: The orbital overlapping in a Mn-O-Mn bond with a (a) ferromagnetic configuration, and (b) antiferromagnet configuration.

Pauli's principle. Thus, the antiferromagnet configuration is energetically favourable.

The sign and strength of the superexchange depends on many factors such as the involved orbitals, the distance between the atoms, and the bond angle. The superexchange is complex due to involving multiple hybridized orbitals. Thus, semi-empirical rules have been developed by Anderson, Goodenough, and Kanamori, over the years in 1950s[27, 28, 29, 30]. According to these rules, when the bonding angle is 180°, such as the case above, the two magnetic atoms with partially filled $3d$ orbitals interact antiferromagnetically. On the other hand, they have weak ferromagnetic interaction when the angle is 90°.

2.1.2 Magnetic Anisotropy

The exchange interaction involves only spins and not spatial coordinates so that the spin space and coordinate space are decoupled and the energy is independent of the

magnetization direction. The majority of magnetic systems are anisotropic, where the energy depends on the direction of the magnetization. This dependence may be attributed to many effects such as the magneto-crystalline anisotropy, surface anisotropy, and shape anisotropy.

The magneto-crystalline anisotropy is due to the spin-orbit coupling. Since the orbitals are linked with the crystalline structure in solid materials, the magneto-crystalline anisotropy energy depends on the relative direction of the magnetization with respect to the crystalline axes.

The surface anisotropy is due to the broken symmetry at the surface of the material. The atoms at the surface have fewer neighbouring atoms than the interior atoms. Thus, the surface atoms have a lower number of exchange interactions. Also, the orbitals of the surface atoms are linked to fewer atoms than those of the interior atoms. This results in a significant change in the crystalline anisotropy at the surface due to the orbital distortion. In other words, the electrons of the surface atoms have a small probability of being out of the surface. The restriction of the motion of these electrons to be in the plane of the surface is associated with an angular momentum that is perpendicular to the surface.

The significance of the surface anisotropy can be illustrated by considering a thin film of Co with variable thickness. For the relatively thick film, the magnetization prefers to be in-plane. With decreasing the film thickness, the ratio of the number of the surface atoms to the number of the interior atoms increases. As a result, the effect of the surface anisotropy becomes significant in comparison with the volume anisotropy due to reducing the thickness. Below a critical thickness, the magnetization rotates to become perpendicular to the surface[31]. Since the surface-to-volume ratio increases with decreasing size, surface anisotropy plays a significant role in nano-sized magnetic particles. It is important to note that the factors contributing to surface anisotropy, such as broken symmetry, surface strain, and the orbital nature at the surface, can depend on the direction of crystalline growth and the composition of

the layers that share an interface with the film. Therefore, the crystalline growth relative to the surface and the coating material can significantly influence the nature and strength of surface anisotropy [32].

The exact dependence of the energy on the direction of magnetization can be complex. However, in many cases, the magnetization tends to align along a specific axis known as the easy axis. The simplest and most versatile model for describing anisotropy is the Stoner–Wohlfarth model, where the anisotropy is uniaxial and is given by $E = KV\sin^2(\theta)$, where K is the anisotropy constant, V is the volume of the material, and $\theta$is the angle between the magnetization and the easy axis. This model was first proposed by Stoner and Wohlfarth for nanoparticles with uniform magnetization [33]. The model is widely popular due to its simplicity and its success in describing many systems.

The shape anisotropy is a magnetostatic effect that depends on the geometric confinement of the magnetization to be inside the substance. To understand this anisotropy, let us assume a uniform magnetization inside a thin film as shown in Fig. 2.3. We can represent each dipole by two magnetic charges. The magnetic charges, an imaginary construct analogous to electric charges, are zero everywhere except at the surface area that is perpendicular to the magnetization. These charges generate a field in the opposite direction of the magnetization inside the film (the demagnetization field). When the magnetization is perpendicular to the plane of the film, the magnetic charges are large and separated by the small thickness of the film. Thus these charges generate a large demagnetization field as shown in Figs. 2.3A,B. When the magnetization is in the plane, the magnetic charges are small and far apart from each other, resulting in a small demagnetization field as shown in Figs. 2.3C,D. Since the demagnetization field opposes the direction of the magnetization, the larger the field, the larger the energy of the system. Hence, aligning the magnetization in the plane of the film is energetically favourable. Obviously, the shape anisotropy depends on the shape of the substance. In a sphere, the demagnetization field has the same

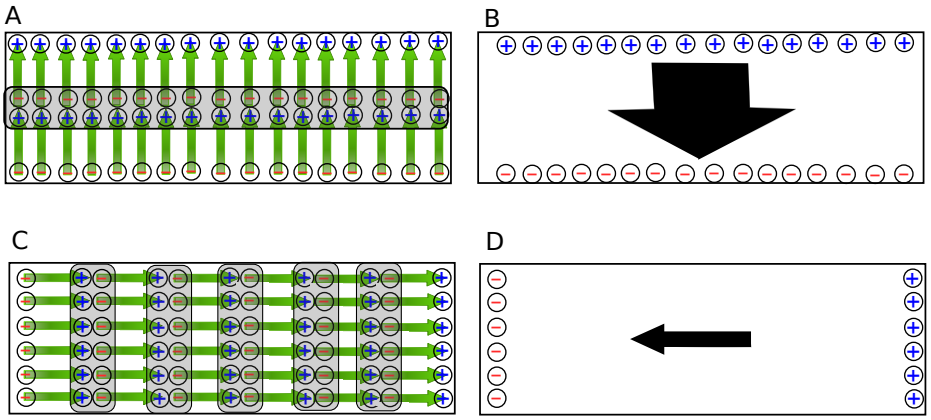

Figure 2.3: The distribution of the magnetic charges in a thin film with a uniform magnetization. An illustration of the magnetic charges for a uniform out-of-plane magnetization is shown in (A) and the generated demagnetization field (B). Similarly, the magnetic charges and the resulting demagnetization field for an in-plane magnetization is shown in (C) and (D), respectively.

magnitude regardless of the direction of the magnetization, and there is no preferred direction due to the shape of the particle.

The demagnetization field is merely the dipole field generated inside the particle. Two spatially separated magnetic particles can interact with each other by the dipole field generated outside each particle.

2.1.3 Dipole Interactions

The energy due to the dipole interactions between magnetic dipoles is given by

$$E_d = -\frac{\mu_0}{4\pi}\frac{\mu^2}{a^3}\sum_{i>j}\left[\frac{3(\hat{\sigma}_i\cdot\vec{r}_{ij}/a)(\hat{\sigma}_j\cdot\vec{r}_{ij}/a)}{(r_{ij}/a)^5} - \frac{\hat{\sigma}_i\cdot\hat{\sigma}_j}{(r_{ij}/a)^3}\right], \tag{2.2}$$

where μ_0 is the vacuum permeability, a is the distance unit, r_{ij} is the distance between the dipoles i and j, $\hat{\sigma}_i$ is a unit vector in the direction of the dipole i, and μ is the magnet moment of one spin (or particle). The dipole energy of two neighboring spins

of $1\mu_B$ and separated by 0.3 nm is of the order of $|E_{d0}|/k_B = 0.014\,\mathrm{K}$. This is five orders of magnitude smaller than the exchange energy, but the dipole interactions are long-ranged, and the dipole energy accumulates over a long distance to have significant influence.

Dipole interactions become important in the case of an assembly of magnetic nanoparticles with a uniform magnetization inside each nanoparticle. If the nanoparticles are separated from each other, the inter-particle interactions are purely due to the dipole interactions. Each nanoparticle can be approximated by a single magnetic dipole with a magnitude μ proportional to its size. Hence, the interparticle-interactions (dipole interactions) can be controlled by the size of the particle or the distance between the particles.

Furthermore, the nature of the inter-particle magnetic order, and hence the macroscopic magnetic order, can be controlled by the spatial distribution of the particles. For example, when the magnetic dipoles (the nanoparticles) are on an infinite FCC[34], BCC[35], or triangular[36, 37] superlattice, the magnetic dipoles order ferromagnetically. On the other hand, the magnetic order of a square array forms anti-parallel stripes[36, 38, 39]. The tunability of the dipole interactions by controlling the size, geometric arrangement and the inter-particle spacing provides an opportunity to synthesize structures with novel magnetic properties. The interplay between the intra-particle short-range interactions (exchange and anisotropy) and the long-range (dipole) interactions may result in more complex and novel properties. These novel properties provide the potential for new applications. To fully exploit this potential, it is essential to understand the interplay between the various interactions.

2.2 Magnetic Domains

So far, we have assumed a uniform or semi-uniform magnetization inside the particle. This is not necessarily the case. For example, two large pieces of iron do not at-

tract or repel each other unless they are magnetized. This attributes to the presence of multiple domains inside the piece of iron, resulting in negligible net magnetization. The presence of dipole interactions can drive domain formation. To understand the mechanism of this formation, we consider a finite-size material with dipole and ferromagnetic exchange interactions.

In the continuous magnetization approximation, where the magnetization is assumed to vary smoothly and continuously across the material rather than changing abruptly at the atomic scale, the exchange energy of a ferromagnet with a simple cubic structure can be expressed as

$$E_{ex} = \frac{A}{M_s^2} \int dV (\nabla \mathbf{M})^2 = A \int dV (\nabla \boldsymbol{\sigma})^2, \tag{2.3}$$

where $A = n_l JS^2/a$ is the exchange stiffness constant, n_l is the number of atoms per unit-cell and a is the unit-cell parameter, M_s is the spontaneous magnetization, σ is a unit vector in the direction of the local magnetization, V is the volume, and $\mathbf{M}$ is the local magnetization. Since the change in the energy is what we are interested in, the ground state energy is neglected in E_{ex}. From Eqn. [2.2], the dipole energy of a magnetically saturated ferromagnet (all dipoles are parallel) is of the order of $E_{ds} \sim \mu_0 \ (\mu^2/a^3)N$, where N is the number of the spins. Since $\mu/a^3 = M_s$ and $Na^3 = V$, it follows that the dipole energy of a saturated particle is of the order of $E_{ds} \sim \frac{1}{2}\mu_0 V M_s^2$.

The dipole energy can be reduced by forming multiple magnetic domains, as illustrated in Fig. 2.4(a). A magnetic domain is a region with a relatively uniform magnetization. The gradient in the magnetization between two magnetic domains can be in the form of a Bloch or Néel domain-wall as illustrated in Fig. 2.4(b). In a Bloch wall, the magnetization rotates parallel to the domain wall plane, while in a Néel wall, the magnetization rotates perpendicular to the domain wall plane. The formation of magnetic domains reduces the magnetic charges at the surface significantly. Hence, the dipole energy of the multi-domain arrangement is a small fraction

of the dipole energy of the single domain arrangement. This reduction in the dipole energy is associated with an increase in the exchange energy due to the gradient in magnetization by $E_{ex} = AV < (\nabla \boldsymbol{\sigma})^2 >$. By assuming that the change in magnetization direction occurs uniformly over a characteristic length scale δL, We estimate the increase in the exchange energy as $E_{ex} =\approx AV(\delta \boldsymbol{\sigma}/\delta L)^2$. We introduce a characteristic length, L_{ex}, of the order of the minimum distance at which the magnetization changes its direction by $|\delta \boldsymbol{\sigma}| = 1$ to reduce the dipole energy. This change in the direction of the magnetization increases the exchange energy by $E_{ex} \approx AV/L_{ex}^2$. By equating the increase in the exchange energy with the decrease of the dipole energy ($\sim E_{ds}$), we find the exchange-correlation length to be

$$L_{ex} = \sqrt{\frac{2A}{\mu_0 M_s^2}}. \tag{2.4}$$

The exchange-correlation length is an important parameter that relates to the size of the magnetic domains. The magnetic properties of a particle can fall in one of two very different regimes depending on the particle's size relative to the exchange correlation length. For ferromagnetic particles with dimensions smaller than L_{ex}, the magnetization remains mostly uniform. We refer to these particles as single-domain nanoparticles, and the dipole field outside each particle can be approximated by assuming that the nanoparticle is a single super-dipole. For particles with much larger dimensions than the exchange-correlation length, the magnetization inside the particle is divided into magnetic domains to minimize the dipole energy. Consequently, the net magnetization of these particles almost vanishes. Hence, the dipole field that is generated outside the particle is negligible, and the inter-particle interaction becomes small (such as the case of two macroscopic pieces of iron). Typically, the value of L_{ex} falls in the range from a few to tens of nanometers. It is important to note that our calculations of the exchange-correlation length account only for dipole interactions and ferromagnetic exchange interactions. The inclusion of other effects, such as anisotropy, could significantly influence the exchange-correlation length.

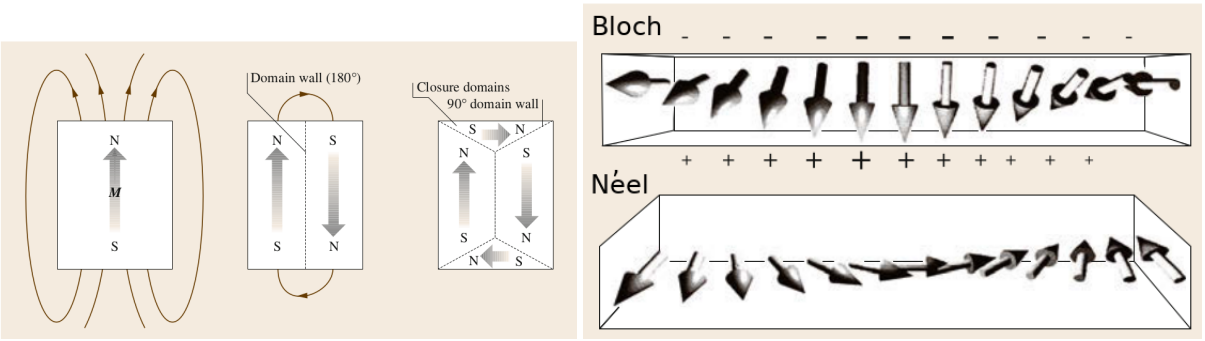

(a) (b)

Figure 2.4: (a) The magneto-static energy is minimized by forming multiple domains at the expense of the exchange energy. (b) Magnetic domains are separated by a Bloch or Néel wall.

2.3 Temperature effect

The temperature dependence of classical physical systems is governed by the statistics of the Boltzmann distribution. In the Boltzmann distribution, the probability of finding the system in a state (ν) is proportional to $\exp(-E_\nu/k_BT)$, where E_ν is the energy of the system when it is in the state ν, k_B is the Boltzmann constant, and T is the temperature. Thus, the ratio of the probability of finding the system in a state ν_1 to the probability of finding it in a state ν_2 is $P_1/P_2 = \exp\left(-(E_{\nu 1} - E_{\nu 2})/k_BT\right)$. Let us consider the case of a simple ferromagnet in the ground state where all the spins are parallel. By assigning the label ν_1 to this state and ν_2 to the state of one spin being flipped in the opposite direction, we find that the difference in the exchange energy difference between the two states is $E_{\nu 2} - E_{\nu 1} = zJ$, where z is the number of the nearest neighbours. The ratio of the probability of the system being in the ground state probability to the probability that the spin is flipped is $P_1/P_2 = exp\left(zJ/k_BT\right)$. Near $T = 0$K, this ratio is very large and the system prefers to be in the ground ferromagnetic state. At temperatures much higher than zJ/k_B, this ratio drops down

to less than e^1, and the system is disordered (Noting that there are many disordered states in comparison with the ground state). Noting that the latter case is equivalent to the case of $J = 0$, the ferromagnet behaves as a paramagnet at high temperatures.

The mean-field approximation can be utilized in determining the thermal dependence of the physical properties of a magnetic system or estimating the Curie temperature. The Curie temperature (T_c) is the critical temperature above which the magnetic order vanishes completely. The mean-field theory was initially established by P. Weiss and P. Curie to explain the thermal behaviour of ferromagnetic materials and their response to an external field [40]. Their work (in 1906) proceeds the development of the Heisenberg exchange model [41, 25] (in 1928), which was incorporated explicitly in their calculations later on. The theory assumes that there is an effective magnetic field due to the interaction between the atoms and that this field is the same for all the identical atoms.

Assuming that an atom i has a magnetic moment $\vec{\mu_i}$, the energy of that atom is given by $E = -\vec{\mu_i} \cdot \left(\mu_0 \vec{H}_0 + \vec{H}_{\text{eff}}\right)$, where $\vec{H}_{\text{eff}} = \lambda \vec{M}$ is the effective field on the atom i due to the interactions with the surrounding atoms, $\vec{M}$ is the net magnetization, $\vec{H}_0$ is the applied field , and λ is the molecular field coefficient, which quantifies the strength of the interaction between a given atom i and the surrounding atoms within the material. Using the Heisenberg model, the mean-field approximation predicts the critical temperature to be $T_c = \frac{2zJs(s+1)}{3k_B}$, where s is the spin per atom. The magnetization dependence on temperature according to this theory is given by $M = NgsB_s(y)$, where $y = \frac{gs\mu_B\mu_0 H}{k_B T}$, N is the number of magnetic atoms per unit volume, g is the tha Landé factor, and $B_s(y)$ the Brillouin function of y. Figure 2.5 shows the temperature dependence of the magnetization for various values of s. For large values of s, the number of the eigenvalues $(2s + 1)$ increases. Hence, the quantum discretization becomes less important and the magnetic moment can be approximated as a classical magnetic dipole.

The mean-field theory is an elegant tool to investigate the thermal properties of

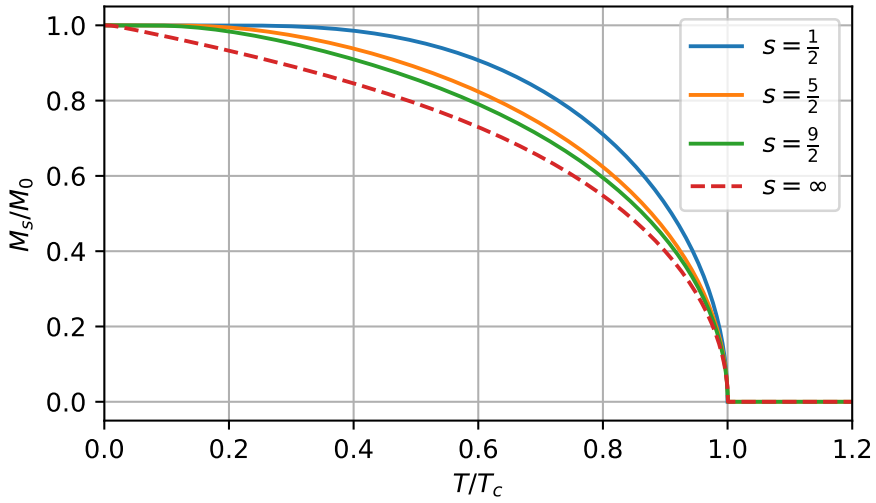

Figure 2.5: The normalized magnetization (M_s/M_0) as a function of the normalized temperature (T/T_c) from the mean field approximation for different values of atomic magnetic moment.

a magnetic system. Unfortunately, the assumption of a constant field is not valid for systems with a small number of interactions. In fact, the mean-field theory fails qualitatively in the case of one-dimensional systems. Thus computational methods may be necessary to get a better quantitative and qualitative understanding of the system.

2.4 Monte-Carlo Simulation Method

Monte-Carlo (MC) is one of the most versatile computing methods in solving specific mathematical and statistical problems, including finding the equilibrium state of a system. For our case, Monte-Carlo can be implemented by sampling the possible states by changing the direction of one spin randomly, then accepting the change in the spin by a probability $P = \exp(-\frac{\Delta E}{k_B T})$, where ΔE is the change in the energy

because of the change of that spin. This process mimics the Boltzmann distribution, and it is repeated (for all the spins) until a sufficient number of possible states is covered. MC method and its variations can be an effective computing method in searching for the equilibrium state. Unfortunately, MC does not involve the time-effect. Thus, MC is not an ideal option to study systems that are not in equilibrium or the dynamic properties of a given system. The time evolution of a magnetic system can be described by the stochastic Landau-Lifshitz LLG equation (sLLG) as discussed in Sec 2.5.

2.5 Equation of Motion

Based on the fact that a single spin precesses around an applied field, Landau and Lifshitz provided the first mathematical description of the motion a classical magnetic moment in 1935 [42]. They suggested that the motion of a magnetic dipole can be described by

$$\frac{\partial \vec{\mu}_i}{\partial t} = -\gamma \left(\vec{\mu}_i \times \vec{H}_i \right), \tag{2.5}$$

where $\gamma = \frac{g_e \mu_B}{\hbar} = 1.76 \times 10^{11}$ rad/s.T is the gyromagnetic ratio, $\vec{H}_i \cdot \hat{d} = -\frac{1}{\mu_0} \frac{\partial E}{\partial (\vec{\mu} \cdot \hat{d})}$ is the effective field observed by $\vec{\mu}_i$, and $\hat{d} = \hat{x}, \hat{y},$ or $\hat{z}$. Since the change in the magnetic moment is perpendicular to the magnetization and to the effective field, Eqn. [2.5] conserves the angle between $\vec{\mu}_i$ and $\vec{H}_i$. Thus, the equation lacks the expression of the energy dissipation associated with the damping of the spin precession where the spin tends to align parallel to the applied field over time. Gilbert has added a term that expresses that damping. By including the damping term, we obtain the Landau-Lifshitz-Gilbert equation (LLG)[43, 44]

$$\frac{\partial \vec{\mu}_i}{\partial t} = -\frac{\gamma}{(1+\alpha^2)} \left(\vec{\mu}_i \times \vec{H}_i + \alpha \vec{\mu}_i \times (\vec{\mu}_i \times \vec{H}_i) \right), \tag{2.6}$$

where α is the damping constant with a typical value between 0.001 and 0.1. Fig. 2.6 shows the motion of the magnetic moment according to the LLG equation. The

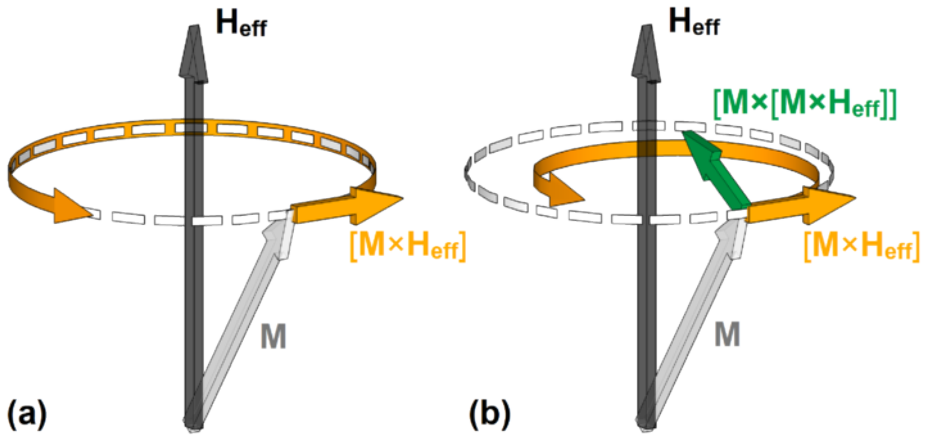

Figure 2.6: The motion of a magnetic moment according to the LLG equation. The precessional motion due to the first term (a) and a spiral motion by including the damping term (b).

larger the value of α, the faster the magnetic moment aligns with the effective field. Thus, setting α to a large value speeds up reaching the equilibrium.

The stochastic Landau-Lifshitz-Gilbert (sLLG) equation is obtained by incorporating the thermal effect in the LLG by adding a thermal field to the effective field. The thermal field is given by $\vec{H}_{th} = \sqrt{\frac{\alpha k_B T}{\gamma \mu \Delta t}}\vec{\zeta}(t)$, where Δt is the time step, $\vec{\zeta}(t)$ is a three dimensional random vector with a gaussian distribution and satisfies $\langle \zeta_d(t) \rangle = 0$ and $\langle \zeta_d(t)\zeta'_d(t') \rangle = \delta_{dd'}\delta(t-t')$, where $d, d' = x, y, z$.

2.5.1 Spin-waves

One of the consequences of the magnetic interaction between the spins and the nature of the LLG equation of motion is the spin-waves. The spin-waves are the propagating periodic variations in the direction of the spins. The spin-waves can be illustrated in the simple case of a chain of equidistant spins with a ferromagnetic coupling. An illustration of a spin wave on a chain is shown in Fig. 2.7.

By neglecting the damping term, the motion of the spins in a one-dimensional

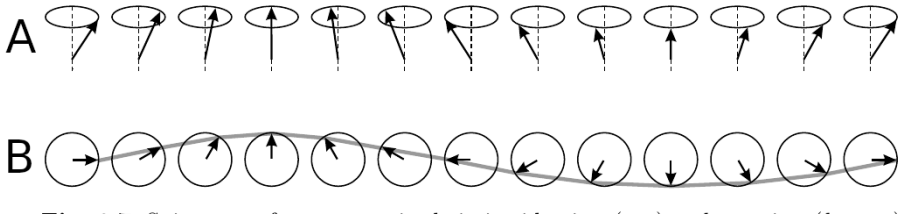

Figure 2.7: A spin wave on a ferromagnetic chain from (a) a perspective view and (b) from top view (from Ref[1]).

chain can be expressed as

$$\frac{\partial \vec{S}_i}{\partial t} = \frac{1}{\hbar} S_i \times J\left(\vec{S}_{i-1} + S_{i+1}\right). \tag{2.7}$$

Starting with the ground state with the spins aligned along the z-axis and assuming a small deviation from the ground state, we can use the approximation $S_i^z \approx S$, whereas S_i^x and S_i^y are very small. Then, the solution of Eqn. [2.7] is a wave with:

$$S_i^x = Ae^{i(qia - wt)} \tag{2.8}$$

$$S_i^y = Be^{i(qia - wt)} \tag{2.9}$$

$$A = iB \text{ (are constants)}$$

$$\hbar w = 2JS\left(1 - \cos(qa)\right),$$

where q is the wave-vector, w is the angular frequency, and a is the chain spacing. Worth noting that for very long wave-length ($q \approx 0$), the excitation energy is $\hbar w \approx 0$. Hence, a very small energy can create spin waves in this case. In the quantum form, the spin-waves are quantized by the quasi-particles (magnons). A magnon is the smallest possible disturbance of the spins from the ground state, and it corresponds to the reduction of the magnetization by $s = 1$. At low temperature, the excitation energy is small, and we can use the approximation ($\hbar w = 2JS(qa)^2/2 \Rightarrow w \propto q^2$). The density of states (D) of the spin waves in three dimensions is

$$D(q) \propto q^2 \Rightarrow D(w) \propto w^{1/2} \tag{2.10}$$

Since magnons correspond to integer spins, they follow the Bose-Einstien distribution. Thus the number of magnons is

$$n_m = \int_0^\infty \frac{D(w)}{e^{\hbar w/k_B T} - 1} dw.$$

This integral gives $n_m \propto T^{3/2}$. Since the number of magnons is proportional to the reduction in the magnetization of a ferromagnet, $M(0) - M(T) \propto T^{3/2}$.

Chapter 3

Model and methodology:

3.1 Maghemite nanoparticles: short range interactions

Maghemite has an inverse spinel structure in which each unit cell has 32 O^{2-}, 8 Fe^{3+} occupying tetrahedral sites, and $16\times(5/6)$ Fe^{3+} occupying octahedral sites. One sixth of the octahedral sites are vacant to balance the charge. Fig. 3.1 shows the crystalline structure, highlighting the position of each type of site.

The Fe^{3+} ions in both tetrahedral and octahedral sites have a magnetic moment due to their unpaired electrons. The magnetic moment of each Fe^{3+} ion is approximately 5 μ_B. The magnetic moments of Fe^{+3} ions in tetrahedral (A) sites align antiparallel to octahedral (B) sites.Since there are more octahedral sites than tetrahedral site, a perfect alignment corresponds to a net magnetization leading to a ferrimagnetic ordering.

In case of a perfect allignment, the saturation magnetization per Fe^{3+} is:

$$M_s(0) = \frac{(N_B \times 5\mu_B - N_A \times 5\mu_B)}{N_B + N_A};$$
$$M_s(0) = \frac{16 \times (5/6) \times 5\mu_B - 8 \times 5\mu_B}{16 \times (5/6) + 8} = \frac{1}{4}5\mu_B,$$

where N_B is the number of the Fe^{3+} on the octahedral sites per unit cell, and N_A is

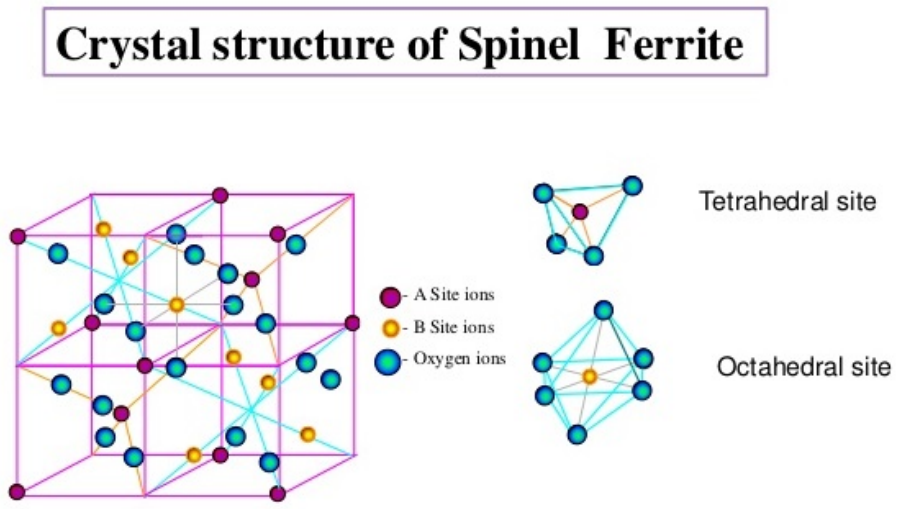

Figure 3.1: The distribution of octahedral and tetrahedral sites in the maghemite crystal.

the number of the Fe^{3+} on the tetrahedral sites per unit cell.

We describe a maghemite nanoparticle by a core-shell model that has an energy

$$E_{\mathrm{NP}} = -\sum_{\langle ij \rangle} (J_{ij} \hat{S}_i \cdot \hat{S}_j) - K_s \sum_{i \in \mathrm{surface}} (\hat{S}_i \cdot \hat{n}_i)^2, \tag{3.1}$$

where $\hat{S}_i$ is a unit vector in the direction of the spin i, and $\hat{n}_i$ is a radially oriented unit vector. The first term in Eqn. [3.1] describes the super-exchange interactions between the iron spins through the oxygen atoms. The second term in Eqn. [3.1] describes the radial surface anisotropy (K_s) of the surface spins. Since the magnetic moment per Fe cation ($g_s S = 5\mu_B$) is relatively large, we use a classical Heisenberg spin description.

The nanoparticle is constructed by cutting a sphere of 7.5 nm diameter through the maghemite lattice, where one of the tetrahedral sites is located at the center of the

sphere. This results in a nanoparticle containing approximately 6000 iron atoms and 9000 oxygen atoms. The core is defined as a sphere of 6.3 nm diameter in the center of the nanoparticle (with the rest being the surface "shell"); the surface-to-volume ratio of these nanoparticles is about 40%. The vacancies in the octahedral sites are randomly distributed and each nanoparticle has its own unique vacancy distribution. We begin by examining the magnetism of non-interacting (no dipolar interactions) nanoparticles to determine their intrinsic spin moments and overall magnetization temperature dependencies. After that, we study the dipole interactions of a triangular array of these nanoparticles and the interplay between the dipole interactions and the intrinsic interactions of these nanoparticles. The core is assumed to have bulk-like properties where the super-exchange between nearest neighbour, J_{TT}, J_{OO}, J_{OT}, is -42, -17.2, and -56.2 K between tetrahedral-tetrahedral sites, octahedral-octahedral sites, and octahedral-tetrahedral sites, respectively [2, 45, 46]. The surface exchange (super-exchange) constants were set to 1/40 of that in the bulk maghemite to match the experimental results of the increase in the saturation magnetization at low temperatures [47, 48].

The experimental results of maghemite nanparticles [48] show a rapid increase in the magnetization below 25 K ($\approx 1/40$ of the order temperature of bulk maghemite). As we will show in the next chapter, our model suggest that this increase in the magnetization is due to the order of the surface spins. Thus, the ratio of the saturation magnetization near 0 K to the saturation magnetization above the temperature of the rapid increase in the magnetization (25 K), corresponds to the ratio of the number of the nanoparticle atoms to the number of the core atoms. Using this ratio from the experimental results suggests a surface thickness of 0.62 nm. We set the core diameter in our model to be 6.3 nm, leaving a surface thickness of 0.62 nm.

The bulk exchange constants were determined from magnetization and Mössbauer spectroscopy measurements on bulk maghemite using mean-field theory[49, 50, 51, 52]. However, the mean-field theory neglects fluctuations and usually overestimates the

Curie temperature in comparison with Monte Carlo and stochastic Landau-Lifshitz-Gilbert (sLLG) methods. In the case of three-dimensional systems, the Curie temperature estimation from the mean-field theory is about 35% higher than the numerical calculations. In addition to that, we use a unit vector instead of the spin value in our model. Using the unit-vectors reduces the exchange energy by a factor of s(s+1) = 8.75 if the exchange parameters were kept the same. Thus, we have rescaled the exchange parameters by a factor of $1.3 \times s(s+1) \approx 12.5$ so that the Curie temperature from the simulation results yields reasonable agreement with the experimentally extrapolated values.

All the simulations in this thesis use the stochastic Landau-Lifshitz-Gilbert equation to describe the motion of the dipole or the spin magnetic moment. The sLLG equation was integrated for each of the individual atomic spins in each of the nanoparticles in steps of 4×10^{-4} tu, where $1\,\mathrm{tu} = 1.9 \times 10^{-11}\,\mathrm{s}$. To improve the numerical accuracy or to reduce the required computing time, the 4th order Runge-Kutta algorithm was used (in comparison with lower order integration schemes). To determine the temperature dependence of the magnetization, the nanoparticle was cooled in the absence of an external field from a random magnetic configuration at 1000 K to 0 K in steps of 2 K at a rate of 0.1 K/tu. Starting the simulations with random magnetic configurations at a temperature (1000 K) that is above the ordering temperature reduces the chance of getting the nanoparticle stuck in a meta-stable state. To speed up reaching the equilibration, the damping factor (α) was set to 0.5 for all the simulations of the temperature dependence. The simulations of maghemite nanoparticles and arrays were performed using the micromagnetics scripting language MagLua [53].

Using sLLG means that we assume that the spins are classical vectors which ignores quantum effects. At low temperature (typically well below 10 K), the quantum tunneling allow the spins to access high energy states that are rarely accessible by thermal excitation. Hence, a real quantum model never reaches the ground state at 0 K. At high temperatures, thermal fluctuations increase, causing decoherence

between quantum states. This decoherence means that the distinct quantum phases and interference effects that typically distinguish quantum states are lost, or smeared. As a result, the system's quantum nature becomes less pronounced and there is no significant difference between the quantum and the classical model.

Another aspect that differentiates the two models is the uncertainty in quantum spins. The uncertainty in the spin components along the x- and y-axes, perpendicular to the quantization axis z is $S_x^2+S_y^2$. The expectation value is $\langle S_x^2+S_y^2\rangle = \langle S^2\rangle - \langle S_z^2\rangle$, where: $\langle S^2\rangle = S(S+1)\hbar^2$ is the total spin magnitude, and $\langle S_z^2\rangle = m^2\hbar^2$ where m is the magnetic quantum number. Hence, $\langle S_x^2 + S_y^2\rangle = S(S+1)\hbar^2 - S^2\hbar^2 = S\hbar^2$ This shows that the perpendicular uncertainty is proportional to S.

To compare the quantum result with classical expectations, we normalize the uncertainty by dividing by the total spin magnitude squared $\langle S^2\rangle$:

$$\frac{\langle S_x^2 + S_y^2\rangle}{\langle S^2\rangle} = \frac{S\hbar^2}{S(S+1)\hbar^2} = \frac{S}{S(S+1)} \sim \frac{1}{S+1}$$

. As S becomes large, the ratio $\frac{1}{S+1}$ tends to zero, which implies that the uncertainty in the spin components S_x and S_y becomes negligible compared to the total spin S. This calculation is for a single spin, in a nanoparticle of thousands of spins, the uncertainty becomes negligible (in term of the net magnetization).

3.2 Maghemite nanoparticles: long range interactions

To describe the long-range dipole interactions in the triangular array of these nanoparticles, we use the point dipole approximation. In this approximation, the dipole field is calculated by representing each nanoparticle as a magnetic dipole at its centre, where the magnetic moment of the dipole equals the magnetic moment of the corresponding nanoparticle. We construct an $L \times L$ triangular array with a lattice parameter a. Hence, the nanoparticles are located at sites $n_1\vec{a_1} + n_2\vec{a_2}$, where $\vec{a_1} = a(1,0,0)$, $\vec{a_2} = a(1/2, \sqrt{3}/2, 0)$, and n_1 and n_2 are integers between 1 and L. To account for the

long-range interactions in the array, we impose periodic boundary conditions by using the Ewald summation method[54]. The periodic boundary conditions mean that the array is equivalent to a system that fills the entire plane with repeated configurations, as shown in Fig. 3.2.

is rapeated to infinity in order to calculate The dipolar energy of a triangular array of $L \times L$ dipoles is given by

$$E_d = \frac{1}{2} \sum_{k}^{L^2} \sum_{l}^{L^2} \sum_{\alpha,\beta=1}^{3} \sigma_k^{\alpha} \left(g_{k,l} \Gamma_{k,l}^{\alpha,\beta} \right) \sigma_l^{\beta}, \tag{3.2}$$

where $\Gamma_{k,l}^{\alpha,\beta}$ is an element of a 3×3 tensor that depends only on the relative position $(\vec{r}_{k,l}/a)$ between the sites k and l in the array, σ_k^{α} is a Cartesian component of the normalized magnetic moment of the nanoparticle at site k, and $g_{k,l} = \mu_0 m_k m_l / 4\pi a^3$ is the dipole interaction strength, where m_k denotes the magnitude of the dipole moment of the nanoparticle at the site k, and μ_0 is the vacuum permeability. Therefore, the

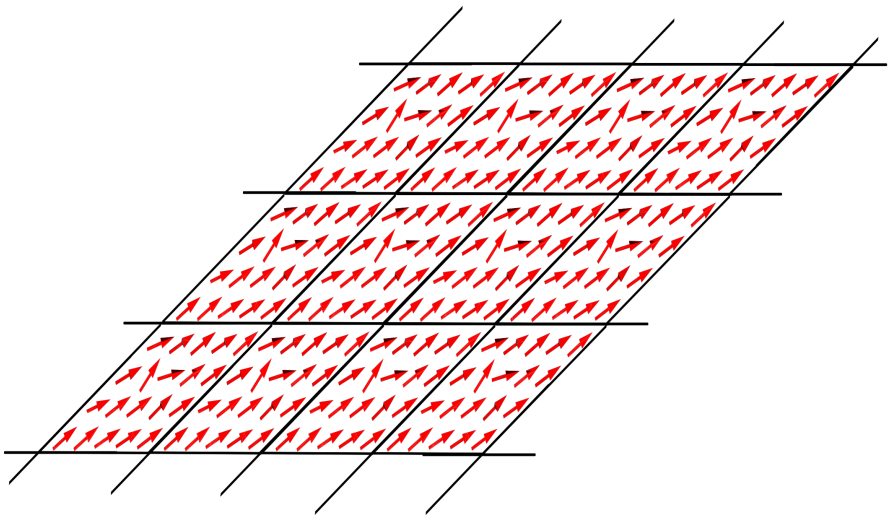

Figure 3.2: Illustration of 5×4 triangular array with periodic boundary conditions. The system consist of identical copies of the magnetic configuration of the array (contained in a parallelogram).

energy of a triangular array of the nanoparticles is

$$E = \frac{1}{2}\sum_{k}^{L^2}\sum_{l}^{L^2}\sum_{\alpha,\nu=1}^{3}\sigma_k^{\alpha}\left(g_{k,l}\Gamma_{k,l}^{\alpha,\nu}\right)\sigma_l^{\nu} + \sum_{q}^{L^2}E_{\mathrm{NP}}^{q}, \tag{3.3}$$

where E_{NP}^{q} is the energy due to the short-range interactions in the nanoparticle on the site q in the array as defined in Eqn. [3.1]. The random vacancy distribution on the octahedral sites and the orientation of the maghemite unit cell are unique for each nanoparticle.

To validate our sLLG approach and to determine the nature of the magnetic order due to the dipole interactions in triangular arrays, we first performed simulations of simple dipoles in different sized triangular arrays. Each ensemble consisted of 500 arrays of simple point dipoles, where the array size was $L = 8$, 16, 24, or 32. For the purposes of universality and comparison between different systems, we define the reduced temperature as $\tau = Tk_B/g$, where $g = \mu_0 m^2/4\pi a^3$ and m is the magnitude of the dipole moment. The simulations begin with random magnetic configurations at $\tau = 1$. The magnetization and the energy were determined as a function of the reduced temperature τ as the temperature was decreased from $\tau = 1$ to 0 in steps of 0.02. The arrays were left to equilibrate at each temperature step for 1000 ξ and the data were recorded for another 1000 ξ after equilibration for statistical averaging where, $\xi = m/\gamma g$, is the normalized time unit.

To study the interplay that results from the surface anisotropy and dipole interactions between nanoparticles in a triangular array, simulations of an array size L=24 and lattice parameter a=7.5 nm were carried out. The array was cooled from 55 K to 0 in steps of 5 K, and the simulation was repeated for radial anisotropy constants K_s/k_B=0, 5, and 10 K. The array was left to equilibrate from 2500 to 7500 time unit for each temperature step and the statistics were collected for the same amount of time after equilibration. For comparison, the same process was conducted for an array of simple dipoles (with no anisotropy) where each dipole was given the average magnitude of the magnetic dipole of the individual nanoparticles at any tem-

perature. For the nanoparticle arrays, the message passing interface, MPI, was used where each nanoparticle was assigned to a single core-processor. The dipole field at each nanoparticle was updated every 12 time-steps to reduce the communication time between processors. The simulations were conducted using the Graham and Cedar computing clusters [1].

3.3 Triangular arrays: spin-wave calculations

To study the spin-waves, we use the spin configurations at 5 K from the nanoparticle array with $K_s/k_B = 5$ K as the initial configurations. We let the array to relax for 5000 tu with $\alpha = 0.5$ at 1 K. After that, the data was recorded for 21000 tu with $\alpha = 0.0001$. The small value of α ensures that the effect of the thermal fluctuations on the precession of the magnetic moments is small. Using the final spin configuration as initial conditions, the same simulation process was repeated for $K_s/k_B = 0, 1, 2.5, 3.5,$ and 6.5 K. The resulting 21000 tu for each value of K_s was divided into five partially overlapping windows of 7000 tu. Each window was processed separately, and the final results were averaged over the windows to improve the statistics.

Since the average magnetization over time corresponds to zero-frequency, it does not contribute to the spin-waves. So, we subtract the average magnetization (over each time-window) of each nanoparticle from the nanoparticle magnetization before performing the spin-wave calculations. So, the magnetization that is used for the spin-wave analysis is given by

$$\vec{M}_{i,j}(t) = \vec{M'}_{i,j}(t) - < \vec{M'}_{i,j} >_t, \tag{3.4}$$

where $\vec{M'}_{i,j}(t)$ is the original magnetization of the nanoparticle (i, j) at time (t).

Using the spatial Fourier transform, we obtain the time dependence of the spin

[1]This research was made possible in part by the allocation of resources on these clusters, which are part of the Digital Research Alliance of Canada: https://www.alliancecan.ca

waves for each wave-vector ($\vec{q}$) as

$$\vec{M}(\vec{q},t) = \sum_{j=1}^{L^2} \vec{M}(\vec{r_j},t)\exp[i\{(n_1/L)\vec{b_1} + (n_2/L)\vec{b_2})\}.\vec{r_j}]; \tag{3.5}$$

$$\vec{q} = n_1\vec{b_1} + n_2\vec{b_2};$$

$$\vec{b_1} = \frac{2\pi}{a}(1,-1/\sqrt{3}), \quad \vec{b_2} = \frac{2\pi}{a}(0,2/\sqrt{3}),$$

where $\vec{b}_1$ and $\vec{b}_2$ are the primitive vectors of the reciprocal array of a triangular array, and n_1 and n_2 are integers in the range $[0, L-1]$. To obtain the spectra of the spin-waves (the amplitude vs the frequency), we calculate the Fourier transform of $\vec{M}(\vec{q},t)$ in the frequency domain using

$$\vec{M}(\vec{q},f_l) = \sum_{j=0}^{N_t-1} \vec{M}(\vec{q},t_j)\exp[i\{2\pi f_l w_l t_j\}]h(j); \tag{3.6}$$

$$t_j = T_t\frac{j}{N_p},$$

$$f_l = \frac{1}{T_t}\frac{l}{N_p},$$

$$h(j) = \sin^2(\frac{\pi j}{N_p}),$$

where T_t is the total time of the window, N_p is the total number of the recorded points during one time-window, l is an integer in the range $[0, N_t]$, f_l is the frequency, and h is the Hanning function. The convolution with the Hanning function is included to reduce the spectral leakage that is generated by the discontinuity at the boundaries of the time-window.

From $\vec{M}(\vec{q},f_l)$, we obtain the amplitude as a function of the frequency for the three components of the spin-waves for each value of the wave-vectors $\vec{q}$. We average the amplitude of each component of the spin-wave over the windows (for every value of $\vec{q}$ and f_l) to reduce the noise.

For comparison, the previous process and analysis were applied to a simple dipole array with no anisotropy. The average amplitude of the magnetization of the indi-

vidual nanoparticles was assigned to each dipole. Like the nanoparticle array, the distance between the neighbouring dipoles is 7.5nm.

Chapter 4

Maghemite Nanoparticles on a Triangular Array

4.1 Maghemite Nanoparticles

First, we examine the magnetic order of individual maghemite nanoparticles due to the superexchange and the surface anisotropy. Fig. 4.1 shows the core ($m_c(T)$) and the total magnetization ($m_n(T)$)) of a nanoparticle with a diameter of 7.5 nm as a function of temperature obtained using the sLLG simulations. The core spins order at 850 K, comparable to the experimentally extrapolated value for bulk maghemite[51], and for temperatures below 50 K the core spins are (effectively) aligned fully. Below 30 K, the core spins are fully aligned, but the nanoparticle magnetization increases rapidly with decreasing temperature due to the order of the surface spins, as shown in Fig. 4.1. This is in good agreement with previous simulations of 5 nm nanoparticles (inset of Fig. 4.1)[2] that were in agreement with previous Monte-Carlo simulations and experimental observations [47, 48].

The ground state due to the super-exchange is ferrimagnetic where the spins of the octahedral sites are parallel to each other and anti-parallel to the spins on the tetrahedral sites. This is consistent with the experiments where the magnetization

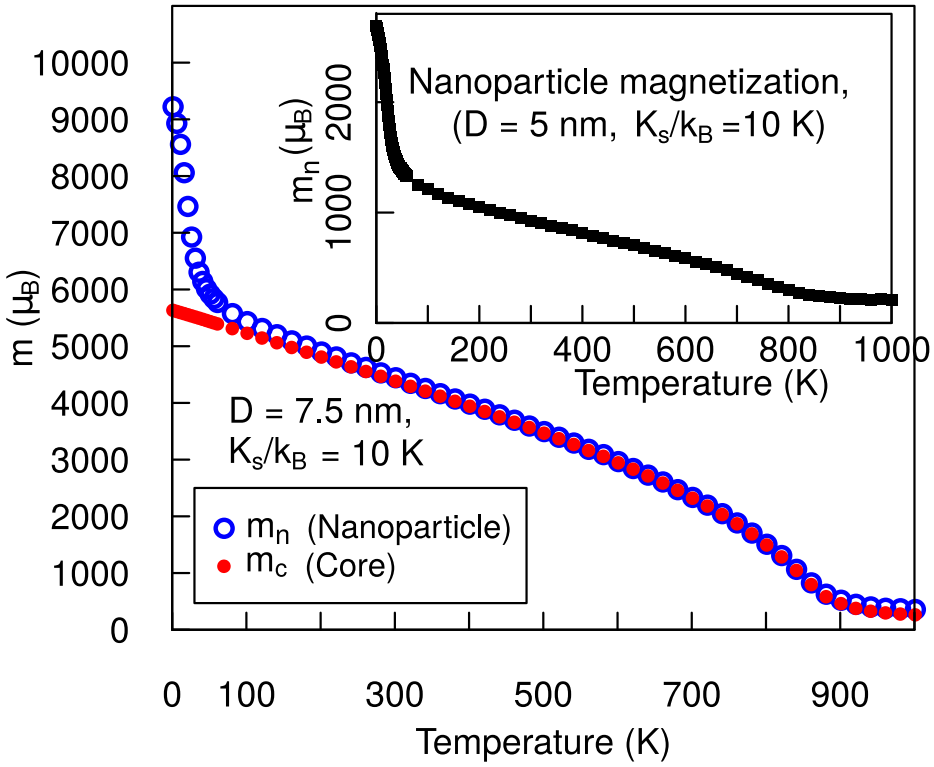

Figure 4.1: The total and the core magnetization of a 7.5 nm diameter nanoparticle as a function of temperature. Previous results of $m_n(T)$[2] for a 5 nm diameter nanoparticle are shown in the inset.

is found to be the result of two anti-parallel sublattices with a ratio of 0.6 between the number of spins on each sublattice. On average, a unit cell of maghemite has 8 tetrahedral sites and $16 \times (5/6)$ octahedral sites. Thus, the average (effective) magnetization per iron atom is $\frac{16\times(5/6)-8}{16\times(5/6)+8} \times 5\mu_B = 5/4\mu_B$.

Fig. 4.2 shows the magnetic moment of the 7.5 nm diameter nanoparticle for K_s/k_B=0, 5, and 10 K at low temperatures. The core spins are fully aligned below 60 K, and below 15 K the surface spins are relatively well ordered. Since the super-exchange between the surface spins is chosen to be 1/40 of the corresponding interactions between the core spins, we expect the surface spins to order below a tem-

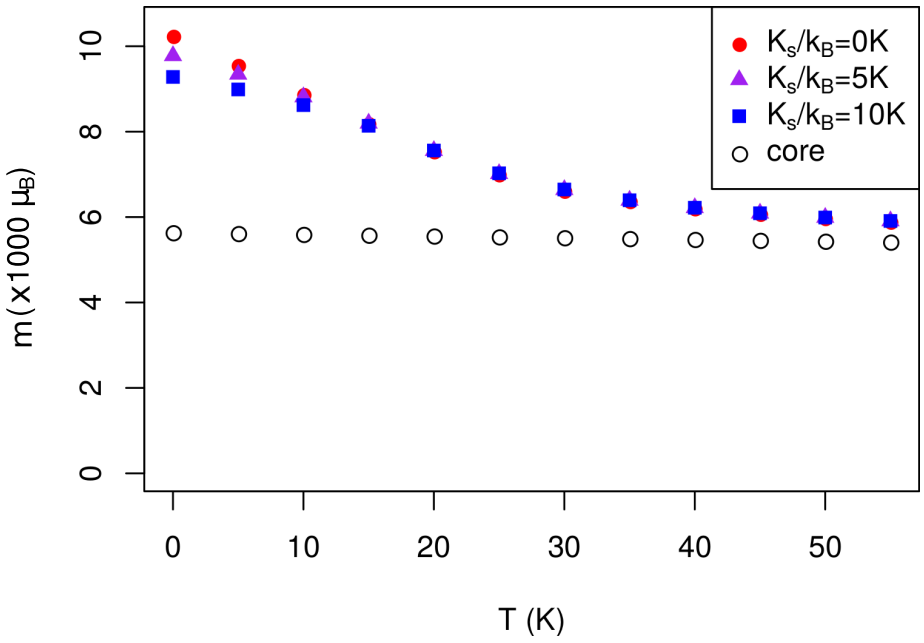

Figure 4.2: The magnetic moment of individual nanoparticles as a function of temperature for various values of K_s. The open circles are the core magnetic moment which is saturated at low temperatures and is independent of K_s.

perature of $850/40 \simeq 21$ K. We note that the surface spins start to order at a higher temperature than that (around 30 K). The order of the surface spins at a relatively high temperature is due to the interactions of the surface spins with the well-ordered core spins. These interactions result in an increase in the effective field observed by the surface spins. We find that the nanoparticle's magnetization decreases with increasing K_s, suggesting that the surface radial anisotropy reduces the alignment between surface spins. This can be understood by referring to the surface anisotropy term in Eqn. [3.1]. The energy due to the surface anisotropy is minimal when the surface spins are radially oriented (inward or outward). Fig. 4.3 shows an illustration of the magnetic configuration of a nanoparticle at 0 K. The core spins are well aligned with each other, whereas the surface spins have a tendency to align perpendicular to

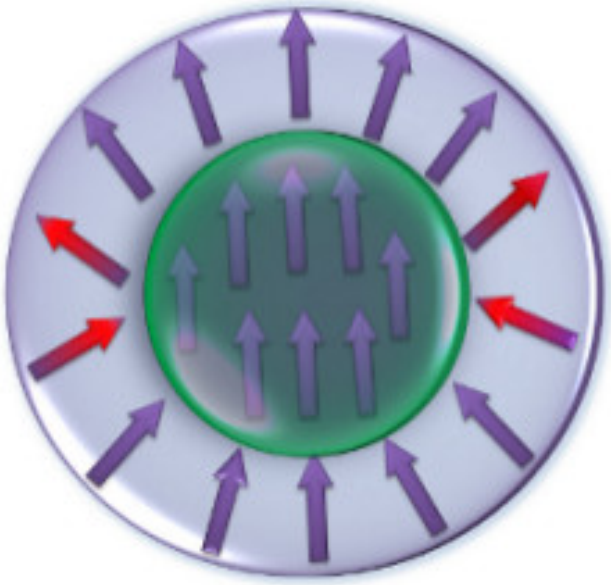

Figure 4.3: An illustration of the magnetic configuration of a maghemite nanoparticle with surface anisotropy.

the surface. According to Eqn. [3.1], this tendency increases as K_s increases, resulting in a decrease in the surface net magnetization.

4.2 Dipole Arrays

To study the interplay between the intra-particle interactions discussed in Sec. 4.1 and the dipole interactions in a triangular array of nanoparticles, we need to determine the nature of the magnetic order due to the dipole interactions in triangular arrays. Thus, we study the effect of dipole interactions in triangular arrays of simple point dipoles. Fig. 4.4 shows the normalized magnetization as a function of the reduced temperature ($\tau = Tk_B/g; g = \mu_0 m^2/4\pi a^3$) for various array sizes, where each array has $L \times L$ dipoles. The arrays order ferromagnetically below a critical temperature. We note that the magnetization at high temperature depends on the array size. The size effect

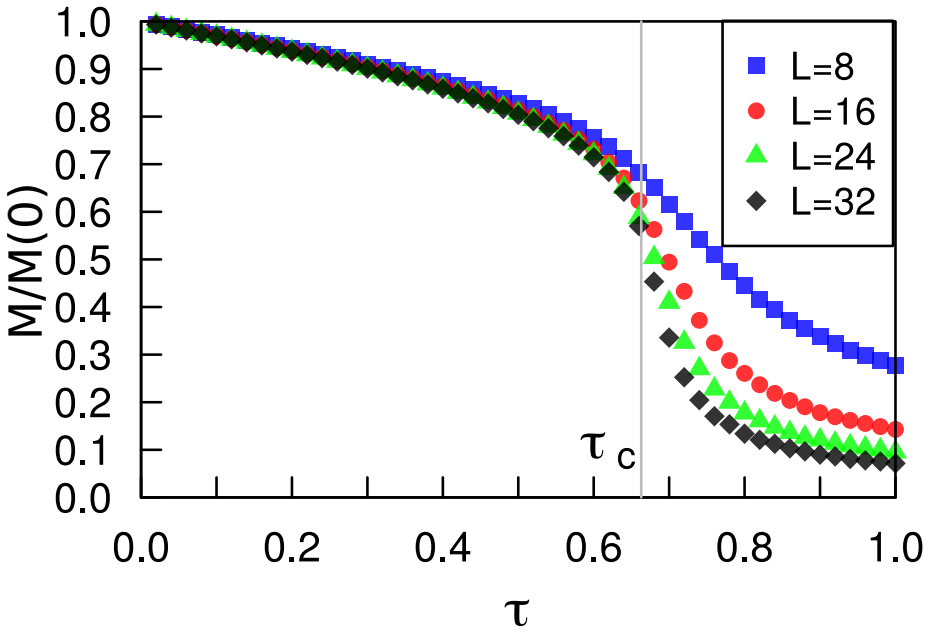

Figure 4.4: The magnetization for different sizes of the triangular array of magnetic dipoles as a function of reduced temperature ($\tau = Tk_B/g$).

can be understood by considering the statistical effect for small arrays, where a fully random spin configuration would yield a net magnetization $M \propto 1/\sqrt{L^2} = 1/L$.

Since the array is repeated periodically, each dipole observes the field from its copies, where the copies have the same direction as the original dipole, and they are separated from it by distances that are proportional to L. For illustration, Fig fig:periodic shows a tringular array with periodic boundary cnditions. The strength of the dipole interaction between these copies increases by reducing L (The copies become closer to the origin). Thus, the magnetic order increases with decreasing L as Fig. 4.4 shows.

We find that at low temperatures $M(0) - M(T) \propto T$, where $M(0)$ corresponds to the ferromagnetic alignment at 0 temperature. This linearity is a characteristic of the classical Heisenberg model that we used to represent the dipoles (i.e. classical 3-

dimensional dipoles)[55, 56, 57]. Our simulations identified that the net magnetization remains effectively in-plane once the array starts to get ordered.

The correlation length ξ measures the distance over which fluctuations in a system are correlated. Near the critical temperature, ξ becomes very large, indicating that fluctuations are correlated over long distances. In finite systems, however, ξ is constrained by the system size L. By rescaling ξ to account for this limitation and using the critical scaling components, it can be shown that the Binder parameter ($B =< M^4 > / < M^2 >^2$)[58] becomes independent of system size at the critical temperature.

Fig. 4.5 shows B as a function of the reduced temperature. Since the Binder parameter is independent of the array size at the critical temperature (τ_c), the point where all the lines cross each other corresponds to τ_c. We find the critical temperature, $\tau_c \simeq 0.663$, in good agreement with previous Monte-Carlo simulations by Tomita ($\tau_c \simeq 0.6639$)[37]. Previous studies[59] of dipole interactions in triangular arrays of planar spins (the spins are restricted to be in-plane) showed a phase transition at $\tau_c \simeq 0.88$, which is slightly higher than our results for Heisenberg classical three-dimensional spins; out-of-plane fluctuations for the Heisenberg case can occur and suppresses τ_c.

We found the ferromagnetic ground state to have energy-per-site, $E/g \simeq -2.757$, in agreement with previous studies ($E/g \simeq -2.758$)[60, 61]. The ground state energy is independent of the direction of the net magnetization as long as the dipoles are parallel and in-plane. Since the dipole-dipole interactions act like a planar anisotropy (force the spins to remain in-plane), our Heisenberg spin model and the planar spin model have identical ground state energies as pointed out by Rastelli et al.[59]. While the dipolar energy, given by Eqn. [3.2], is not invariant under a uniform rotation of the spins, its ground state is nevertheless continuously degenerate. This property is common to a number of two dimensional dipolar systems such as Honeycomb and triangular arrays[62].

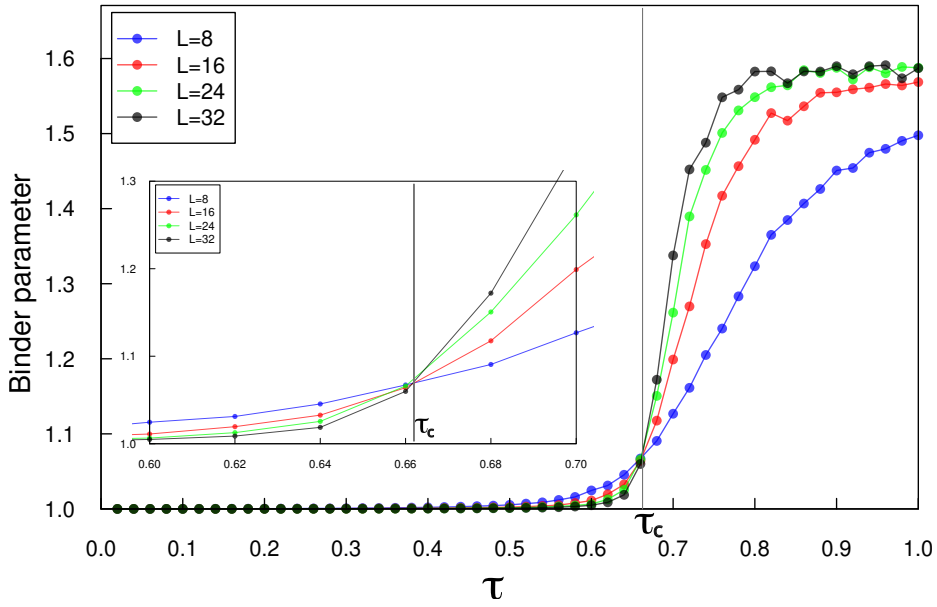

Figure 4.5: The Binder parameter for different sizes of the triangular array of magnetic dipoles as a function of reduced temperature.

By introducing some perturbation from the ground state, the anisotropic nature of Eqn. [3.2] may result in preferring certain in-plane directions for the net magnetization. This effect is known as order-from-disorder and can be induced by perturbation due to thermal fluctuations or structural disorder[63, 64, 65, 66].

Indeed, the simulations reveal a preference for certain in-plane directions at $\tau > 0$. To illustrate this, we measure the direction of the net magnetization at equally spaced time intervals and plot the corresponding point on the $x-$ and $y-$axes (the array's plane). Fig.4.6 shows the observed directions of the net magnetization of a triangular array of magnetic dipoles with $L = 32$ at $\tau = 0.4$, where each point corresponds to one of the measurements. We define the x-axis as the primitive vector $\vec{a_1}$, and ϕ as the angle between $\vec{a_1}$ and the net magnetization. We note that the array magnetization prefers to be in one of the directions $\phi = 30°, 90°, 150°, 210°, 270°$. This is consistent with the theoretical calculations for the planar spin system[63, 64, 59].

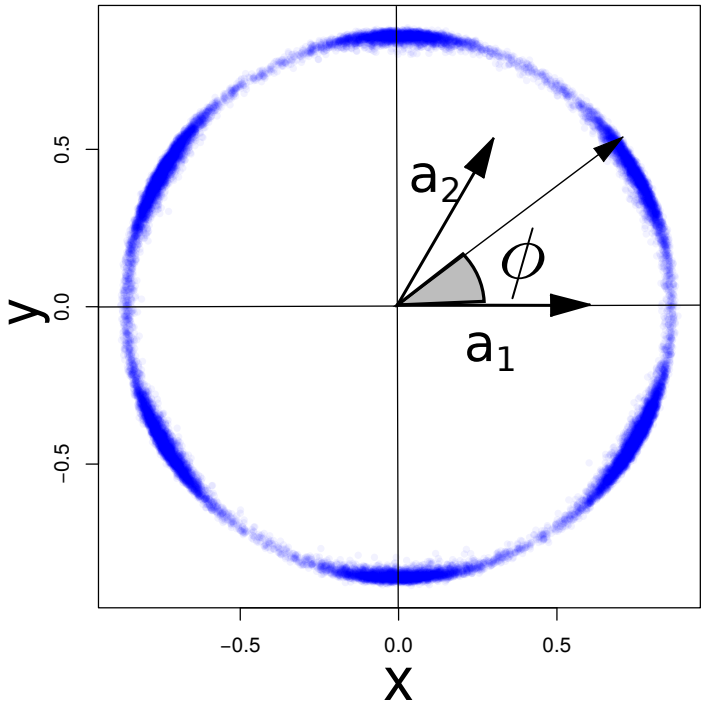

Figure 4.6: The in-plane direction of the net magnetization of a triangular array of magnetic dipoles with $L = 32$ at $\tau = 0.4$. Each point corresponds to one measurement.

We have performed the same calculation for the Heisenberg case by expanding the free energy in terms of harmonic excitations for several values of L, and the predicted preferred directions match the simulation results (the detailed calculations are discussed in Appendix A). We also found that the free energy barrier per site was dependent on the array size, as shown in Table 4.1. To calculate the energy barrier from the sLLG simulations, we record 2000 measurements of the direction of the net magnetization of each array in the ensemble at equally spaced time intervals. We divide the planar angle ϕ between the net magnetization and $\vec{a}_1$ into sectors of 2 degrees and determine n_ϕ, the number of times the net magnetization is found to be in each sector. Fig. 4.7 shows n_ϕ at various reduced temperatures. We find that the

Table 4.1: The free energy barrier per site in units of τ for various array sizes as calculated from the expansion in term of the harmonic excitations.

L	8	16	32	64	128
$\Delta f/\tau$	0.0344	0.0242	0.0205	0.0194	0.0190

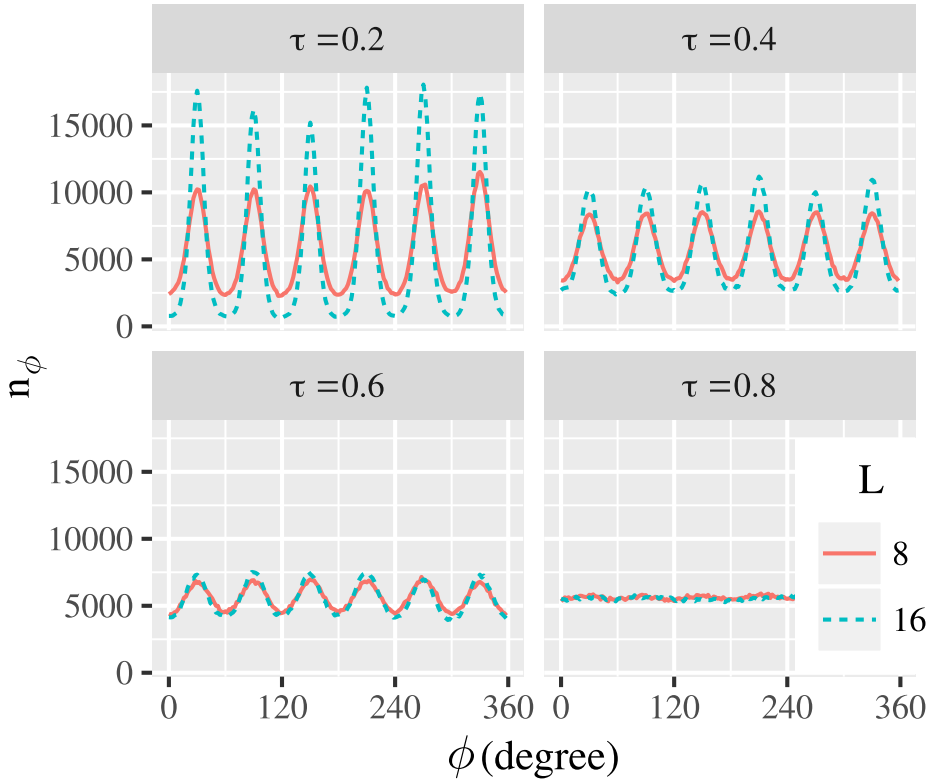

Figure 4.7: Histogram of the angle between the net magnetization and $\vec{a}_1$ for array sizes $L = 8$ (red) and 16 (blue).

direction of the net magnetization exhibits a six-fold symmetry and prefers to be at a 30° angle with respect to the primitive vectors [67].

At low temperatures, our arrays of Heisenberg classical spins behave like the arrays of planar spins[59]. Given that the planar anisotropy has a six-fold symmetry, we

averaged over angles that were separated by 60^o intervals to improve the statistics. The probability of the net magnetization being in a given sector is well approximated by n_ϕ/n, where n is the total number of measurements. Since the Boltzmann factor $\exp(-f_\phi L^2/\tau) \propto n_\phi/n$ where f_ϕ is the effective free energy per site in units of g, then $f_\phi/\tau = -\ln(n_\phi/n)/L^2 + c$, where c is a constant. Fig. 4.8 shows $-\ln(n_\phi/n)/L^2$ as a function of ϕ at $\tau = 0.04$ for sizes L=8 and 16. The effective free energy barrier per site can be estimated from the difference between the maximum and minimum values, given by $\Delta f_\phi/\tau \simeq 0.0330$ for L=8, and $\Delta f_\phi/\tau \simeq 0.0232$ for L=16, in a good agreement with the predictions given in Table 4.1.

While the net magnetization in our system remains in-plane below τ_c, the individual dipoles are not necessarily in-plane. This difference is important for nanoparticle arrays as we will see later.

4.3 Triangular Nanoparticle Array

So far, we have determined the nature of the magnetic order due to super-exchange and surface anisotropy in individual maghemite nanoparticles, as well as the dipole interactions in triangular arrays of simple dipoles. To study the interplay that results from these interactions, simulations of an array of maghemite nanoparticles were carried out. The dipole-dipole interactions between nanoparticles were dealt with as discussed in Sec. 3.2.

Fig. 4.9 presents the temperature dependence of the average magnitude of the array magnetization per nanoparticle, $M(T)/L^2$, as a function of temperature. While the magnetization of each individual nanoparticle was relatively large at 45 K due to the ordering of core spins as shown in Fig. 4.2, the net magnetization of the triangular array per nanoparticle is significantly less due to the lack of alignment of the nanoparticle magnetizations.

Since the nanoparticle magnetization, $m_n(T)$, increases significantly with cooling

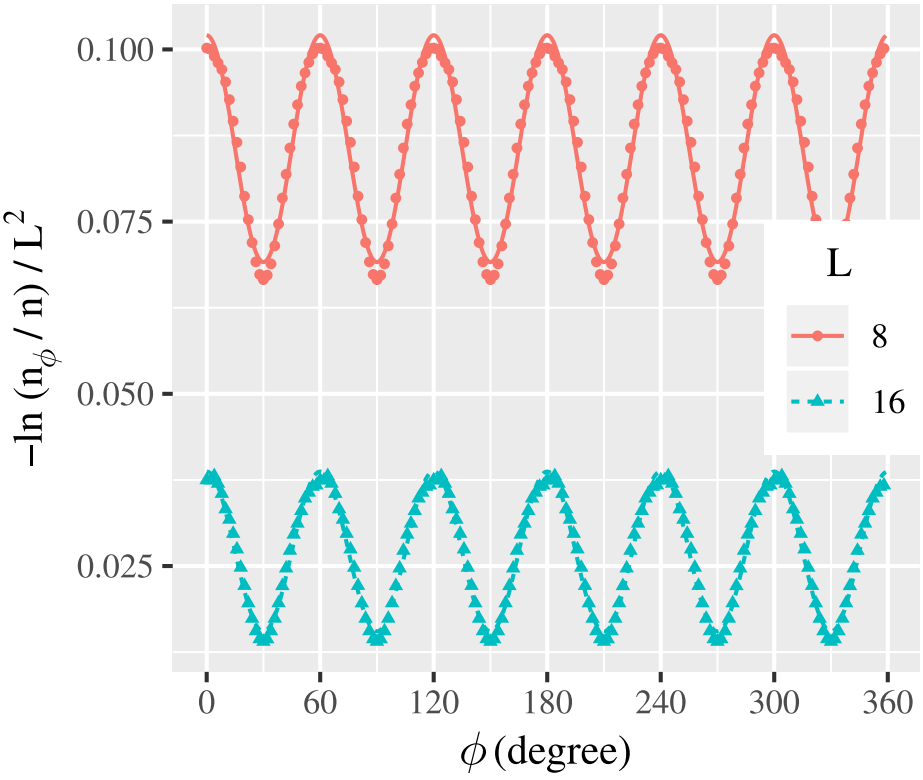

Figure 4.8: $-\ln(n_\phi/n)/L^2$ as a function of ϕ for ensembles of dipole arrays at $\tau = 0.04$, $L = 8$ (red) and 16 (blue). The points are the simulation results and the line is a fit with a cosine function as a guide to the eye.

below 25 K (Fig. 4.2) the strength of the dipole interactions between the nanoparticles, $g(T) = \mu_0[m_n(T)]^2/4\pi a^3$, is strongly temperature dependent. Due to finite size effects, the simple dipole array discussed previously with $L = 24$ started to order at a reduced temperature $\tau \simeq 0.8$, higher than τ_c. For the nanoparticle array, this corresponds to

$$\begin{aligned} &\tau = Tk_B/g(T) = 0.8 \Longrightarrow T \simeq (1.18 \times 10^{-6}) m_n(T)^2 \\ &T \simeq 44 \text{ K}, \\ &m_n(T = 44 \text{ K}) = 6100\ \mu_B \end{aligned} \tag{4.1}$$

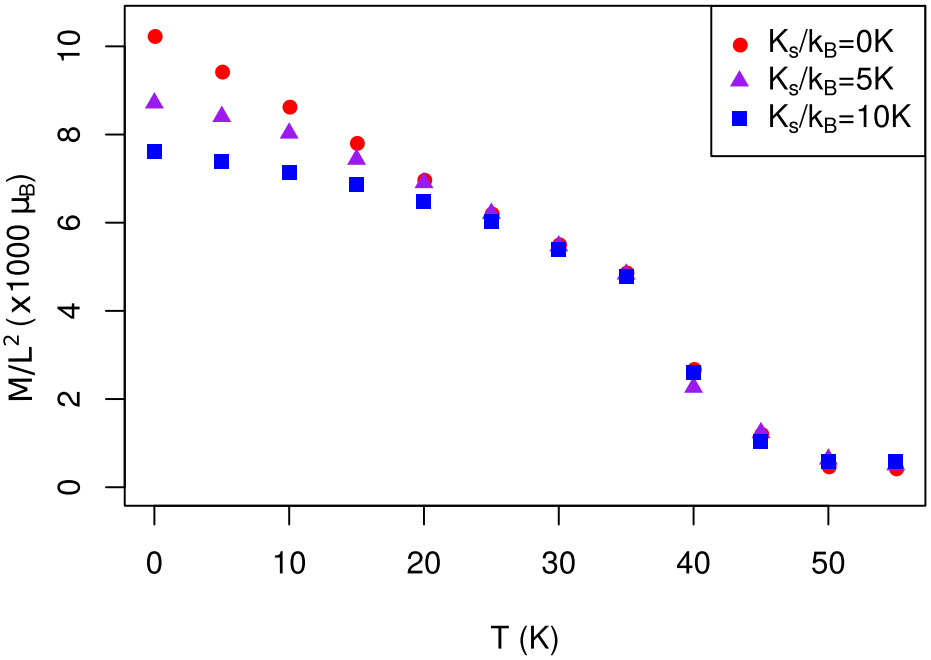

Figure 4.9: The temperature dependence of the nanoparticle array net magnetization per site for different values of K_s.

For temperatures below 25 K, Fig. 4.9 shows that M/L^2 decreases with increasing K_s. While some of this decrease may be attributed to the decrease in the surface magnetization with increasing K_s, this is not the whole story. To understand this, we define an order parameter $\eta = M(T)/[L^2 m_n(T)]$ and a reduced temperature $\tau = Tk_B/g(T)$. Plotting the order parameter η as a function of the reduced temperature τ, as shown in Fig. 4.10, removes the dependence of the data on the net magnetic moment of the nanoparticles. The plots of the rescaled data shown in Fig. 4.10 show that the nanoparticles with no surface anisotropy (K_s=0) behave as simple dipoles. For $K_s \neq 0$, the order parameter $\eta(\tau)$ falls below the curve of the simple dipoles at low temperature ($\tau < 0.22$ for $K_s/k_B = 5\,\mathrm{K}$ and $\tau < 0.35$ for $K_s/k_B = 10\,\mathrm{K}$. While there is no obvious difference between the nanoparticle array and the dipole array near the array ordering temperature, the nanoparticles have some attributes that are

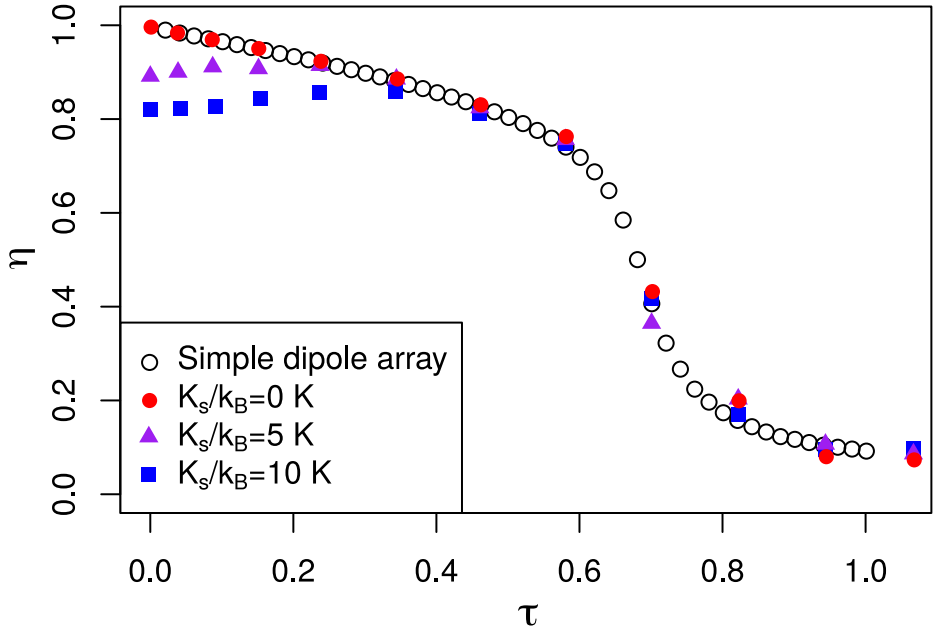

Figure 4.10: The order parameter as a function of the reduced temperature for dipole and nanoparticle arrays with $L = 24$.

different from simple dipoles. These differences may alter the critical behaviour of the nanoparticle array. For example, the presence of an effective surface anisotropy may shift the nanoparticle array further from the behaviour of planar dipoles. In our case, this nanoparticle anisotropy is negligible at the array ordering temperature due to the lack of magnetic order at the surface, as discussed later. Furthermore, the magnitude of the nanoparticle magnetizations fluctuates slightly due to thermal excitations. These fluctuations introduce additional degrees of freedom and may change the universality of the critical behaviour. We speculate that the differences mentioned above between the the nanoparticle array and the dipole array are negligible for the chosen parameters. Unfortunately, obtaining statistically meaningful data to explore the critical behaviour of the nanoparticle array demands a simulation time beyond what is currently feasible.

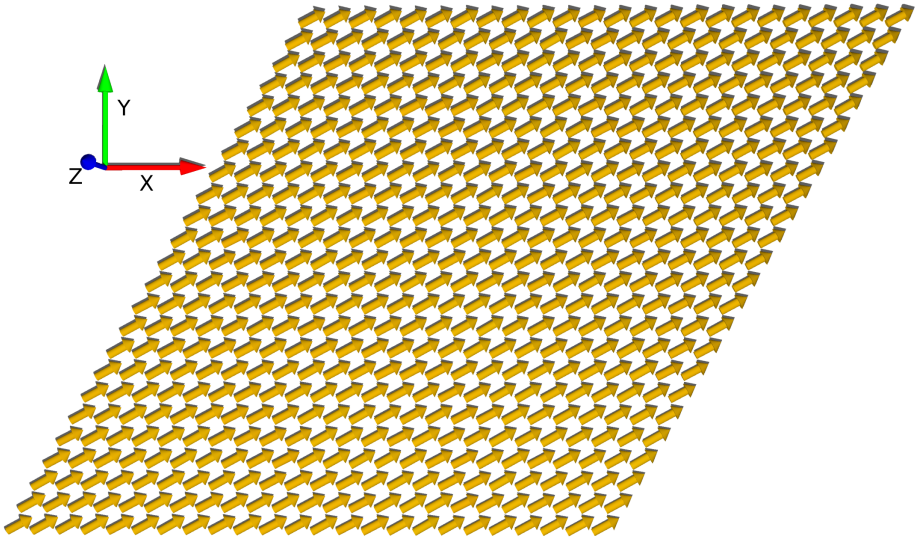

Figure 4.11: The magnetic configuration of nanoparticle arrays with $K_s = 0$ and $L = 24$ at $T = 0$. Each arrow represents the magnetization of one nanoparticle. The directions of the arrows are color-coded using a composition of red, green, and blue colors to represents the x-,y- and z-components (see the main axes on the top left). The golden color of the arrows is the result of mixing red (x-component) with some green (y-component).

The effect of the surface radial anisotropy on η can be illustrated by comparing the magnetic configuration of an array of nanoparticles for $K_s = 0$ at $T = 0$ (τ=0) as shown in Fig. 4.11 (each arrow represents the magnetization of one nanoparticle) with the corresponding magnetic configuration of the same array for $K_s/k_B = 5\,\mathrm{K}$ and $10\,\mathrm{K}$ as shown in Fig. 4.12. Each of the configurations was obtained after cooling the array from 55 K to 0. In the case of $K_s = 0$, cooling the array relaxes to a ferromagnetic state in which the nanoparticles are perfectly aligned ferromagnetically along one of the six preferred directions determined by the thermal fluctuations, as discussed in Section 4.2, giving an order parameter $\eta = 1$ for $\tau = 0$. The corresponding magnetic configurations for the case of $K_s \neq 0$ show a much more complex structure with

out-of-plane components in addition to an in-plane disorder that results in the formation of magnetic domains. These results are similar to those reported by Russier[36] who studied triangular arrays of nanoparticles that had no internal structure but a random uniaxial anisotropy at 0 K, and he observed a similar domain configuration. The inter-particle disorder in arrays of maghemite nanoparticles with non-zero radial

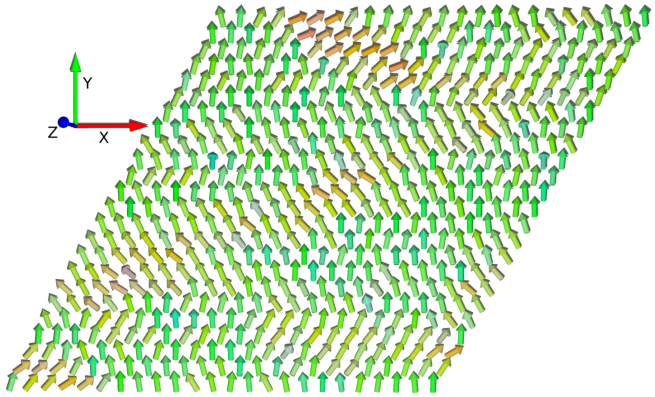

(a)

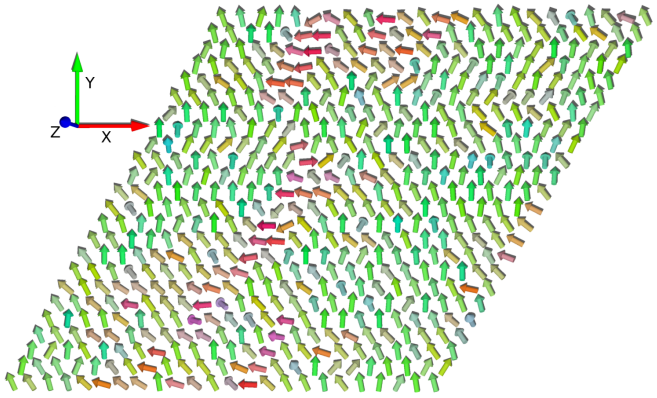

(b)

Figure 4.12: The magnetic configuration of nanoparticle triangular arrays of size L=24 with (a) K_s/k_B=5 K and (b) K_s/k_B=10 K at $T = 0$. Each arrow represents the magnetization of one nanoparticle. The color coding scheme is the same as in Fig. 4.11.

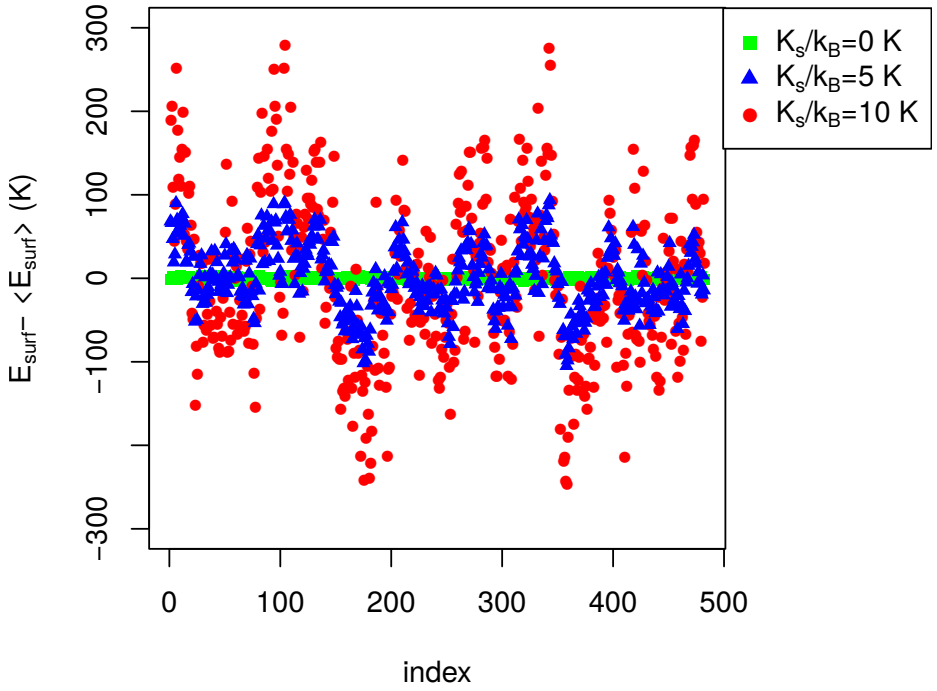

Figure 4.13: The change in the surface energy plotted as a function of the index of the direction of the core magnetic moment calculated for a single nanoparticle.

anisotropy suggests that an *effective* anisotropy arises for each nanoparticle. This is consistent with previous atomistic studies on FCC superlattice arrays of maghemite nanoparticles[34]. The nature and origin of this anisotropy is discussed in the following section.

4.4 The Effective Anisotropy

While the existence of an *effective* anisotropy in the individual nanoparticles at low temperatures that is dependent on the radial anisotropy of the surface spins would appear to account for the reduction in the order parameter η at low temperatures, the mechanism by which radial anisotropy associated with the surface spins can give rise to such a term is not obvious. To understand the origin and character of this

effective anisotropy we first note that for temperatures below which the surface spins begin to order, the magnetization of the nanoparticle core is essentially saturated and that the core Fe ions have no single site anisotropy. This implies that the effective anisotropy of the nanoparticles originates from the surface and its exchange with the fully saturated core. To illustrate this, we consider a single nanoparticle in which the magnetic moment of the core spins are assumed to be fully saturated and to be in a fixed orientation, denoted by the unit vector $\hat{\sigma}$. Using the standard Monte Carlo method, the surface spins are given random directions and then allowed to equilibrate at a given temperature followed by a calculation of the total energy and magnetization of the surface spins for each of the core magnetization directions. This calculation is performed for N values of $\hat{\sigma}$ which we denote by the set $\{\hat{\sigma}_i\} = (\hat{\sigma}_1, \hat{\sigma}_2 \ldots \hat{\sigma}_N)$ and each of the data represented by a point on a unit sphere.

The surface energy is calculated as a function of the index i for three values of $K_s/k_B = 0\,\mathrm{K}$, $5\,\mathrm{K}$ and $10\,\mathrm{K}$ at temperature of $2\,\mathrm{K}$ as shown in Fig. 4.13. For $K_s = 0$ there is no variation of the surface energy of the nanoparticle due to the rotation of the core spins. This is consistent with the result in Fig. 4.10 which shows that the dependence of the rescaled order parameter η on the reduced temperature τ agrees closely to the corresponding result for point dipoles. This is in sharp contrast to the case of finite values of K_s for which the surface energy of the nanoparticle shows a strong variation as a function of the index i. This behaviour suggests that the preferred orientation of the nanoparticle magnetization is determined by the variation in the surface energy with respect to the orientation of the core magnetization, $\hat{\sigma}_i$, and can be thought of as an effective anisotropy.

To explore the origin of this effective anisotropy, we begin by noting that one sixth of the octahedral sites are vacant and that these vacant sites are randomly distributed throughout the nanoparticle. Due to statistical variation the vacancies in the nanoparticles will not be distributed uniformly. This is clearly seen in Fig. 4.14 which show the location of the surface vacancies projected onto the surface of the

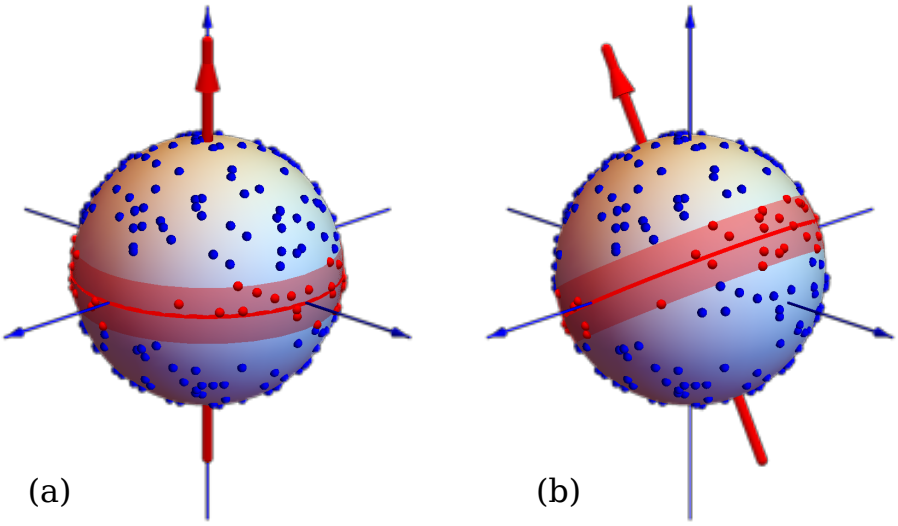

Figure 4.14: An illustration of the dependence of the equatorial vacancies on the orientation of the magnetization. The arrow indicates the direction of the core magnetization, the red line indicates the magnetic equator, the red band indicates the region in which the number of vacancies on octahedral sites are enumerated. The surface equatorial vacancies are shown as red circles, and the other vacancies as blue circles.

unit sphere for a typical nanoparticle. The equitorial vacancies are shown as red circles and the other vacancies as blue circles. Of particular interest is the number of surface vacancies located in the narrow band of octahedral sites close to the equatorial plane perpendicular to $\hat{\sigma}$. Figures 4.14 (a) and (b) show the surface vacancies that are located within a band of width $\pm 11.5^{\circ}$ for two values of $\hat{\sigma}$ indicated by the red arrows. Denoting by $n_i = n(\hat{\sigma}_i)$ the number of surface vacancies that are located within this equatorial band of octahedral states for each of the core orientations $\{\hat{\sigma}_i\}$, Fig. 4.15 plots n_i as a function of the index i together with the corresponding value for the energies $E_i = E(\hat{\sigma}_i)$ shown in Fig. 4.13. The data presented in Fig. 4.15

illustrates two important features. The first is simply the variation in n_i and the second is the fact that n_i appears to be anti-correlated to the energy E_i. Using the surface energy data for $K_s/k_B = 10\,\mathrm{K}$ we have evaluated a Pearson's correlation $\frac{\sum_i \Delta n_i \Delta E_i}{\sqrt{(\sum_i \Delta n_i^2)(\sum_i \Delta E_i^2)}} = -0.68$ where $\Delta n_i = n_i - \langle n_i \rangle$ and $\Delta E_i = E_i - \langle E_i \rangle$ respectively.

The results in Fig. 4.15 clearly show that the distribution of surface vacancies plays a critical role in determining the relationship between the surface energy and the orientation of the core spins. To obtain a qualitative understanding of what exactly determines the nature and form of this relationship, consider first the magnetic configuration of a spherical nanoparticle at $T \approx 0$ as illustrated schematically in Fig. 4.16(a). Fig. 4.16(a) shows a nanoparticle with no surface vacancies, a uniformly

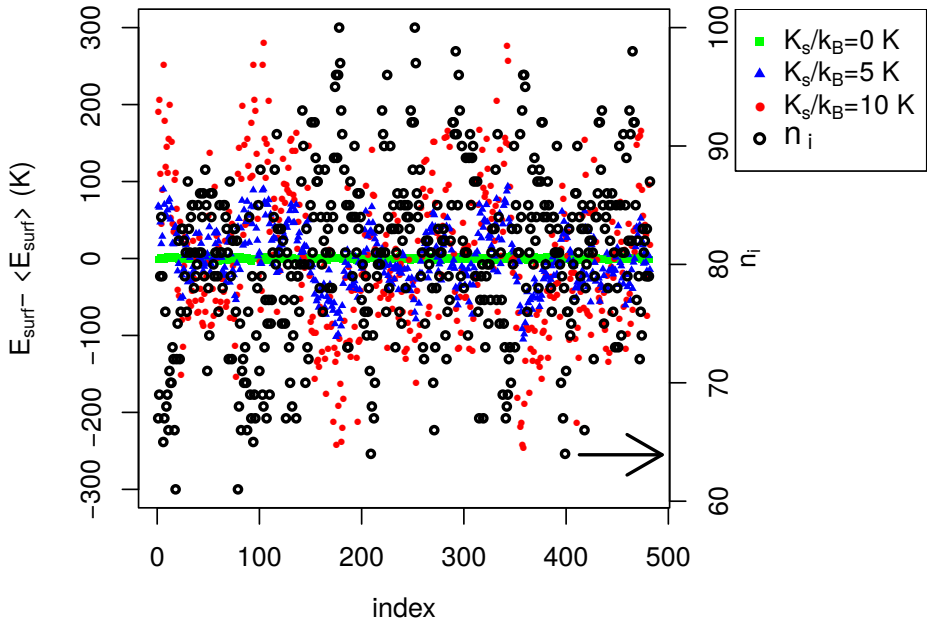

Figure 4.15: The change in the surface energy (the same data that are shown in Fig. 4.13) is plotted along with the number of vacancies on the octahedral sites in the equatorial region for each direction of the core magnetization for the same nanoparticle.

magnetized core and the surface spins directed inwards at the south pole and outwards at the north pole. While the detailed nature of the magnetic structure at the poles is determined by the minimizing super-exchange interactions and the single ion radial anisotropy at the surface for a given core orientation $\hat{\sigma}$, it is nevertheless clear from Fig. 4.16(a) that such a configuration must contain some form of domain wall located at the magnetic equator separating the two regions surrounding the magnetic poles. This has been confirmed in simulation studies[2] and is shown to be qualitatively similar to a Néel domain wall. Because the spins contained within the domain wall are highly frustrated, their energy will be higher than the surface spins located within the regions surrounding the magnetic poles.

Consider now the case shown schematically in Fig. 4.16(b) that shows the same system but with the core magnetization rotated[1]. Qualitatively we would expect that the surface spins rotate to align with the core spins and that the energy would remain approximately constant. We also note that both spin configurations contain four frustrated spins shown in red. Compare this now with the situation shown schematically in Figs. 4.16(c) and (d) in which we show essentially the same two spin configurations but with two surface vacancies indicated by the yellow dots. Whereas in the previous example each configuration has four frustrated spins, the spin configuration on the left (Fig. 4.16(c)) has four frustrated spins but the spin configuration on the right has only two frustrated spins. Since the frustrated spins (colored red) have a higher energy than the other spins (colored blue) we would expect the energy of the nanoparticle spin configuration on the right to have a lower energy than the spin configuration on the left.

While the nanoparticles we consider are somewhat more complicated than the very simplified system considered above, the basic counting argument nevertheless

[1]It is essential to note that when we refer to rotating the spin configuration, the location of the spins themselves do not change. Instead we mean that the individual spins remain fixed at their lattice sites and it is only the direction of their magnetic moment that is rotated.

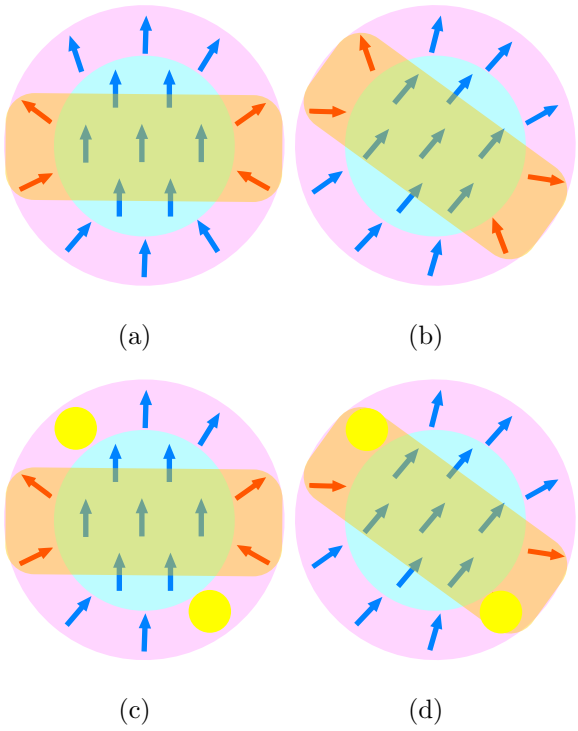

Figure 4.16: (a) Illustration of the spin configuration of one nanoparticle. The red colour represents the high energy spins. (b) The position of the magnetic equator depends on the direction of the core magnetization. (c) The yellow circles represent the random vacancies and the nanoparticle has four spins with higher energy. (d) The nanoparticle has only two higher energy spins and an effective torque exerted on the nanoparticle magnetization to minimize the overall energy.

provides a qualitative description of the correlation between the vacancy distribution and the surface energy demonstrated in Fig. 4.15 as a function of the orientation of the core magnetization. The argument may be summarized as follows: for a given orientation $\hat{\sigma}$ of the core magnetization, the surface spins may be divided into two distinct regions surrounding the magnetic poles. These regions are separated by a domain wall located on the magnetic equator. The spins in this region are highly

frustrated and have a higher energy than those located in the polar regions. As we rotate the core magnetization the surface spins respond such that the domain wall separating the two polar regions lies in the plane perpendicular to $\hat{\sigma}$ passing through the origin. As illustrated in Figs. 4.16(c) and (d) the greater the number of vacancies located within the domain wall the fewer the number of frustrated spins and the lower the energy of the spin configuration. This is akin to the pinning of domain walls by impurities and defects in standard ferromagnetic materials.

To visualize the dependence of the surface energy of a randomly selected nanoparticle on the orientation of the core magnetization, we subdivide the convex hull of the points $\{\hat{\sigma}_i\}$ on the unit sphere by constructing a Voronoi diagram[68] that consists of a set of polygons (the Voronoi regions) that enclose each of the points $\{\hat{\sigma}_i\}$. Each Voronoi region is then color coded according to the surface energy (Fig. 4.17 (a)) and the number of vacancies in the equatorial band (Fig. 4.17 (b)) when the core magnetization is in the direction of of $\{\hat{\sigma}_i\}$. Clearly, the largest numbers of equatorial vacancies coincide with the directions of the core magnetization which gives the lowest surface energy. In addition, since both the number of vacancies in the equatorial band and the energy of a single nanoparticle given by Eqn. [3.1] calculated for a specific orientation $\{\hat{\sigma}_i\}$ are invariant under the inversion ($\hat{\sigma}_i \rightarrow -\hat{\sigma}_i$), the surface energy will consist of a set of local minima comprised entirely of several distinct sets of degenerate pairs. Each pair of local energy minima may be thought of as defining an effective anisotropy axis. The set of such axes will be determined by the specific nature of the surface and will therefore be unique to each nanoparticle and will serve to characterize the effective anisotropy, alluded to earlier, for each of the individual nanoparticles.

The energy landscapes for a nanoparticle with $K_s/k_B = 10\,\mathrm{K}$ are shown in Fig. 4.18 for (a) $T = 5\,\mathrm{K}$, (b) $15\,\mathrm{K}$ and (c) $25\,\mathrm{K}$. The energy landscapes are characterized by several distinct local extrema. While the overall scale of the variation in the surface energy decreases with increasing temperature, the location of the local extrema are

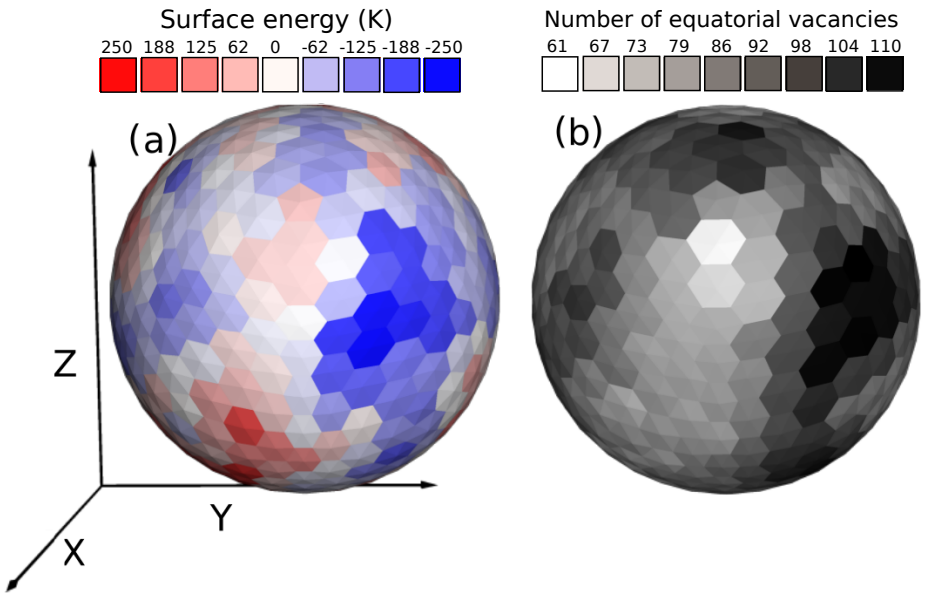

Figure 4.17: The surface energy landscape of one nanoparticle with K_s/k_B=10 K at (a) T=5 K, and (b) the number of vacancies in the equatorial band associated with each of the mesh points $\{\hat{\sigma}_i\}$.

relatively insensitive to temperature. The variation of the surface energy (and hence the effective anisotropy) decreases as the temperature approaches 25 K above which the surface spins disorder. This behaviour is consistent with the discussion presented schematically in Fig. 4.16 since the spatial distribution of the vacancies (which determines the location of the minima) is independent of temperature, whereas the degree of frustration of the surface spins located in the vicinity of the magnetic equator will decrease as the surface magnetization decreases with increasing temperature (which determines the magnitude of the variation of the surface energy). In addition, above 25 K the surface spins disorder and there is no well defined domain wall. As a consequence, the surface spin configuration has a negligible effect on the dependence of the surface energy on the orientation of the core spins. This is consistent with our results in Fig. 4.9 where the array magnetization is independent of the surface ra-

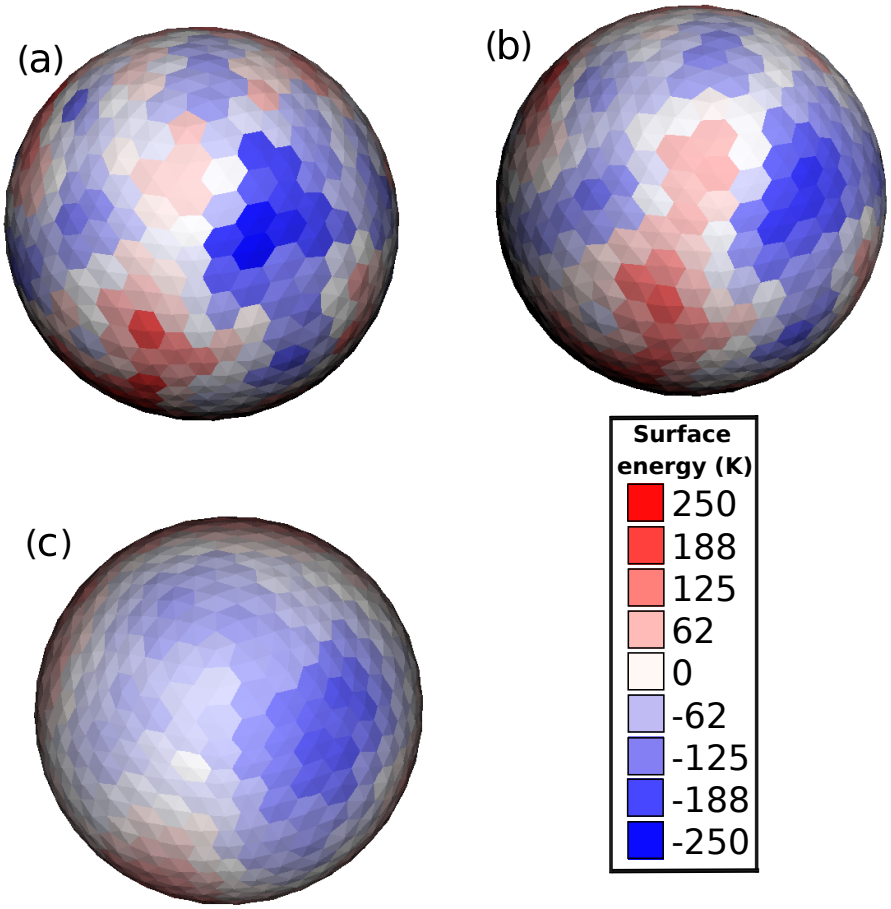

Figure 4.18: The surface energy landscape of one nanoparticle with K_s/k_B=10 K at (a) T=5 K, (b) T=15 K, and (c) T=25 K.

dial anisotropy at temperatures above 25 K. Furthermore, the increase in the surface effective anisotropy with decreasing the temperature (below which the surface spins begin to order) is consistent with experimental observations[48] of 7 nm spherical non-interacting maghemite nanoparticles where both the anisotropy and the magnetization show an exponential like increase below 30 K. Such behavior is expected to be observed in magnetic nanoparticles of materials other than maghemite as well due to crystalline defects or due to doping with non-magnetic atoms.

In the nanoparticle arrays, the magnetization of each nanoparticle approaches one of the directions that maximize the number of the equatorial vacancies at the surface to reduce the surface energy. At the same time, it tends to maintan an in-plane direction that is close to the magnetizations of the surrounding nanoparticles to minimize the energy of the ferromagnetic dipolar interactions. As a result, the array can be divided into magnetic domains where each group of neighboring nanoparticles tend to have a local magnetization that is different from other groups. With reducing the radial surface anisotropy, the ferromagnetic long range dipolar interactions become more dominant over the localized surface effective anisotropy and the size of each domain increases. As the size of the magnetic domains increases with reducing the radial anisotropy, the number of the magnetic domains in the array decreases as shown in Figs. 4.11,4.12.

4.5 Summary

The ferromagnetic ground state of a system of magnetic dipoles in a triangular array shows an energy-per-site consistent with previous studies. The energy remains the same regardless of the magnetization direction, as long as the dipoles are parallel and in-plane, leading to a degenerate ground state. When perturbations are introduced, such as thermal fluctuations or structural disorder, the system exhibits "order-from-disorder," preferring certain in-plane directions for the net magnetization. This behavior is confirmed by simulations showing a six-fold symmetry in the preferred magnetization directions.

In a triangular array of maghemite nanoparticles, the magnetization of each nanoparticle prefers specific directions influenced by the interplay between short-range interactions and the random distribution of vacancies on the surface, resulting in an effective anisotropy unique to each nanoparticle. This effective anisotropy of the individual nanoparticles is shown to increase with decreasing temperature, aligning with ex-

perimental observations of dispersed maghemite nanoparticles. The simulations also indicate that the effective anisotropy reduces array alignment, contributing to the formation of magnetic domains within the array. As radial surface anisotropy increases, ferromagnetic dipolar interactions become less dominant, leading to smaller magnetic domains.

Chapter 5

Spin waves in Triangular Array of Maghemite Nanoparticles

In this chapter, we start by exploring the spin wave excitations in a triangular lattice of simple dipoles, coupled via dipolar interctions, and compare these observations with an exact theoretical model to confirm the accuracy of our findings. Then, we examine a lattice of maghemite nanoparticles to investigate the impact of surface anisotropy on the excitations. We observe that vacancies within the nanoparticles introduce a random anisotropy, resulting in spectral gaps.

5.1 Simple Dipole Array

To understand the effect of the surface anisotropy on the dynamics of an array of nanoparticles, we study the spin waves of the array. To illustrate the formation of spin waves due to interparticle interactions, we start by studying the spin waves in an array of simple dipoles using the method that is discussed in Sec. 3.3. The dipole array has a net magnetization along the y-axis (one of the six preferred directions). Since the effective field is along the y-axis, the y-component of the spin waves corresponds to the longitudinal waves. This component represents how the magnetization vector returns to its equilibrium state along the direction of the effective magnetic

field after being disturbed. In our case, there is no external disturbance, and the longitudinal component is just the relaxation response to the thermal fluctuation when present. The propagation of precession around the y-axis (oscillation of the x- and z-components of the magnetization of the dipoles) corresponds to the transverse waves.

Fig. 5.1 shows the spectra of the longitudinal spin wave of the simple dipole array (y-component of the magnetization) for various values of the wave-vector. Each wave-vector corresponds to a given value (n_1, n_2) where $\vec{q} = n_1\vec{b_1} + n_2\vec{b_2}$, with the reciprocal lattice unit vectors defined as: $\vec{b_1} = \frac{2\pi}{a}\left(1, -\frac{1}{3}\right)$ and $\vec{b_2} = \frac{2\pi}{a}\left(0, \frac{2}{3}\right)$. For example, the top-left subfigure contains the spectra for the wave-vectors with $n_1 = 0$ and $n_2 = 0, 1, 2, ..., 23$. The spectra exhibit a single dominant peak at zero frequency, indicating that the longitudinal component primarily captures the relaxation of the magnetization to its equilibrium state along the effective field direction. The absence of any significant peaks at non-zero frequencies (any wave-vector with $n_1 \neq 0$ and $n_2 \neq 0$) suggests that the propagating longitudinal modes in the system are negligible. This behavior is consistent with the expectation that the longitudinal component represents the magnetization's response to thermal fluctuations and does not contribute to the spin wave dynamics.

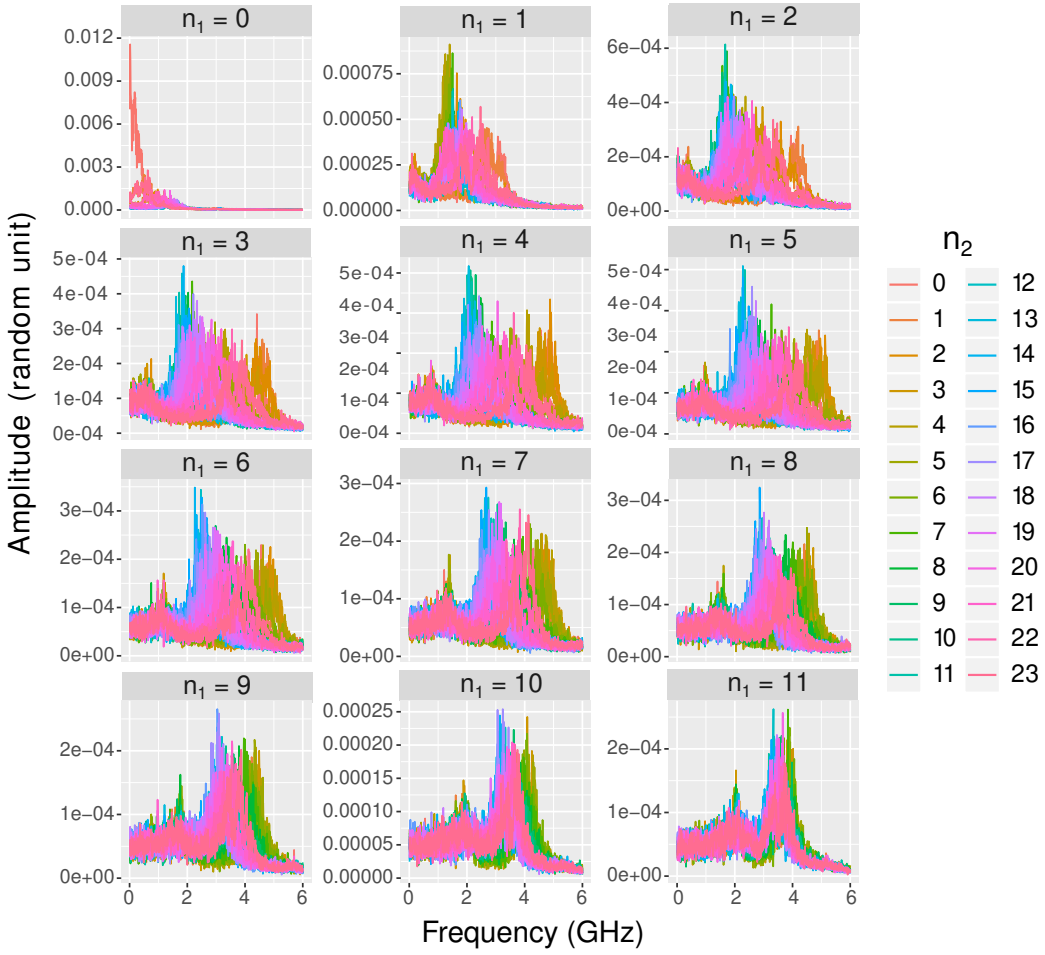

Figure 5.1: The amplitude of the longitudinal spin waves in a triangular array of simple dipoles at 1 K, as a function of the frequency, is presented for various values of the wave-vector (i.e., various values of n_1 and n_2). Note the different scales for the amplitude.

Similarly, Fig. 5.2 shows the spectra of the z-component of the magnetization. The frequencies and amplitudes of the peaks of the longitudinal spin waves vary with the wave vector, reflecting the dispersive nature of the spin waves. In contrast to the longitudinal component, the z-component spectra exhibit clear peaks at non-zero frequencies, indicating the presence of propagating spin wave modes. The amplitude

of these peaks is two orders of magnitude larger than amplitude of the longitudinal spin waves. Since the longitudinal component corresponds to the relaxation process and the system is being studied without any disturbance, the longitudinal modes shown in Fig. 5.1 have much smaller amplitude than the transverse modes in Fig. 5.2 (two orders of magnitude). This phenomenon can be comprehended by considering a single spin precessing around an effective field along the y-axis. In this scenario, there is no longitudinal component; the spin simply precesses in the x-z plane.

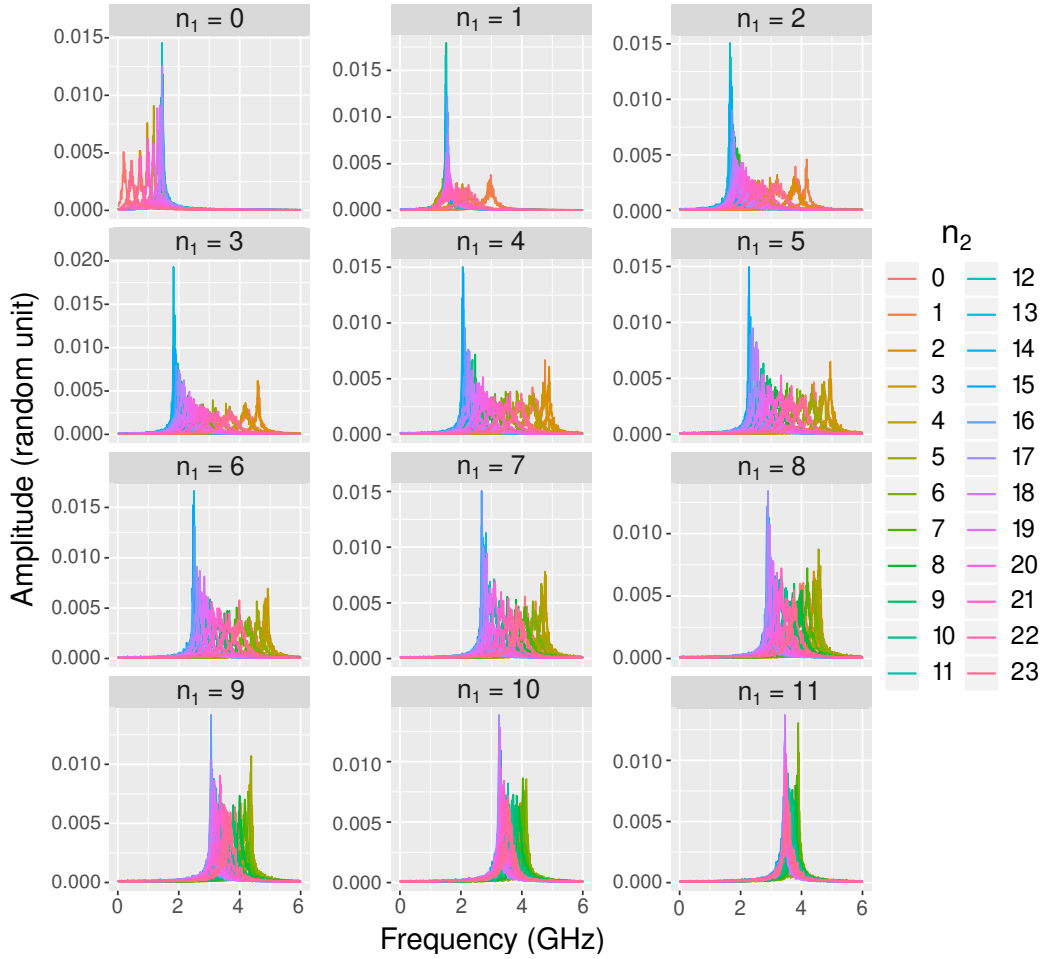

Figure 5.2: The amplitude of the z-component of the spin waves in a triangular array of simple dipoles at 1 K, as a function of frequency, for various values of the wave-vector (i.e., various values of n_1 and n_2).

Fig. 5.3 displays the spectra of the x-component of the magnetization. We note a peak with very large-amplitude for long wavelengths (i.e., $n_1 = n_2 = 0$). The case of ($n_1 = n_2 = 0$) corresponds to null wave-vector (i.e., infinite wave-length). In other words, the extra near-zero-frequency peak in the x-component corresponds to the mode of the movement of the net magnetization. The net magnetization can move in plane (with the restriction of the small in-plane six-fold anisotypy), but not out of

plane. Thus, we see this near zero-frequency peak in the spectra of the x-component, but not in the spectra of the z-component. The presence of this extra peak in the x-component spectra for long wavelengths indicates that low-energy excitations of the system can results in an in-plane movement of the net magnetization.

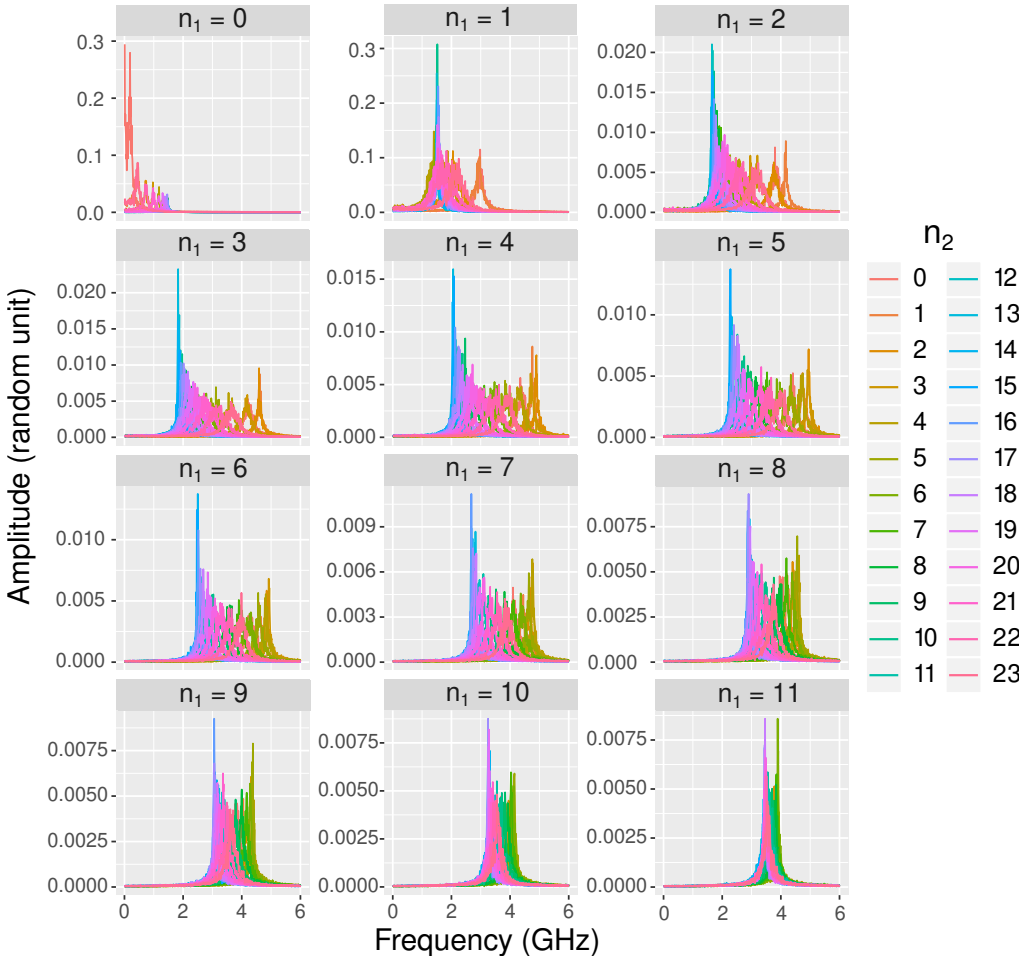

Figure 5.3: The amplitude of the x-compnent of the spin waves in a triangular array of simple dipoles at 1 K, as a function of frequency, for various values of the wave-vector (i.e., various values of n_1 and n_2).

To illustrate the differences between the x- and z-components, Fig. 5.4 displays the spectra of both components for $n_1 = 0$ and various values of n_2. It is observed that for relatively short wavelengths ($n_2 \neq 0$), both components exhibit the same peak frequency. For long wavelengths where $n_1 = n_2 = 0$, the x-component reveals an additional peak near zero frequency, attributed to the in-plane movement of net magnetization. The overlap between the two peaks for the x-component shifts the non-zero peak frequency. This shift results in a discrepancy between the x- and the z-component frequencies. To account for this discrepency, the x-component was fitted with two lorentzian functions as shown in Fig. 5.5. We note that the fitting curve match well with the spectra. After fitting, the frequency of the non-zero peak matches the frequency of the z-component. This is expected as the two components corresponds to the propagating transverse spin wave after removing the peak that corresponds to the movement of the net magnetization.

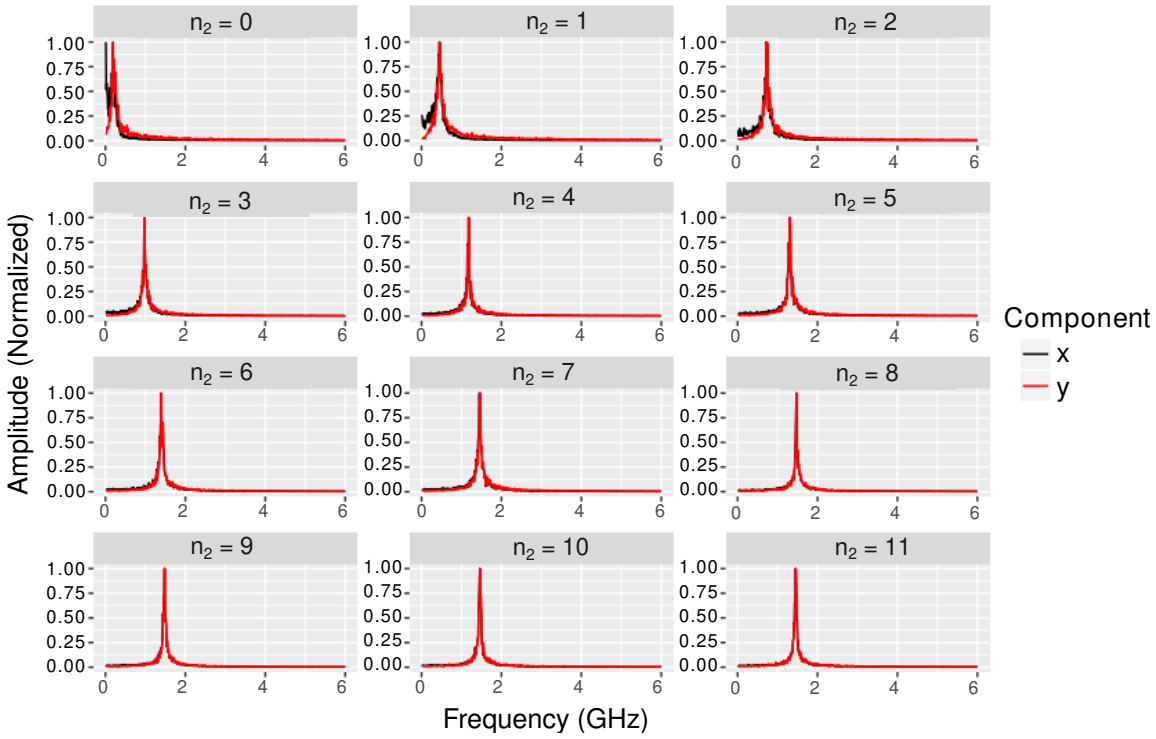

Figure 5.4: The amplitude of the x and the z-compnent of the spin waves in a triangular array of simple dipoles at 1 K, as a function of frequency, for various values of the wave-vector ($n_1 = 0$).

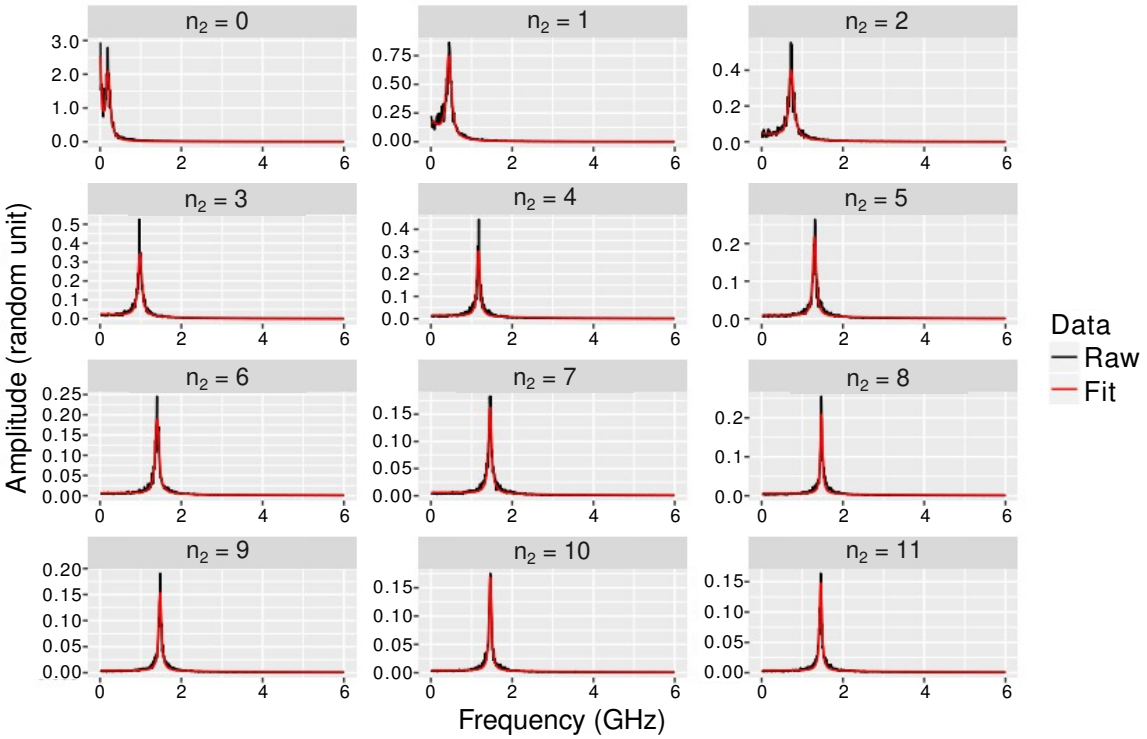

Figure 5.5: Fitting the x-component spectra of the dipole array involves using two Lorentzian functions, where one peak is positioned at zero.

Since the x-component has an extra relaxation peak due to the in-plane movement, and the frequency of the x-component matches the frequency of the z-component after removing the zero-frequency peak, we will focus on the z-component as a reference to the transverse spin wave.

We calculate the peak frequency for each value of n_1 and n_2 in Fig. 5.2 and plot it as a function of the corresponding wave-vector in Brillouin zone. For comparison, we plot the Brillouin zone for the theoretical calculations and for the nanoparticle array with $K_s = 0K$ as shown in Fig. 5.6. The difference in the direction between the subfigures is due to the fact that the magnetization of the nanoparticle array happened to be in one of the six-fold directions (other than the y-axis). Similarly, the

theoretical calculation as shown in Appendix B was carried out by assuming that the magnetization is in another direction of the six preffered directions.

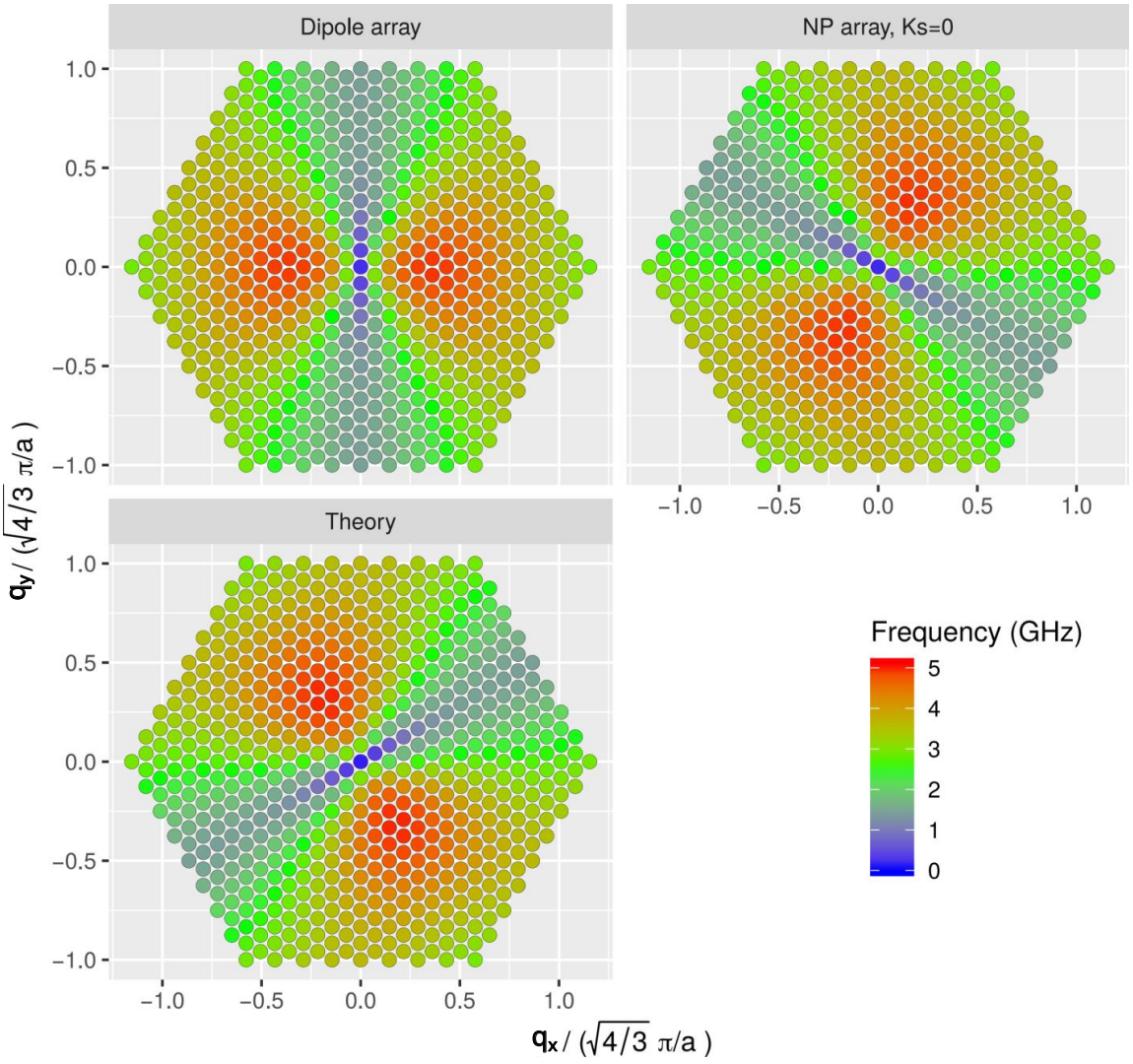

Figure 5.6: The transverse spin wave frequency as a function of the wave-vector for (a) simple dipole array, (b) nanoparticle array with $K_s = 0$K, and (c) theoretical calculation. The frequency is color coded.

We note that the spin wave frequencies along the direction of the net magnetization

are lower than the frequencies in the perpendicular direction. Along the direction of the net magnetization, the energy required to excite spin waves is generally lower due to the alignment of magnetic moments. This alignment reduces the effective magnetic field experienced by neighboring moments, facilitating the propagation of spin waves with lower energy.

Perpendicular to the magnetization direction, the magnetic moments experience stronger interactions and may encounter higher energy barriers due to magnetic anisotropy. As a result, spin waves propagating in this direction typically have higher frequencies.

To facilitate a more direct comparison, we plot the dispersion curve along the direction of the magnetization in Fig. 5.7 and along a direction perpendicular to the magnetization in Fig. 5.8. The good agreement between the spin wave dispersion of the simple dipole array, the nanoparticle array with zero anisotropy, and the theoretical calculations validates our atomistic simulation approach. It demonstrates that the dynamics of the magnetization in the nanoparticle array with zero anisotropy can be effectively captured by considering the dipolar interactions between the nanoparticles, treating them as simple dipoles. The frequency at $q = 0$, F_0, attributes to the energy gap due to the six-fold in-plane anisotropy as discussed in Appendix B.

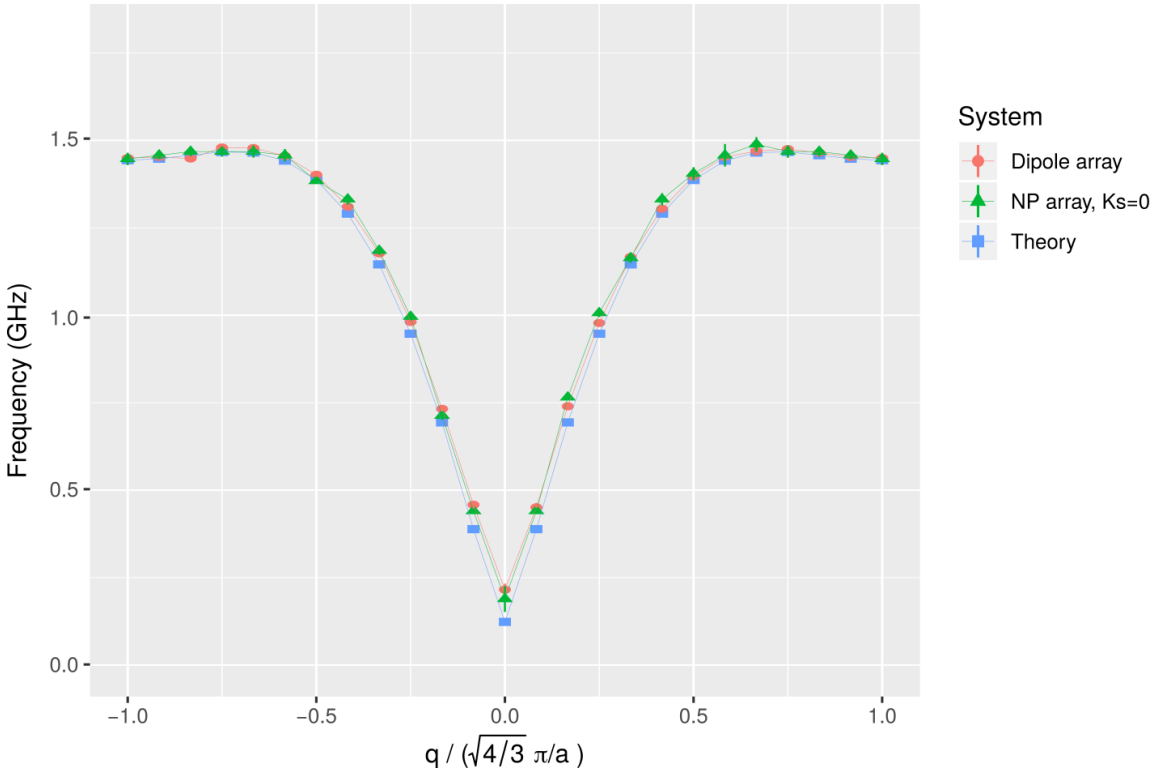

Figure 5.7: The dispersion curve of the transverse spin waves for simple dipole array, Nanoparticle array with $K_s = 0K$, and theoretical calculation in a direction that is parallel to the net magnetization.

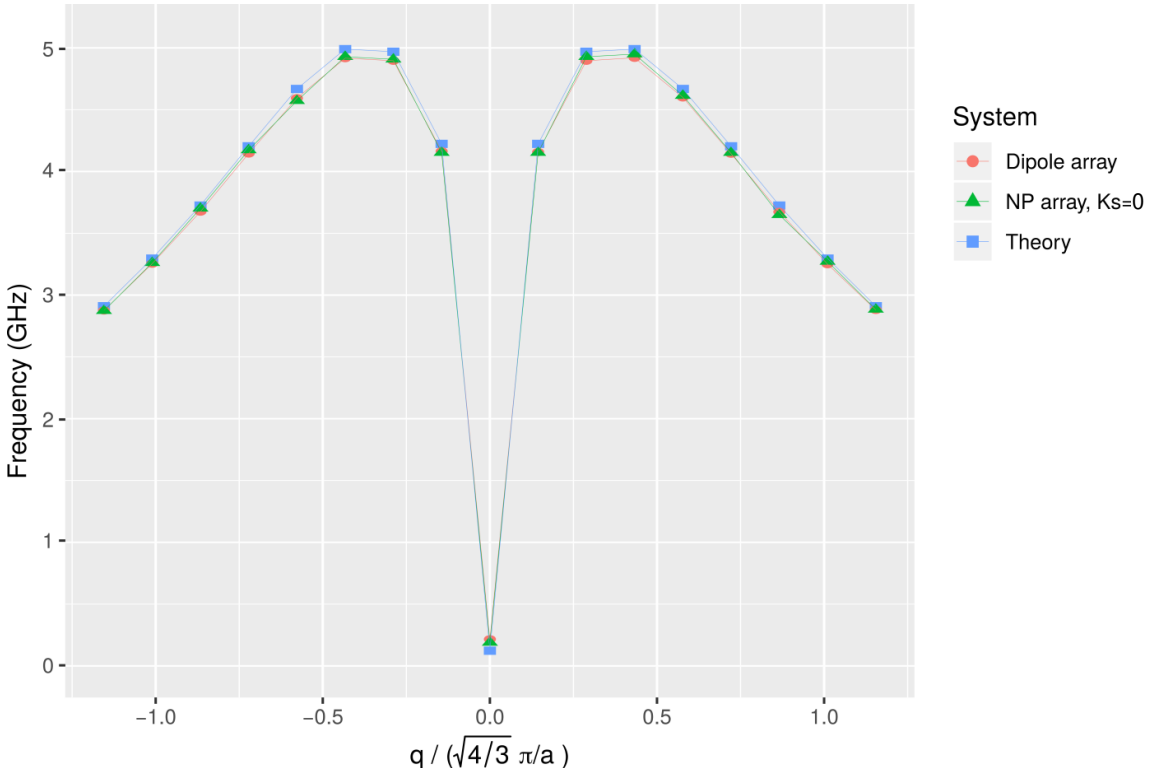

Figure 5.8: The dispersion curve of the transverse spin waves for simple dipole array, Nanoparticle array with $K_s = 0K$, and theoretical calculation in a direction that is prependicular to the net magnetization.

5.2 Maghemite Nanoparticle Array

To illustrate the effect of the surface anisotropy, we consider a nanoparticle array with $K_s = 2.5K$. Fig. 5.9 shows the spectra of the z-component of nanoparticle array with $K_s = 2.5K$ for $n_1 = 0$ and various values of n_2. The line is drawn by fitting the data using smoothing splines functions in order to obtain a more precise value of the non-zero peak freaquency. The non-zero frequency is identical for both the z- and the x-component as they are just components of the same waves. We note the presense of an additional peak at zero frequency for all wave-vectors. As we will demonstrate, the

appearance of the zero-frequency peak in the presence of surface anisotropy suggests the existence of localized modes that do not propagate through the system.

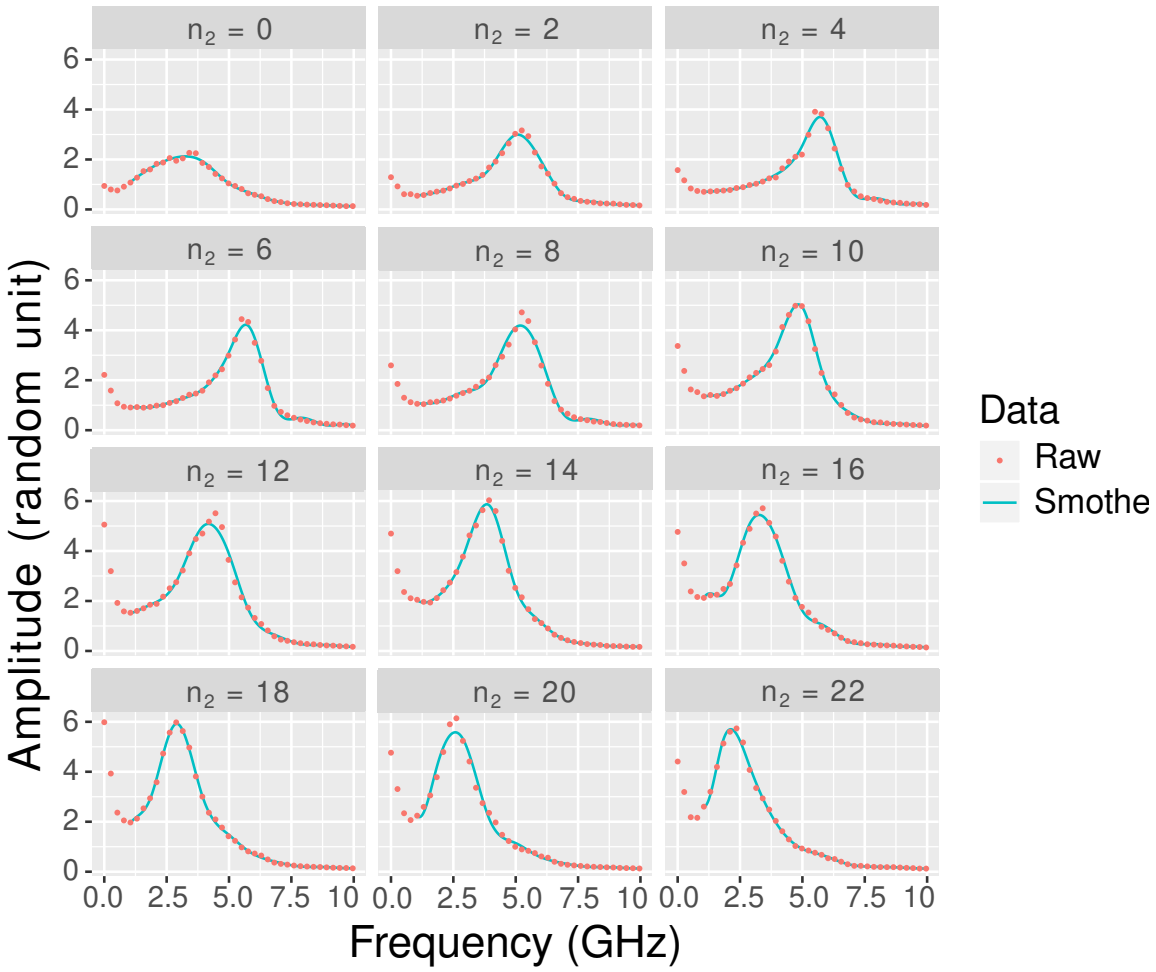

Figure 5.9: The spectra of the z-component of nanoparticle array with $K_s = 2.5K$ for $n_1 = 0$ and various values of n_2. The line is drawn by fitting the data using smoothing splines functions.

To understand the origin of the zero frequency peaks, we consider the magnetization of one nanoparticle in the array. Since the spin waves are propagating across the array, the precession of the magnetization of any nanoparticle is just a combina-

tion of all the spin waves. Thus, each nanoparticle should have non-zero amplitude for any precession frequency that corresponds to a propagating spin wave. Plotting the spectra of each nanoparticle shows two distinct groups of nanoparticles: a group where the spectra of each nanoparticle have a single non-zero peak, and another group of nanoparticles with an additional and more dominant peak at zero frequency. Fig. 5.10 shows the frequency of the largest peak for each nanoparticle vs the index of the nanoparticle. This indicates that the zero-frequency peak is due to some localized effect rather than propagating spin waves.

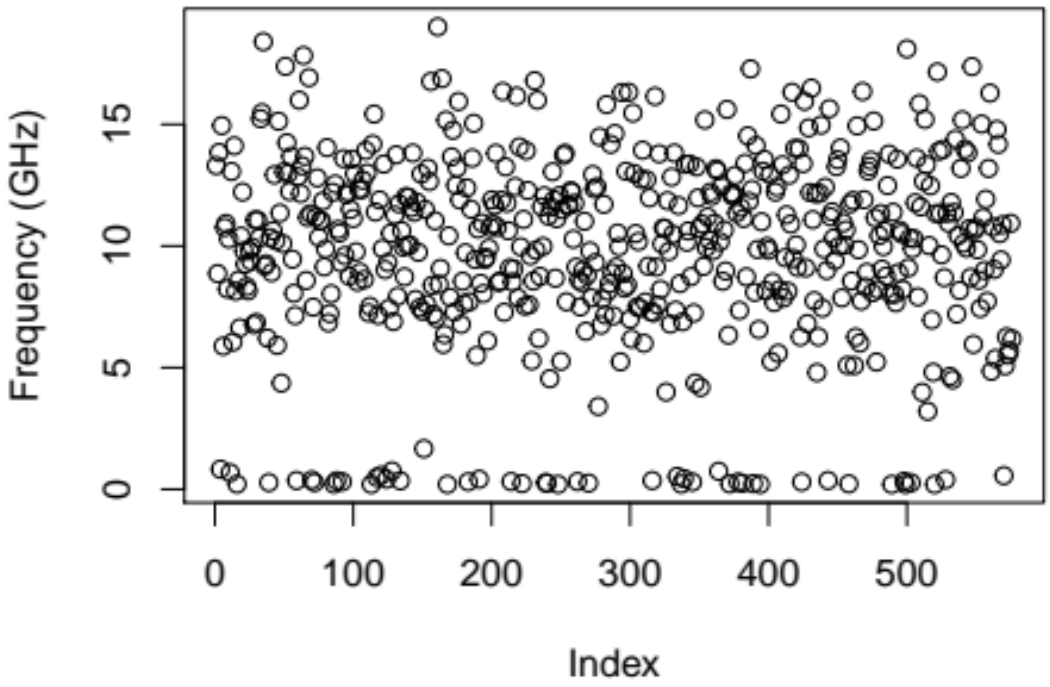

Figure 5.10: The frequency of the largest peak of each nanoparticle vs the index of the nanoparticle. Each point is for one nanoparticle.

For confirmation, we plot the magnetization of a nanoparticle with zero-frequency peak and compare it with a nanoparticle without zero-frequency peak. Fig. 5.11 shows an example of a nanoparticle of each group. The magnetization of each of the nanoparticles that have only one peak precesses around a fixed point, whereas the magnetization of each of the nanoparticles that have zero-frequency peak hops between two directions. This localized, nanoparticle-specific hopping or transitioning from one minimum to another is the reason for the zero-frequency peak. The presence of these localized modes in the nanoparticle array with surface anisotropy highlights the role of the surface effective anisotropy in modifying the magnetic dynamics at the individual nanoparticle level.

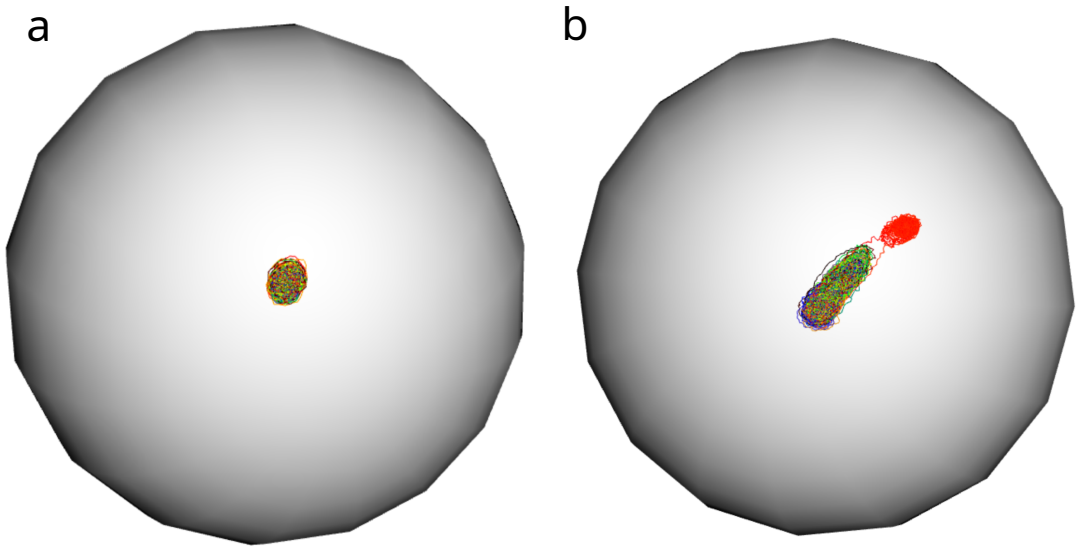

Figure 5.11: The movement of the magnetization of one nanoparticle with only one peak (a) and nanoparticle with an additional zero frequency peak (b). The change in color corresponds to the progression of time.

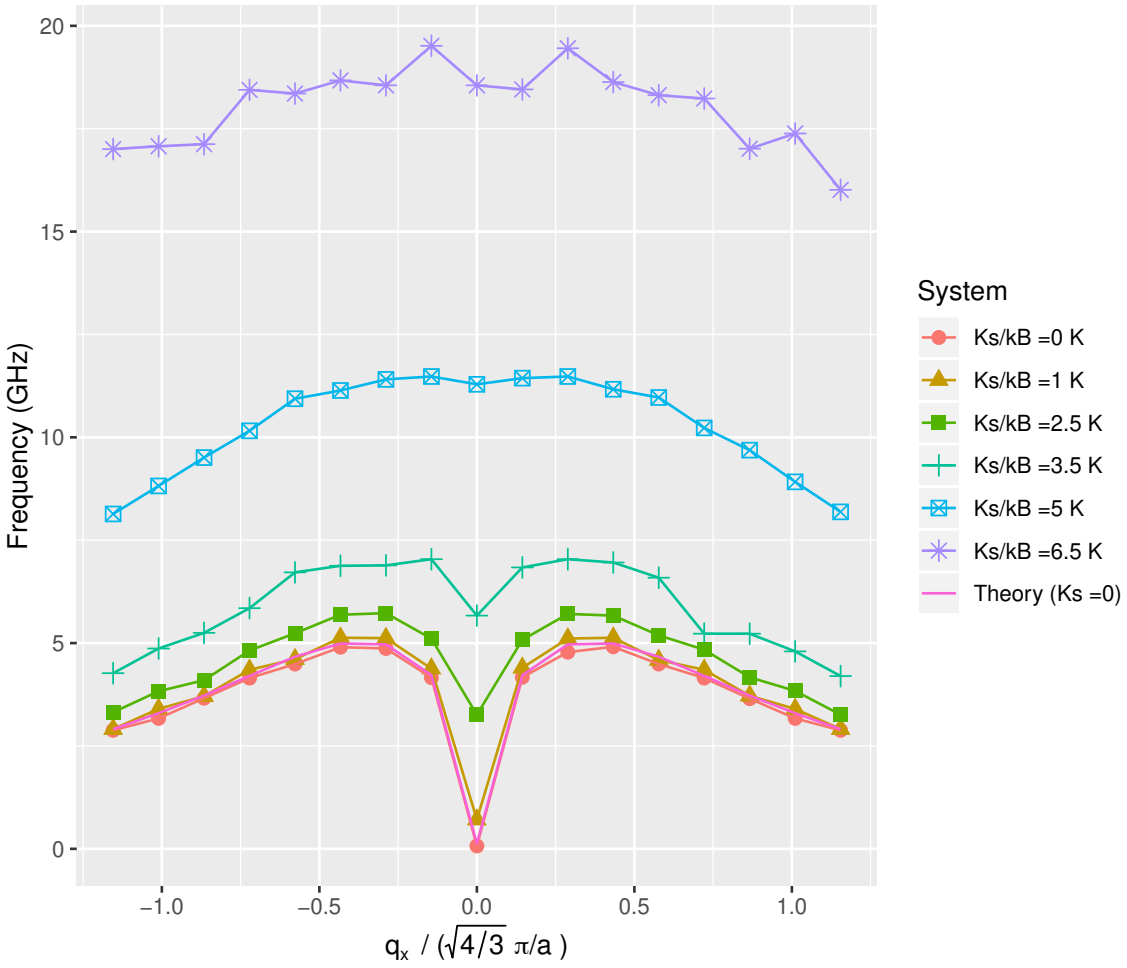

Figure 5.12: The dispersion curve in a direction that is perpendicular to the net magnetization (transverse spin waves). The data are for various values of K_s for the nanoparticle array in comparison with the theoretical calculation ($K_s = 0K$).

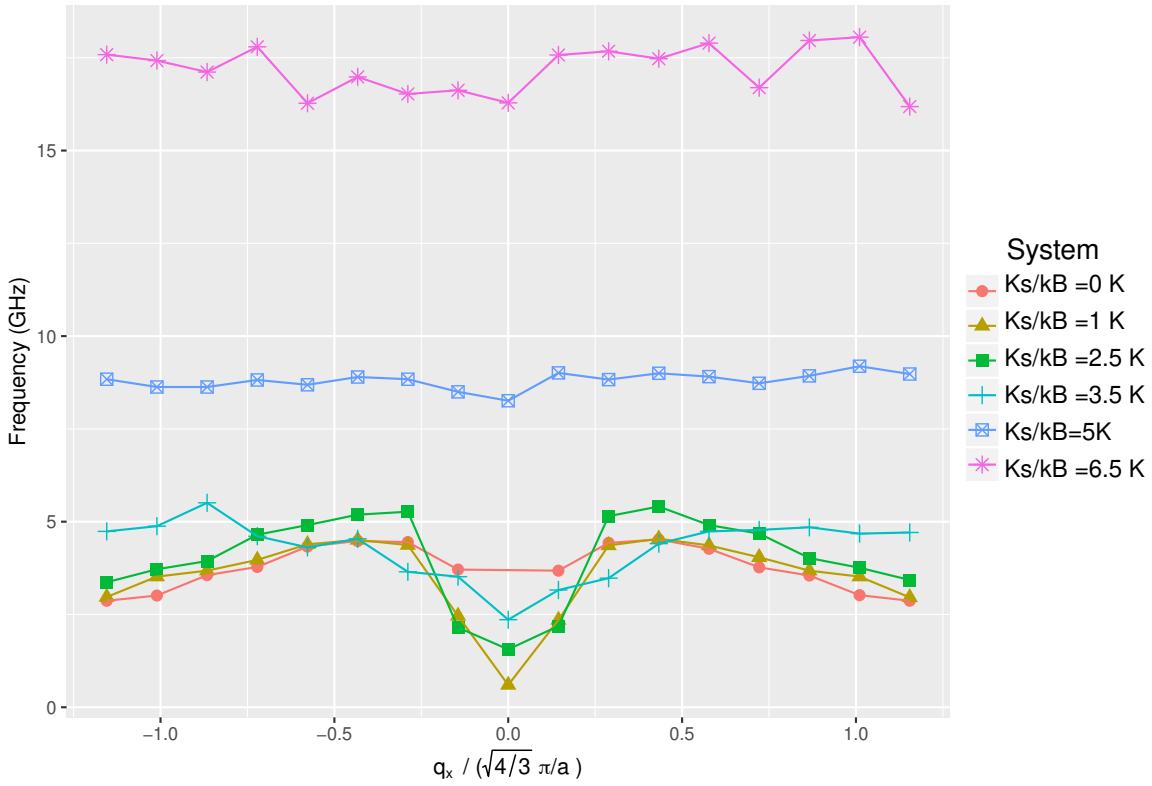

Figure 5.13: The dispersion curve in a direction that is parallel to the net magnetization (longitudinal spin waves). The data are for various values of K_s for the nanoparticle array.

To examine how the surface anisotropy affects the spin wave peaks in Fig. 5.9, we plot the dispersion curve for various values of Ks along the direction perpendicular to the net magnetization in Fig. 5.12 (transverse modes) and along the direction of the net magnetization in Fig. 5.13 (longitudinal modes). The simulation results for $K_s = 0$K are omitted since they agree with theory, as discussed earlier. We note that the spin wave frequency increases with increasing surface anisotropy. This behavior can be attributed to the additional effective field generated by the surface anisotropy, which modifies the precession frequency of the magnetization. Previous studies [69, 70, 71] show that the energy gap (and hence the frequency F) of the

localized transverse spin wave due to random anisotropy (K_s) is $F \propto K_s^2$. Since the six fold anisotropy introduces an additional energy gap that corresponds to frequency F_0, the relationship in our case becomes: $F - F_0 \propto K_s^2$

Fig. 5.14 shows the simulation results of the frequencies ($(F - F_0)^{1/2}$) at $q = 0$ vs the surface anisotropy K_s/k_B for the transverse waves. The line represents a linear fit with a slope constant $2.13 \times 10^3 \mathrm{s}^{-1/2}\mathrm{K}^{-1}$. The simulation results fit well with the relationship $F - F_0 \propto K_s^2$. This is in agreement with previous studies of transverse spin waves in systems with random anisotropy [69, 70, 71]. This confirms that the surface anisotropy is responsible for the increase of the energy gap and the localization of the spin waves.

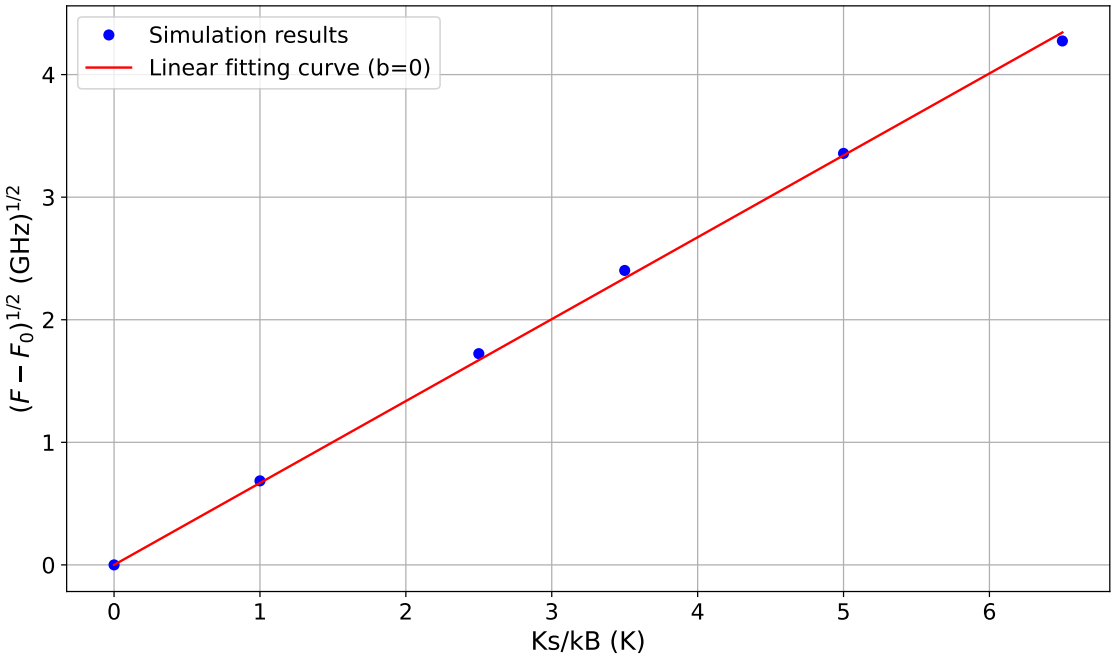

Figure 5.14: The sqaured root of the frequency $(F - F_0)^{1/2}$ of the transverse spin waves for $q = 0$ as a function of the surface anisotropy of the nanoparticle array. The line is the linear fitting.

Fig. 5.15 shows the simulation results of the frequencies $(F - F_0)$ at $q = 0$ vs the surface anisotropy K_s/k_B for the longitudinal spin waves. The line represents a linear fit for $K_s/k_B \leq 2.5K$ with a slope constant 0.62×10^6 $s^{-1}K^{-1}$. The simulation results fit well with the relationship $F - F_0 \propto K_s$ for small values of K_s. For large values of K_s, the localized spin waves couples the longitudinal spin waves with the more dominant transverse spin waves. For small values of K_s, the linearity between F and K_s is in agreement with previous studies of longitudinal spin waves in systems with random anisotropy [70, 71, 72].

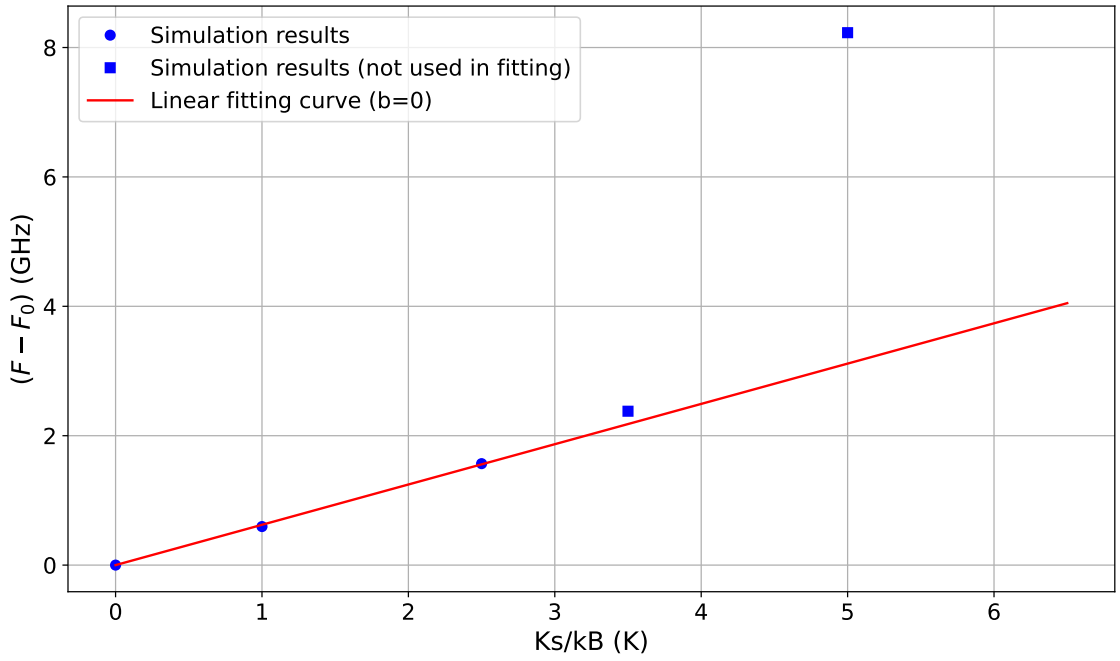

Figure 5.15: The frequency $(F - F_0)$ of the longitudinal spin waves for $q = 0$ as a function of the surface anisotropy of the nanoparticle array. The line is a linear fit to the circular shape points.

Chapter 6

Conclusion

In this thesis, we utilized atomistic spin dynamics simulations to explore the magnetic properties and dynamics of maghemite nanoparticle assemblies, which are influenced by both inter-particle and intra-particle interactions. Our investigation particularly delved into the effects of surface anisotropy, vacancies in maghemite nanoparticles, and the interactions arising from intra-particle dipoles. Through the development of a multiscale hierarchal model capable of accurately capturing the intricate interplay between intra-particle and inter-particle interactions, we have contributed novel insights into the fundamental physics governing the behavior of these systems.

Our simulations of individual maghemite nanoparticles revealed that the surface anisotropy and the vacancies play a crucial role in determining their magnetic properties. We found that competetion between the surface anisotropy and the exchange or super-exchange interactions leads to a reduction in the magnetization of the nanoparticles, particularly at low temperatures. The presence of vacancies, which modify the local magnetic interactions, leads to a more complex magnetic structure with an inhomogeneous effective anisotropy that is unique to each nanoparticle. Our results provide a deeper understanding of the experimental observations of reduced magnetization in maghemite nanoparticles and highlight the importance of considering the surface and the vacancies effects in maghemite nanoparticles.

Moving beyond individual nanoparticles, we investigated the collective magnetic behavior of maghemite nanoparticle assemblies arranged in a triangular array. To understand the nature of the dipolar interactions in an assembly of nanoparticles, we start by studying the dipole interactions of a triangular array of simple dipoles with periodic boundary conditions. Our simulations reveal that such array orders ferromagneticly in plane. Further more, there is a six-fold in-plane anisotropy due to the order from disorder effect. These findings are consistent with previous theoretical studies.

Arrays of maghemite nanoparticles with no anisotropy show identical behavior to the array of simple dipoles after normalizing the nanoparticle magnetization to take into account the dependence of the nanoparticle magnetization on temperature. In the presence of the surface anisotropy, each nanoparticle experiences an effective anisotropy that is unique to each nanoparticle. Since the effective anisotropy increases with reducing the temperature, the intra-particle order of the magnetization decreases below the surface order temperature. At 0 K temperature, we note that the out-of plane component increases with increasing the surface anisotropy. This can be understood by considering that the surface effective anisotropy is unique and randomly oriented for each nanoparticle. The competition between the intra-particle dipole interaction and the surface effective anisotropy leads to the formation of magnetic domains in the array of nanoparticles. The size of the domains decreases with increasing the surface anisotropy.

Our analysis of the spin wave spectra in simple dipole arrays has revealed the presence of transverse spin wave modes, characterized by the precession of the magnetization in the plane perpendicular to the effective field. On the other hand, the longitudinal component captures the relaxation of the magnetization to its equilibrium state and does not contribute significantly to the propagating spin wave modes. The comparison of the spin wave dispersion relations of the simple dipole arrays with theoretical calculations has validated our atomistic simulation approach and con-

firmed the effectiveness of dipolar interactions in describing the spin wave dynamics. Extending our study to maghemite nanoparticle arrays with zero surface anisotropy, we have found that the spin wave spectra and dispersion relations closely resemble those of the simple dipole arrays.

The introduction of surface anisotropy in the maghemite nanoparticle arrays has revealed the emergence of new dynamic phenomena. In particular, we have observed the presence of localized modes, manifested as zero-frequency peaks in the spin wave spectra. These localized modes arise from the hopping of the magnetization between different energy minima at the individual nanoparticle level, driven by the interplay between the surface anisotropy and the dipolar interactions. The coexistence of localized modes and propagating spin waves in the presence of surface anisotropy underscores the rich dynamic behavior of these systems and the potential for tailoring their magnetic excitations through the control of anisotropy.

Our results highlight the importance of considering the atomic-scale structure and interactions in the modeling and simulation of magnetic nanoparticle systems. While micromagnetic simulations have been widely used to study the behavior of these systems, our work demonstrates that atomistic simulations are essential for capturing the complex interplay between intra-particle and inter-particle interactions, particularly in the presence of surface effects and defects. This highlights the need for the development of multiscale modeling approaches that can bridge the gap between atomistic and micro magnetic simulations, enabling the study of larger-scale systems while retaining the accuracy of atomistic models.

It is worth considering extending our work to study the distribution of the NPs that contribute to the localized waves. We expect these NPs to be correlated with the domain walls in the triangular array. Furthermore, studying NP arrays with open boundary conditions will allow for better comparison with experiments. Our approach can also be utilized to study other array structures, such as square lattices where the dipole interactions are antiferromagnetic, or to study 3D arrays such as FCC. FCC

is a stacked layer of triangular arrays; hence, we expect FCC arrays to have similar characteristics to triangular arrays.

The insights gained from our atomistic simulations can be used to guide the experimental synthesis and characterization of magnetic nanoparticle assemblies. By providing a deeper understanding of the relationship between the atomic-scale structure and the macroscopic properties of these systems, our work can inform the design of new synthesis strategies and characterization techniques that enable the precise control and manipulation of their magnetic behavior.

Looking ahead, there are several promising avenues for future research that build upon the findings of this thesis. One important direction is the extension of our atomistic model to other types of magnetic nanoparticles, such as ferrites and alloys, to explore the role of composition and crystal structure on their magnetic properties and dynamics. Another exciting area of research is the investigation of the effects of external stimuli on the behavior of magnetic nanoparticle assemblies. This could lead to the development of novel stimuli-responsive materials with tunable magnetic properties.

Finally, the integration of magnetic nanoparticle assemblies into functional devices represents an exciting area of future research. By exploiting the unique properties of these systems, such as their high surface-to-volume ratio, tunable magnetic anisotropy, and collective behavior, it may be possible to develop novel devices with enhanced performance and functionality.

Bibliography

[1] Mathias Getzlaff. *Broken Symmetry*. Springer Berlin Heidelberg, Berlin, Heidelberg, 2008.

[2] Bassel Alkadour, J. I. Mercer, J. P. Whitehead, J. van Lierop, and B. W. Southern. Surface vacancy mediated pinning of the magnetization in $\gamma-Fe_2O_3$ nanoparticles: A micromagnetic simulation study. *Phys. Rev. B*, 93:140411, Apr 2016.

[3] Quentin A Pankhurst, J Connolly, S K Jones, and J Dobson. Applications of magnetic nanoparticles in biomedicine. *Journal of Physics D: Applied Physics*, 36(13):R167–R181, 2003.

[4] An-Hui Lu, E Lorena Salabas, and Ferdi Schüth. Magnetic nanoparticles: synthesis, protection, functionalization, and application. *Angewandte Chemie International Edition*, 46(8):1222–1244, 2007.

[5] Ajay Kumar Gupta and Mona Gupta. Synthesis and surface engineering of iron oxide nanoparticles for biomedical applications. *Biomaterials*, 26(18):3995–4021, 2005.

[6] R H Kodama. Magnetic nanoparticles. *Journal of Magnetism and Magnetic Materials*, 200(1-3):359–372, 1999.

[7] Pedro Tartaj, Maria del Puerto Morales, Sabino Veintemillas-Verdaguer, Teresita

Gonz'alez-Carre no, and Carlos J Serna. The preparation of magnetic nanoparticles for applications in biomedicine. *Journal of Physics D: Applied Physics*, 36(13):R182, 2003.

[8] Sophie Laurent, Delphine Forge, Marc Port, Alain Roch, Caroline Robic, Luce Vander Elst, and Robert N Muller. Magnetic iron oxide nanoparticles: synthesis, stabilization, vectorization, physicochemical characterizations, and biological applications. *Chemical reviews*, 108(6):2064–2110, 2008.

[9] Luisa H. A. Silva, Jaqueline R. da Silva, Guilherme A. Ferreira, Renata C. Silva, Emilia C. D. Lima, Ricardo B. Azevedo, and Daniela M. Oliveira. Labeling mesenchymal cells with dmsa-coated gold and iron oxide nanoparticles: assessment of biocompatibility and potential applications. *Journal of Nanobiotechnology*, 14:59, 2016.

[10] Seong-Joo Lee and Soonchil Lee. The spin structure of maghemite investigated by 57fe nmr. *New Journal of Physics*, 8(6):98, jun 2006.

[11] Elisabeth Tronc, Corinne Chanéac, and Jean-Pierre Jolivet. Vacancy ordering and magnetic properties of γ-fe$_2$o$_3$ nanoparticles. *Journal of Magnetism and Magnetic Materials*, 183(1-2):L1–L5, 1998.

[12] E Tronc, A Ezzir, R Cherkaoui, C Chan'eac, M Nogu'es, H Kachkachi, D Fiorani, AM Testa, JM Gren'eche, and JP Jolivet. Surface-related properties of γ-fe$_2$o$_3$ nanoparticles. *Journal of Magnetism and Magnetic Materials*, 221(1-2):63–79, 2000.

[13] M.P. Morales, S. Veintemillas-Verdaguer, M.I. Montero, C.J. Serna, A. Roig, L. Casas, B. Mart'ınez, and F. Sandiumenge. Surface and internal spin canting in γ-fe$_2$o$_3$ nanoparticles. *Chemistry of Materials*, 11(11):3058–3064, 1999.

[14] J. M. D. Coey. *Magnetism and Magnetic Materials*. Cambridge University Press, 2010.

[15] Ralph Skomski. *Simple Models of Magnetism*. Oxford Graduate Texts. Oxford University Press, USA, 2008.

[16] A. P. Guimarães. *Principles of Nanomagnetism*. Springer-Verlag Berlin Heidelberg, 2009.

[17] D. Kechrakos and K. N. Trohidou. Magnetic properties of dipolar interacting single-domain particles. *Physical Review B*, 58(18):12169, 1998.

[18] V. V. Kruglyak, S. O. Demokritov, and D. Grundler. Magnonics. *Journal of Physics D: Applied Physics*, 43(26):264001, 2010.

[19] Roman Verba, Gennadiy Melkov, Vasil Tiberkevich, and Andrei Slavin. Collective spin-wave excitations in a two-dimensional array of coupled magnetic nanodots. *Phys. Rev. B*, 85:014427, Jan 2012.

[20] P. A. Fleury, S. P. S. Porto, L. E. Cheesman, and H. J. Guggenheim. Light scattering from spin waves in fef2 and mnf2. *Physical Review Letters*, 17(2):84–87, 1966.

[21] D.S. Schmool and M. Schmalzl. Ferromagnetic resonance in magnetic nanoparticle assemblies. *Journal of Non-Crystalline Solids*, 353(8):738–742, 2007. Non-Crystalline Solids 8.

[22] M. Varón, M. Beleggia, T. Kasama, R. J. Harrison, R. E. Dunin-Borkowski, V. F. Puntes, and C. Frandsen. Dipolar magnetism in ordered and disordered low-dimensional nanoparticle assemblies. *Scientific Reports*, 3(1):1234, 2013.

[23] Frederik Laust Durhuus, Lau Halkier Wandall, Mathias Hoeg Boisen, Mathias Kure, Marco Beleggia, and Cathrine Frandsen. Simulated clustering dynamics of colloidal magnetic nanoparticles. *Nanoscale*, 13:1970–1981, 2021.

[24] Louis Néel. Properties of ferromagnetic ferrites; ferrimagnetism and antiferromagnetism. *Annales de Physique*, 12(3):137–198, 1948.

[25] J. M. D. Coey. *Magnetism and magnetic materials*. Cambridge University Press, Cambridge, 2010.

[26] H. A. Kramers. L'interaction entre les atomes magnétogènes dans un cristal paramagnétique. *Physica*, 1(1-6):182–192, 1934.

[27] P. W. Anderson. Antiferromagnetism. theory of superexchange interaction. *Phys. Rev.*, 79:350–356, Jul 1950.

[28] P. W. Anderson. New approach to the theory of superexchange interactions. *Phys. Rev.*, 115:2–13, Jul 1959.

[29] John B. Goodenough. Theory of the role of covalence in the perovskite-type manganites $[\mathrm{La}, m(\mathrm{II})]\mathrm{Mno}_3$. *Phys. Rev.*, 100:564–573, Oct 1955.

[30] Junjiro Kanamori. Superexchange interaction and symmetry properties of electron orbitals. *Journal of Physics and Chemistry of Solids*, 10(2):87 – 98, 1959.

[31] F.J.A. den Broeder, W. Hoving, and P.J.H. Bloemen. Magnetic anisotropy of multilayers. *Journal of Magnetism and Magnetic Materials*, 93:562 – 570, 1991.

[32] M T Johnson, P J H Bloemen, F J A den Broeder, and J J de Vries. Magnetic anisotropy in metallic multilayers. *Reports on Progress in Physics*, 59:1409 – 1458, 1996.

[33] E. C. Stoner and E. P. Wohlfarth. A Mechanism of Magnetic Hysteresis in Heterogeneous Alloys. *Philosophical Transactions of the Royal Society of London. Series A, Mathematical and Physical Sciences*, 240(826):599–642, 1948.

[34] Bassel Alkadour, J. I. Mercer, J. P. Whitehead, B. W. Southern, and J. van Lierop. Dipolar ferromagnetism in three-dimensional superlattices of nanoparticles. *Phys. Rev. B*, 95:214407, Jun 2017.

[35] J. M. Luttinger and L. Tisza. Theory of dipole interaction in crystals. *Phys. Rev.*, 70:954–964, Dec 1946.

[36] V. Russier. Calculated magnetic properties of two-dimensional arrays of nanoparticles at vanishing temperature. *Journal of Applied Physics*, 89(2):1287–1294, 2001.

[37] Yusuke Tomita. Monte carlo study of two-dimensional heisenberg dipolar lattices. *Journal of the Physical Society of Japan*, 78(11):114004, 2009.

[38] A. B. MacIsaac, J. P. Whitehead, K. De'Bell, and P. H. Poole. Phase diagram for a magnetic thin film with dipolar interactions and magnetic surface anisotropy. *Phys. Rev. Lett.*, 77:739–742, Jul 1996.

[39] K. De'Bell, A. B. MacIsaac, I. N. Booth, and J. P. Whitehead. Dipolar-induced planar anisotropy in ultrathin magnetic films. *Phys. Rev. B*, 55:15108–15118, Jun 1997.

[40] Pierre Weiss. L'hypothèse du champ moléculaire et la propriété ferromagnétique, 1907. PhD Thesis, University of Zurich.

[41] Werner Heisenberg. Zur theorie des ferromagnetismus. *Zeitschrift für Physik*, 49(9-10):619–636, 1928.

[42] Lev Landau and Evgeny Lifshitz. *Statistical Physics Part 1: Volume 5*. Pergamon Press, 1935.

[43] T. L. Gilbert. A phenomenological theory of damping in ferromagnetic materials. *IEEE Transactions on Magnetics*, 40(6):3443–3449, Nov 2004.

[44] W F Brown. Thermal fluctuations of a single-domain particle. *Physical Review*, 130(5):1677–1686, June 1963.

[45] R. H. Kodama and A. E. Berkowitz. Atomic-scale magnetic modeling of oxide nanoparticles. *Phys. Rev. B*, 59:6321–6336, Mar 1999.

[46] R. H. Kodama, A. E. Berkowitz, E. J. McNiff, Jr., and S. Foner. Surface spin disorder in nife$_2O_4$ nanoparticles. *Phys. Rev. Lett.*, 77:394–397, Jul 1996.

[47] E Tronc, A Ezzir, R Cherkaoui, C Chanéac, M Noguès, H Kachkachi, D Fiorani, A.M Testa, J.M Grenèche, and J.P Jolivet. Surface-related properties of gamma-fe2o3 nanoparticles. *Journal of Magnetism and Magnetic Materials*, 221(1):63 – 79, 2000.

[48] T N Shendruk, R D Desautels, B W Southern, and J van Lierop. The effect of surface spin disorder on the magnetism of $\gamma-$ Fe_2O_3 nanoparticle dispersions. *Nanotechnology*, 18(45):455704, 2007.

[49] A. A. Sidorov, V. P. Suetin, and V. G. Pokazan'ev. *IAdernyi rezonans v tverdo-faznykh soedineniiakh d-metallov (UNTs AN SSSR, Sverdlovsk)*, pages 21 – 31, 1984.

[50] A. A. Sidorov, V. P. Suetin, V. G. Pokazaniev, and B. V. Karpenko. Determination of effective indirect exchange interaction integrals in ferrimagnets. *physica status solidi (b)*, 129(2):625–629, 1985.

[51] G.M. da Costa, E. De Grave, and R.E. Vandenberghe. Mössbauer studies of magnetite and al-substituted maghemites. *Hyperfine Interactions*, 117(1):207–243, Dec 1998.

[52] G. T. Rado and V. J. Folen. Determination of molecular field coefficients in ferrimagnets. *Journal of Applied Physics*, 31:62–68, 1960.

[53] J. I. Mercer and J. P. Whitehead. Scripted micromagnetics environment. Presentation at Magnetic North II, St. Johns, NL, 2011.

[54] K. De'Bell, A. B. MacIsaac, and J. P. Whitehead. Dipolar effects in magnetic thin films and quasi-two-dimensional systems. *Rev. Mod. Phys.*, 72:225–257, 2000.

[55] Y. Yafet, J. Kwo, and E. M. Gyorgy. Dipole-dipole interactions and two-dimensional magnetism. *Phys. Rev. B*, 33:6519–6522, May 1986.

[56] Y. Yafet, J. Kwo, and E. M. Gyorgy. Erratum: Dipole-dipole interactions and two-dimensional magnetism. *Phys. Rev. B*, 34:3475–3475, Sep 1986.

[57] R. F. L. Evans, U. Atxitia, and R. W. Chantrell. Quantitative simulation of temperature-dependent magnetization dynamics and equilibrium properties of elemental ferromagnets. *Phys. Rev. B*, 91:144425, Apr 2015.

[58] G. Palma and D. Zambrano. Cluster-algorithm renormalization-group study of universal fluctuations in the two-dimensional ising model. *Phys. Rev. E*, 78:061134, Dec 2008.

[59] E. Rastelli, S. Regina, and A. Tassi. Planar triangular model with long-range interactions. *Phys. Rev. B*, 66:054431, Aug 2002.

[60] V M Bedanov. Long-range order in a classical two-dimensional dipole system. *Journal of Physics: Condensed Matter*, 4(1):75, 1992.

[61] E. Rastelli, S. Regina, and A. Tassi. Short-range exchange and long-range dipole interactions in a triangular planar model. *Phys. Rev. B*, 67:094429, Mar 2003.

[62] Dominik Schildknecht, Michael Schütt, Laura J. Heyderman, and Peter M. Derlet. Continuous ground-state degeneracy of classical dipoles on regular lattices. *arXiv e-prints*, Mar 2019.

[63] J. Villain, R. Bidaux, J.-P. Carton, and R. Conte. Order as an effect of disorder. *J. Phys. (France)*, 41:1263–1272, 1980.

[64] Sona Prakash and Christopher L. Henley. Ordering due to disorder in dipolar magnets on two-dimensional lattices. *Phys. Rev. B*, 42:6574–6589, Oct 1990.

[65] S M Patchedjiev, J P Whitehead, and K De'Bell. Effects of dilution on the magnetic ordering of a two-dimensional lattice of dipolar magnets. *Journal of Physics: Condensed Matter*, 17(13):2137, 2005.

[66] S M Patchedjiev, J P Whitehead, and K De'Bell. The role of the exchange and dipolar interactions in the determination of the magnetic ordering of a two-dimensional lattice with random vacancies. *Journal of Physics: Condensed Matter*, 19(19):196207, 2007.

[67] B. Alkadour, B. W. Southern, J. P. Whitehead, and J. van Lierop. Triangular array of iron oxide nanoparticles: Simulation study of intraparticle and interparticle magnetism. *Phys. Rev. B*, 100:094416, Sep 2019.

[68] Lili Ju, Todd Ringler, and Max Gunzburger. *Voronoi Tessellations and Their Application to Climate and Global Modeling*, pages 313–342. Springer Berlin Heidelberg, Berlin, Heidelberg, 2011.

[69] V. S. Amaral, B. Barbara, J. B. Sousa, and J. Filippi. Spin Wave Localization in Random Anisotropy Systems: Amorphous (DyxGd1-x)Ni. *Europhysics Letters*, 22(2):111–115, 1993.

[70] W. M. Saslow. Ferromagnets with weak random anisotropy. *Phys. Rev. B*, 35:3454–3460, Mar 1987.

[71] R. A. Serota. Spin-wave localization in ferromagnets with weak random-axes anisotropy. *Phys. Rev. B*, 37:9901–9903, Jun 1988.

[72] W. M. Saslow. Ferromagnets with random anisotropy: Longitudinal spin resonance and movable anisotropy. *Phys. Rev. Lett.*, 50:1320–1323, Apr 1983.

Appendix A

Order From Disorder

Consider the Hamiltonian describing dipole-dipole interactions between Heisenberg classical spins located at the sites of a two dimensional triangular lattice

$$H = \frac{g}{2} \sum_{i=1} \sum_{j=1} \sum_{\alpha=1}^{3} \sum_{\beta=1}^{3} D_{ij}^{\alpha\beta} S_i^{\alpha} S_j^{\beta}, \tag{A.1}$$

where g is the dipole interaction strength and

$$D_{ij}^{\alpha\beta} = \frac{\delta_{\alpha\beta}}{|\vec{r}_i - \vec{r}_j|^3} - \frac{3(\vec{r}_i - \vec{r}_j)^{\alpha} \cdot (\vec{r}_i - \vec{r}_j)^{\beta}}{|\vec{r}_i - \vec{r}_j|^5}$$

is a traceless symmetric tensor. The $\vec{r}_i$ are the lattice positions for each site i in units of the nearest neighbour spacing a and S_i^{α} are the cartesian components of the unit spin at each site.

The basis vectors of the lattice are $\vec{a}_1 = (1, 0, 0)$ and $\vec{a}_2 = (1/2, \sqrt{3}/2, 0)$ in units of a and the positions of the lattice sites are given by $\vec{r} = n_1\vec{a}_1 + n_2\vec{a}_2$ where n_1 and n_2 are integers. We divide the lattice up into cells of size $L \times L$ where both n_1 and n_2 are restricted to the range $1..L$. The infinite system is generated using periodic boundary conditions and the Hamiltonian can be rewritten as

$$H = \frac{g}{2} \sum_{i=1}^{N} \sum_{j=1}^{N} \sum_{\alpha=1}^{3} \sum_{\beta=1}^{3} \Gamma_{ij}^{\alpha\beta} S_i^{\alpha} S_j^{\beta} \tag{A.2}$$

where the sums over i and j are restricted to the cell. The interaction tensor $\Gamma_{ij}^{\alpha\beta}$ is calculated using the Ewald method. Since the triangular lattice only has x and y coordinates, $\Gamma_{ij}^{xz} = \Gamma_{ij}^{yz} = 0$. However, $\Gamma_{ij}^{zz} = -\Gamma_{ij}^{xx} - \Gamma_{ij}^{yy}$ since it is a traceless tensor.

Consider a ferromagnetic ground state with the spins in the plane of the lattice

$$S_i^x = \cos(\phi_0) \; ; S_i^y = \sin(\phi_0) \; ; S_i^z = 0 \; \forall_i \tag{A.3}$$

where ϕ_0 is the direction of the spins in the plane with respect to the x-axis.

Hence the expectation value of H in the ground state is

$$\begin{aligned} < H > &= \frac{g}{2} \sum_i \sum_j [\Gamma_{ij}^{xx} \cos(\phi_0)^2 + \Gamma_{ij}^{yy} \sin(\phi_0)^2 \\ &\qquad + \Gamma_{ij}^{xy} \sin(2\phi_0)] \end{aligned} \tag{A.4}$$

$$\begin{aligned} &= \frac{gN}{2} [\tilde{\Gamma}^{xx}(\vec{k}=0) \cos(\phi_0)^2 + \tilde{\Gamma}^{yy}(\vec{k}=0) \sin(\phi_0)^2 \\ &\qquad + \tilde{\Gamma}^{xy}(\vec{k}=0) \sin(2\phi_0)] \end{aligned} \tag{A.5}$$

where

$$\tilde{\Gamma}^{\alpha\beta}(\vec{k}) = \sum_{j=1}^{N} \Gamma_{ij}^{\alpha\beta} e^{i\vec{k}.(\vec{r}_i - \vec{r}_j)} \tag{A.6}$$

is the Fourier transform of the interaction tensor.

At $\vec{k} = 0$,

$$\tilde{\Gamma}^{\alpha\beta}(\vec{k}) = \delta_{\alpha\beta} 2\epsilon_0 \tag{A.7}$$

for $\alpha, \beta = x, y.$ with

$$\tilde{\Gamma}^{zz}(\vec{k}) = -\tilde{\Gamma}^{xx}(\vec{k}) - \tilde{\Gamma}^{yy}(\vec{k})$$

and

$$\epsilon_0 = -2.758$$

Hence $< H >= Ng\epsilon_0 = -Ng2.758$ is independent of ϕ_0.

Now consider expanding H in terms of harmonic deviations from the ground state $\delta_i = (\phi_i - \phi_0), \gamma_i = (\theta_i - \pi/2)$.

$$\begin{aligned} H &= Ng\epsilon_0 + \frac{g}{2}\sum_{i,j}[\delta_i A_{ij}\delta_j + \gamma_i B_{ij}\gamma_j \\ &\qquad +\gamma_i C_{ij}\delta_j + \delta_i C'_{ij}\gamma_j] \end{aligned} \tag{A.8}$$

where

$$\begin{aligned} A_{ii} &= -\cos(\phi_0)^2\tilde{\Gamma}^{xx}(0) - \sin(\phi_0)^2\tilde{\Gamma}^{yy}(0) - \sin(2\phi_0)\tilde{\Gamma}^{xy}(0) \\ A_{ij} &= \sin(\phi_0)^2\Gamma^{xx}_{ij} + \cos(\phi_0)^2\Gamma^{yy}_{ij} - \sin(2\phi_0)\Gamma^{xy}_{ij} \\ B_{ii} &= A_{ii} \\ B_{ij} &= \Gamma^{zz}_{ij} \\ C_{ij} &= 0 \\ C'_{ij} &= 0 \end{aligned} \tag{A.9}$$

Thus

$$H = Ng\epsilon_0 + \frac{g}{2}\sum_{\vec{k}}[A(\vec{k})\delta_{\vec{k}}\delta_{-\vec{k}} + B(\vec{k})\gamma_{\vec{k}}\gamma_{-\vec{k}}] \tag{A.10}$$

where

$$\begin{aligned} A(\vec{k}) =& -2\epsilon_0 + \sin(\phi_0)^2\tilde{\Gamma}^{xx}(\vec{k}) + \cos(\phi_0)^2\tilde{\Gamma}^{yy}(\vec{k}) \\ & - \sin(2\phi_0)\tilde{\Gamma}^{xy}(\vec{k}) \\ B(\vec{k}) =& -2\epsilon_0 + \tilde{\Gamma}^{zz}(\vec{k}) \end{aligned} \tag{A.11}$$

The partition function is

$$\begin{aligned} Z &= \prod_{\vec{k}}\int_{-\infty}^{\infty}\delta_{\vec{k}}\int_{-\infty}^{\infty}\gamma_{\vec{k}}e^{-N\epsilon_0 g/T - \frac{g}{2T}A(\vec{k})\delta_{\vec{k}}\delta_{-\vec{k}} - \frac{g}{2T}B(\vec{k})\gamma_{\vec{k}}\gamma_{-\vec{k}}} \\ &= e^{-N\epsilon_0 g/T}\prod_{\vec{k}}\left[\frac{2\pi T}{gA(\vec{k})}\right]^{1/2}\left[\frac{2\pi T}{gB(\vec{k})}\right]^{1/2} \end{aligned} \tag{A.12}$$

The free energy is given by

$$F = -T \ln Z = N\epsilon_0 g + T/2 \sum_{\vec{k}} \ln A(\vec{k}) \tag{A.13}$$

plus terms independent of ϕ_0. We only need terms dependent on ϕ_0 to study order from disorder.

Hence

$$dF/(gN) = (T/g)\frac{1}{2L^2} \sum_{\vec{k}} \ln A(\vec{k}) \tag{A.14}$$

or simply

$$df/\tau = \frac{1}{2L^2} \sum_{\vec{k}} \ln A(\vec{k}) \tag{A.15}$$

where $\tau = T/g$ is the reduced temperature and df is the change in free energy per site in units of g.

A numerical calculation for different L yields the form

$$df/\tau = a + b\cos(6\phi_0) \tag{A.16}$$

with the values of a and b listed in Table B1.

The minima lie at $30^0, 90^0, 150^0, 210^0, 270^0, 330^0$ and the barrier height is $2b$.

Table B1: The values of a and b for various array sizes.

L	a	b
8	0.7463	0.0172
16	0.7435	0.0121
32	0.7417	0.0103
64	0.7409	0.0097
128	0.7407	0.0095

Appendix B

Spin Waves

B.1 Spin Waves Frequency

The spin wave excitations can be obtained in a variety of ways. We can use the classical torque equation in either cartesian or spherical coordinates or the quantum mechanical commutation relations for the spin operators. All approaches yield the same result. Perhaps the simplest approach is to use the torque equation in spherical coordinates r, θ, ϕ. The magnetization is in a direction $\hat{r}$ and given by $\vec{M} = M_s\hat{r}$. Since $\hat{r}$ is not a constant vector, it is easy to show that $\frac{d\hat{r}}{dt} = \hat{\theta}\dot{\theta} + \sin\theta\hat{\phi}\dot{\phi}$. The torque equation

$$\frac{d\vec{M}}{dt} = M_s\frac{d\hat{r}}{dt} = -\gamma_G\mu_0\vec{M}\times\vec{H}_{eff} \tag{B.1}$$

where γ_G is the gyromagnetic ratio becomes

$$\begin{aligned} \dot{\theta} &= \gamma_G\mu_0 H_\phi \\ \sin\theta\dot{\phi} &= -\gamma_G\mu_0 H_\theta \end{aligned} \tag{B.2}$$

where $\vec{H}_{eff} = H_r\hat{r} + H_\theta\hat{\theta} + H_\phi\hat{\phi}$ in spherical coordinates and $\vec{H}_{eff} = -\frac{1}{\mu_0}\vec{\nabla}E_{tot}$. and thus $H_\theta = -\frac{\partial E_tot}{\partial\theta}/(\mu_0 M_s)$ and $H_\phi = -\frac{\partial E_tot}{\partial\phi}/(\mu_0 M_s\sin\theta)$.

We can apply these equations to the Hamiltonian in equation (8) above where δ_i is $\phi_i - \phi_0$ and γ_i is $\theta_i - \pi/2$.

Hence from equation (17) we have

$$\begin{aligned} \dot{\gamma}_i &= -\frac{\gamma_G g}{M_s \sin\theta_0} \sum_j A_{ij}\delta_j \\ \sin\theta_0 \dot{\delta}_i &= \frac{\gamma_G g}{M_s} \sum_j B_{ij}\gamma_j \end{aligned} \tag{B.3}$$

and Fourier transforming we arrive at

$$\begin{aligned} \dot{\gamma}(\vec{k}) &= -\frac{\gamma_G g}{M_s \sin\theta_0} A(\vec{k})\delta(\vec{k}) \\ \sin\theta_0 \dot{\delta}(\vec{k}) &= \frac{\gamma_G g}{M_s} B(\vec{k})\gamma(\vec{k}) \end{aligned} \tag{B.4}$$

where $\theta_0 = \pi/2$. Assuming that $\gamma(\vec{k}), \delta(\vec{k}) \sim e^{i\omega(\vec{k})t}$ we find

$$\omega(\vec{k}) = \frac{\gamma_G g}{M_s}\sqrt{A(\vec{k})B(\vec{k})} \tag{B.5}$$

where $A(\vec{k})$ and $B(\vec{k})$ were given previously. The ratio of the out of plane anplitude to that of the in plane amplitude perpendicular to the magnetization direction is given by

$$\sqrt{A(\vec{k})/B(\vec{k})} \tag{B.6}$$

.

The above formula for $\omega(\vec{k})$ is a generalization of that derived by Smit and Belgers for the FMR frequency.

B.2 Effect of order from disorder on spin waves

At zero wave-vector the spin wave frequency above vanishes. However, the order from disorder contributed an extra term in the free energy per site of the form $dF =$

$Tb\sum_i cos(6\phi_i)$. Such a term would contribute to the expansion in equation (8) as follows

$Tb\sum_i cos(6(\phi_0+\delta_i) \sim (T/g)(g/2)b\sum_i cos(6\phi_0)(2-36(\delta_i)^2)$ and A has an extra term $36\tau b$ since $\cos(6\phi_0) = -1$.

Hence the spin wave frequency becomes

$$\omega(\vec{k}) = \frac{\gamma_G g}{M_s}\sqrt{(A(\vec{k})+36\tau b)B(\vec{k})} \tag{B.7}$$

and there is a gap in the spin waves at $\vec{k}=0$ with

$$\omega(\vec{k}=0) = \frac{\gamma_G g}{M_s}\sqrt{(36\tau b)(-6\epsilon_0)} \tag{B.8}$$

.

The behaviour of the array magnetization at low T can be calculated from

$$M(\tau)/M(0) = 1 - \frac{1}{L^2}\sum_{\vec{k}} \frac{A(\vec{k})+B(\vec{k})}{2\omega(\vec{k})}\frac{1}{e^{\omega(\vec{k})/\tau}-1} \tag{B.9}$$

which in the classical limit becomes

$$M(\tau)/M(0) = 1 - \frac{\tau}{L^2}\sum_{\vec{k}} \frac{A(\vec{k})+B(\vec{k})}{2A(\vec{k})B(\vec{k})} \tag{B.10}$$

A numerical calculation yields $M(\tau)/M(0) = 1 - 0.406\tau$ for $L = 128$. For $L = 24$ the coefficient of τ is 0.36.

B.3 Numbers

The prefactor in equation (23) is

$$\frac{\gamma_G g}{M_s} = \frac{2\mu_B}{\hbar}\frac{\mu_0\mu_B^2}{4\pi a^3}(M_s/\mu_B) \tag{B.11}$$

where $M_s = \mu_B$ and $a = 1$ for simple dipoles but $M_s = 2\frac{5}{2}\frac{N}{4}\mu_B$ and $a = 7.5nm$ for nanoparticles with $N/4 = 2052$. I find that $\frac{\gamma_G g}{M_s} = 3.962\times 10^9$ rads/sec for the nanoparticles.

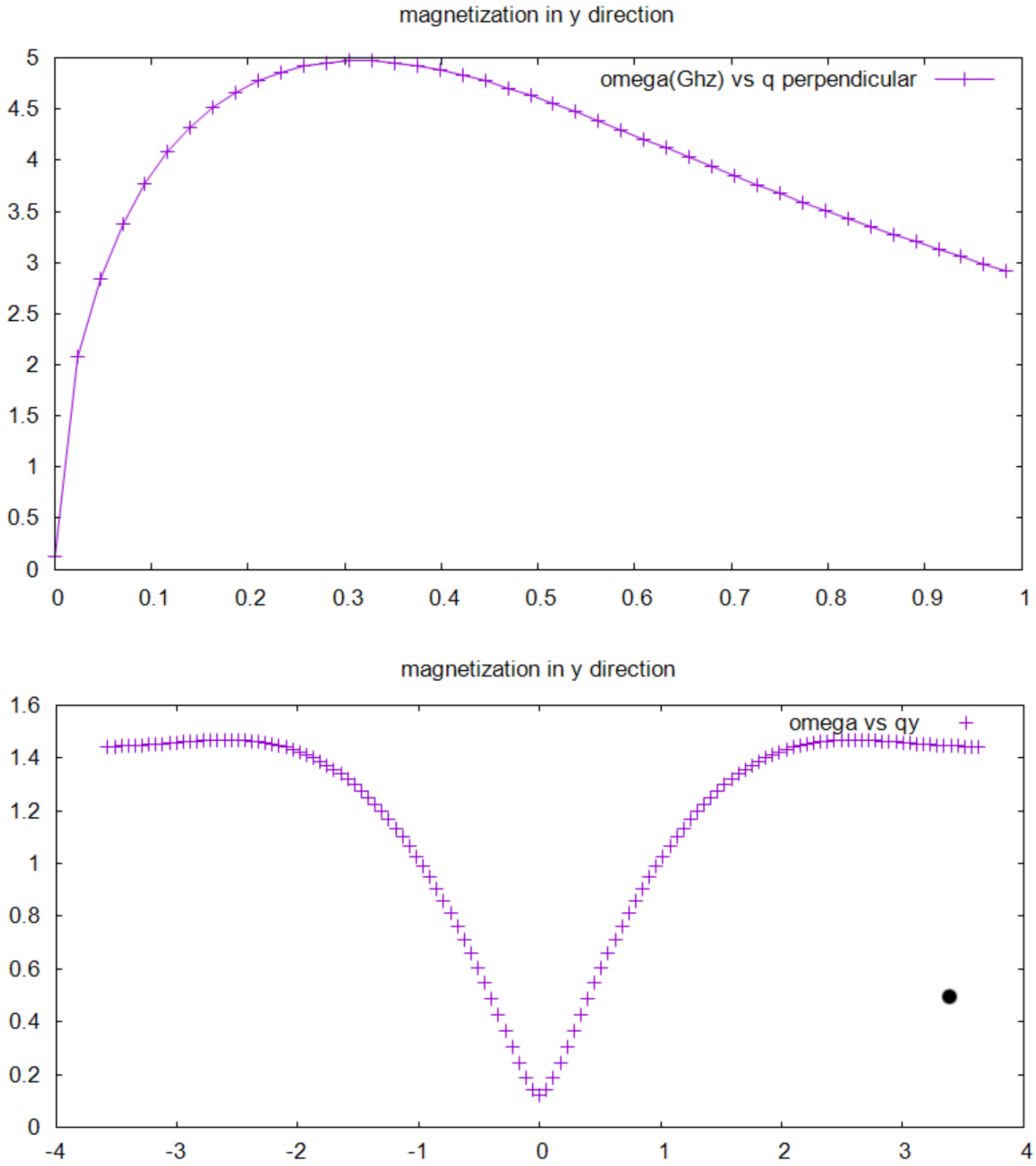

Figure B.1: Spin wave frequency vs wavevector for the triangular array of magnetic dipoles at $\tau = .0064$ $(T = 1K)$

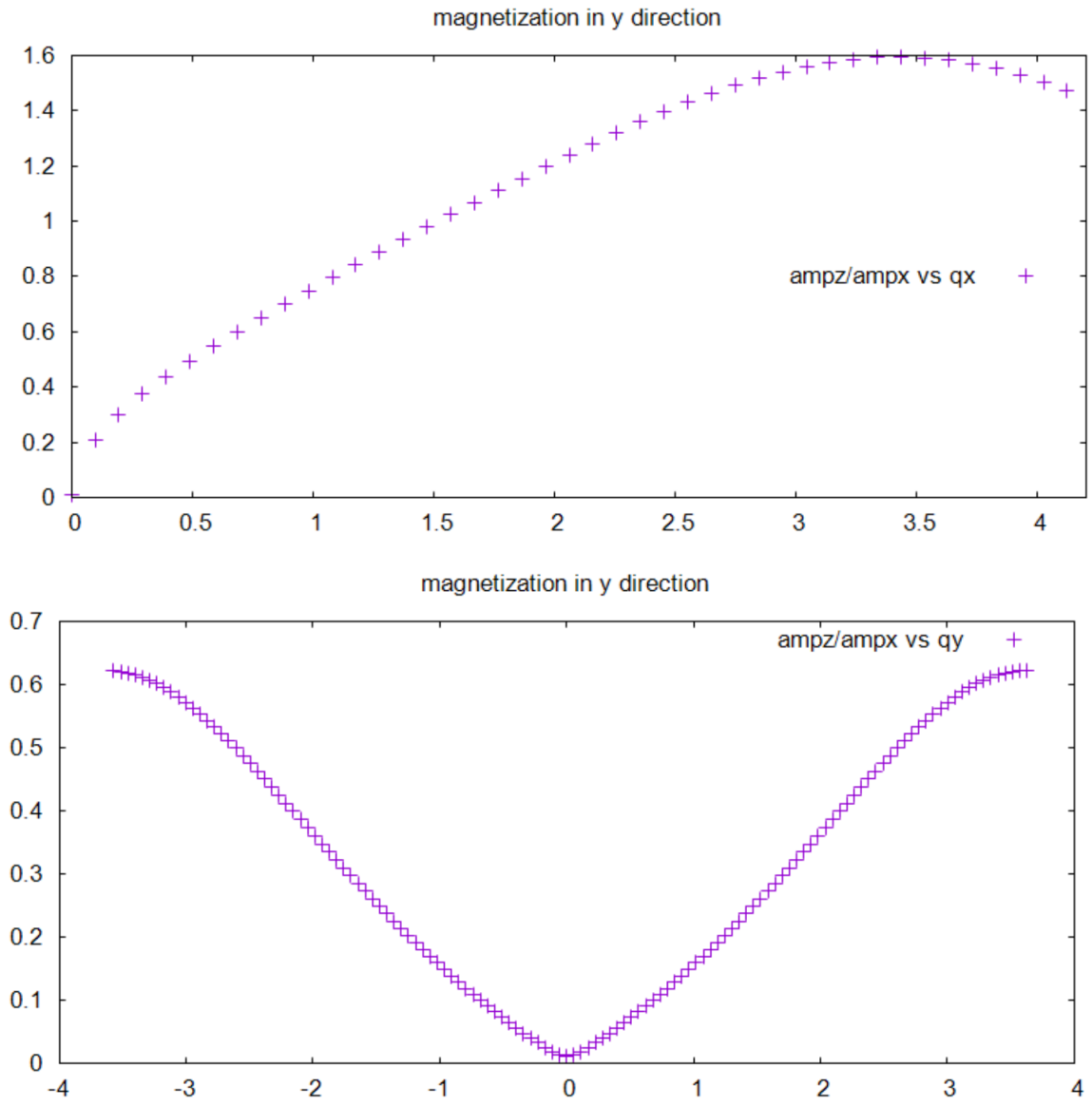

Figure B.2: Out of plane amplitude divided by in plane amplitude for the triangular array of magnetic dipoles as a function of wavevector at $\tau = .0064$ ($T = 1K$).

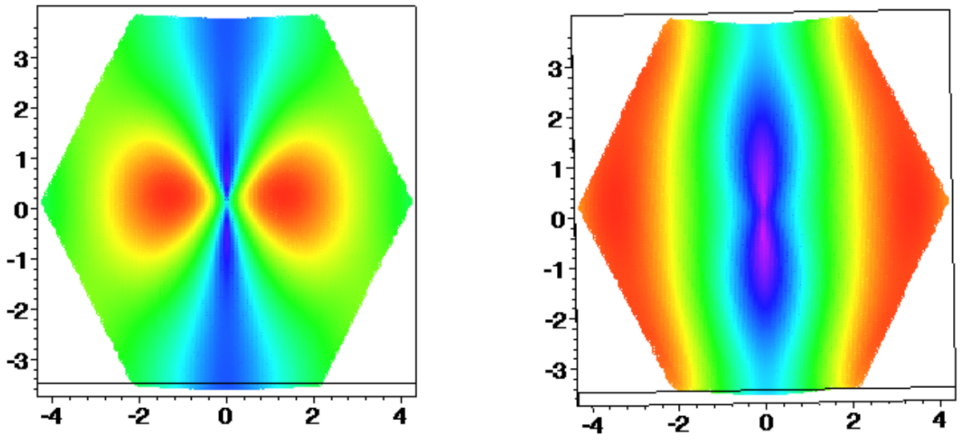

Figure B.3: Omega and out of plane amplitude divided by in plane amplitude in first Brillouin zone at $\tau = .0064$ ($T = 1K$).